CHALMERS
UNIVERSITY OF TECHNOLOGY

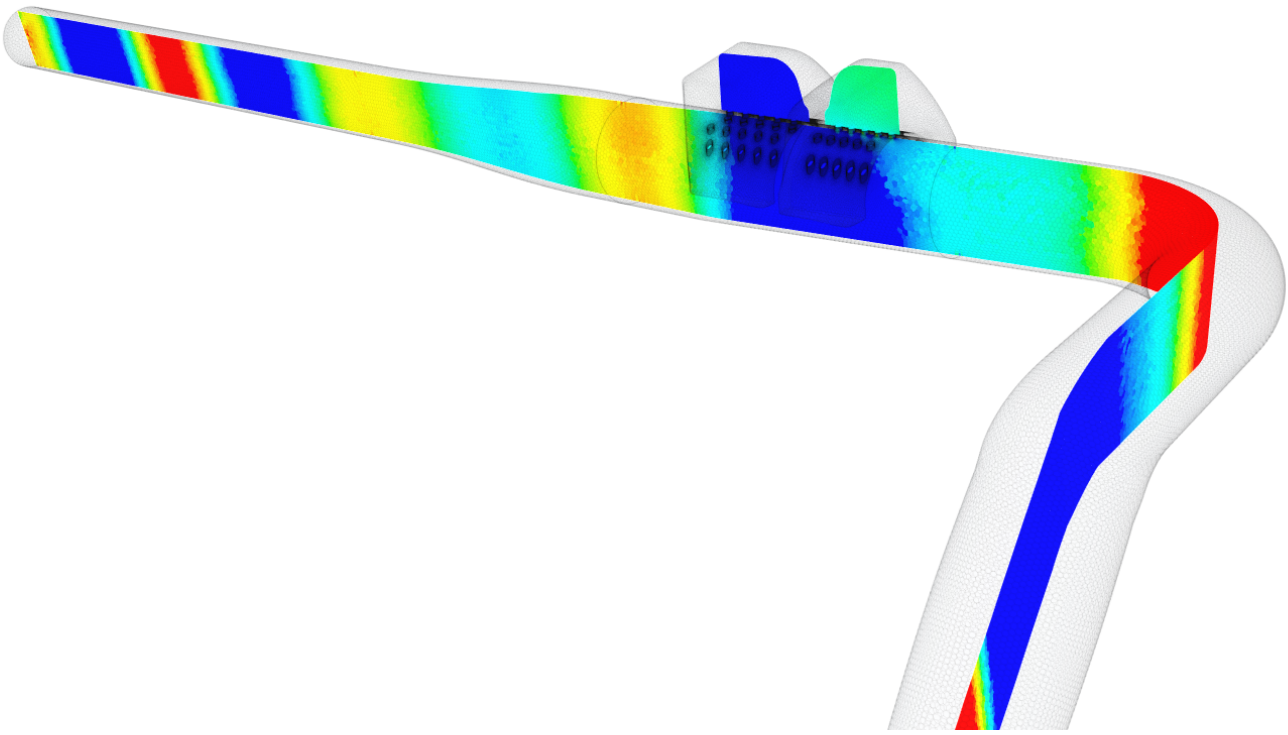

Flow Acoustic Effects on a Commercial Automotive Air Intake Silencer

A Numerical Study using Computational Fluid Dynamics

Master's Thesis in Applied Mechanics

LINUS ZACKRISSON

Department of Applied Mechanics
CHALMERS UNIVERSITY OF TECHNOLOGY
Gothenburg, Sweden 2017

Master's thesis 2017:76

Flow Acoustic Effects on a Commercial Automotive Air Intake Silencer

A Numerical Study using Computational Fluid Dynamics

LINUS ZACKRISSON

CHALMERS
UNIVERSITY OF TECHNOLOGY

Department of Applied Mechanics
Division of Fluid Dynamics
Chalmers University of Technology
Gothenburg, Sweden 2017

Flow Acoustic Effects on a Commercial Automotive Air Intake Silencer
A Numerical Study using Computational Fluid Dynamics
LINUS ZACKRISSON

Supervisor: Magnus Knutsson, Volvo Car Group
Lars Davidsson, Department of Applied Mechanics

Examiner: Lars Davidsson, Department of Applied Mechanics

Master's Thesis 2017:76
Department of Applied Mechanics
Division of Fluid Dynamics

Chalmers University of Technology
SE-412 96 Gothenburg
Telephone +46 31 772 1000

Cover: Plane acoustic waves seen as difference in acoustic pressure fluctuations propagating in the air intake duct system.

Typeset in LaTeX
Printed by Reproservice/Department of Applied Mechanics
Gothenburg, Sweden 2017

Flow Acoustic Effects on a Commercial Automotive Air Intake Silencer
A Numerical Study using Computational Fluid Dynamics
LINUS ZACKRISSON
Department of Applied Mechanics
Chalmers University of Technology

Abstract

Noise generated by turbo-compressors in combustion engine air intake systems is often mitigated by broad-band high-frequency duct silencers. The acoustic performance of a developed silencer design is generally obtained numerically without influence of duct mean flow, using acoustic computer aided engineering (CAE) tools. Discrepancies are however created between the acoustics of the real air intake system and numerical model of the system since mean duct flow is always present in the real system, due to the aspiration of the engine. This Master's thesis project aims to capture flow effect on silencer acoustic performance numerically using computational fluid dynamics (CFD). In cooperation with Volvo Car Group, a commercially existing part of an air intake system, including a silencer composed of two Helmholtz resonators, is studied. An already established academic CFD methodology is explored, used, expanded and streamlined to investigate flow effects on acoustic properties of the complex silencer-duct system. The acoustic properties from the CFD simulation are then compared to experimental data and acoustic CAE.

The established CFD methodology is integrated and applied using the commercial CFD software Star-CCM+, studying the silencer acoustic behaviour with several mean inlet flow speeds. Using Star-CCM+, mean flow and acoustic wave propagation is simulated simultaneously in the defined computational domain of the given silencer-duct system. Acoustic waves in a frequency band of interest related to the eigenfrequency of the silencer, are inserted through a time-varying inlet boundary condition. The numerical setup mimics an acoustic experimental measurement setup where the propagating acoustic waves are captured as pressure signals in virtual microphones, to calculate the acoustic silencing property of transmission loss (TL). Turbulence is modelled using the unsteady Reynolds-averaged Navier-Stokes equations (URANS). Numerical parameters in the CFD setup are studied in regards to numerical accuracy and computational efficiency, to find the most optimal model in describing the flow effect on silencer acoustic performance. The most optimal resulting CFD methodology was able to capture transmission loss characteristics with reasonable accuracy, under predicting the resulting eigenfrequency shift with roughly 8.5 % difference for all flow speeds; as well as a 11.4 % transmission loss peak difference, both in comparison to experimental data.

Different duct geometrical changes were then studied using the optimally developed CFD setup, in order to improve silencer acoustic performance under flow condition. Through a numerical process, six different geometrical changes were developed with varying strategies. The best design resulted in a 15 % increase in first order resonance

peak transmission loss and removal of eigenfrequency shift as well as only increasing pressure drop by 1.1 %, in comparison to a reference simulation.

Keywords: Computational fluid dynamics (CFD), Aeroacoustics, Air intake silencer, Helmholtz resonator, Flow effect, Transmission loss, Noise reduction, Star-CCM+, Unsteady Reynolds averaged Navier-Stokes equations (URANS), geometrical change.

Acknowledgements

The presented Master's thesis project has been conducted in cooperation with the NVH & Driving Dynamics Centre at Volvo Car Group, spring 2017. I would like to express my deepest gratitude towards my supervisor Magnus Knutsson as well as co-worker Simone Vizzini for their continuous encouragement, excellent support and feedback throughout the project. Further, I give thanks to Axel Kierkegaard at Siemens PLM for showing great interest in my project, providing me with valuable information and support regarding Star-CCM+ and CFD. I also want to thank my professor, supervisor and examiner Lars Davidsson at Chalmers University of Technology's Division of Fluid Dynamics for the interesting discussions regarding the project and valuable feedback.

Finally, I want to show my appreciation by thanking all co-workers at the NVH & Driving Dynamics Centre as well as surrounding project groups of interest at Volvo Car Group, it has been a pleasure to work at the office everyday beside all wonderful and friendly people.

Linus Zackrisson, Gothenburg, June 2017

Contents

List of Figures

List of Tables

Nomenclature

Abbreviations

Acronym	Expansion
1D	One-Dimensional
2D	Two-Dimensional
3D	Three-Dimensional
AML	Acoustic Mach number Level
CAD	Computer-Aided Design
CAE	Computer-Aided Engineering
CFD	Computational Fluid Dynamics
CFL	Courant-Friedrischs-Lewy
DES	Detached Eddy Simulation
DNS	Direct Numerical Simulation
DTFT	Discrete-Time Fourier Transform
FEM	Finite Element Method
FFT	Fast Fourier Transform
FVM	Finite Volume Method
HVAC	Heating, Ventilation and Air Conditioning
IL	Insertion Loss
LBM	Lattice Boltzmann Method
LES	Large Eddy Simulation
LNSE	Linearized Navier-Stokes Equations
NR	Noise Reduction
RANS	Reynolds-Averaged Navier–Stokes
RMS	Root Mean Square
PDE	Partial Differential Equation
PISO	Pressure Implicit Splitting of Operators
SIMPLE	Semi-Implicit Method for Pressure Linked Equations
SPL	Sound Pressure Level
SST	Shear Stress Transport
TL	Transmission Loss
BD	Bent duct
SD	Straight duct
BM	Basic mesh

IM	Intermediate mesh
AM	Advanced mesh
DM	Distant microphones
CM	Close microphones

Greek symbols

Variable	Description	Unit
β^*	Constant for k-ω turbulence model	1
γ	Turbulence intermittency	1
Γ	Arbitrary diffusion coefficient	-
δ_{ij}	Kronecker delta	1
δ_n	Neck end correction	m
δ_{vol}	Two-source spatial definition function	m
Δ	Discrete differentiating	-
ε	Turbulent dissipation rate	m^2/s^3
κ	Thermal conductivity	W/(m·K)
κ_t	Turbulent thermal conductivity	W/(m·K)
λ	Wavelength	m
Λ_ϕ	Arbitrary steady transport variable	-
μ	Dynamic viscosity	kg/(m·s)
μ_t	Turbulent dynamic viscosity	kg/(m·s)
ν	Kinematic viscosity	m^2/s
ρ	Density	kg/m^3
ρ_0	Density in undisturbed medium	kg/m^3
ρ_{ac}	Acoustic density disturbance	kg/m^3
σ_ε	Turbulent Prandtl number for ε equation	1
σ_k	Turbulent Prandtl number for k equation in $k-\varepsilon$ turbulence model	1
σ_k^ω	Turbulent Prandtl number for k equation in $k-\omega$ turbulence model	1
σ_θ	Turbulent Prandtl number	1
σ_ω	Turbulent Prandtl number for ω equation	1
τ_{ij}	Viscous stress tensor	$kg/(s \cdot m^3)$
τ_w	Wall stress tensor	$kg/(s \cdot m^2)$
ϕ	Arbitrary tensor variable	-
ψ	Arbitrary tensor variable	-
ω	Specific dissipation rate	1/s
ω_f	Angular frequency ($2\pi f$)	rad/s

Roman symbols

Variable	Description	Unit
$a_{P,nb}$	Discretization coefficients	-
a_{emp}	Empirical inlet boundary condition constant	m/s

a_{in}	Amplitude of acoustic velocity at inlet	m/s
A	Area	m^2
c	Speed of sound	m/s
C_p	Specific heat at constant pressure	J/(kg·K)
C_v	Specific heat at constant volume	J/(kg·K)
C_μ, $C_{\varepsilon 1}$, $C_{\varepsilon 2}$,	Constants for k-ε turbulence model	1
$C_{\omega 1}$, $C_{\omega 2}$,	Constants for k-ω turbulence model	1
d	discrete FFT bucket number	1
D	Diameter	m
e	Internal energy	J
f	Frequency	1/s
f_c	"Cut-on" frequency	1/s
f_d	Discrete FFT frequency	1/s
f_r	Resonance frequency	1/s
f_s	Sample-rate	1/s
$\mathcal{F}$	Fourier transform operator	-
g	Arbitrary signal	-
h	Specific enthalpy	J/kg
H	Acoustic transfer function	
k	Turbulent kinetic energy	$\mathrm{m}^2/\mathrm{s}^2$
k_w	Wavenumber	1/m
k_{wr}	Wavenumber for reflected wave component	1/m
L	Characteristic length	m
L_{in}, L_{out}	Inlet/Outlet duct length	m
L_S	Spatial limit of mass source	m
M	Mach number	1
M_{in}	Mach number profile at inlet boundary	1
M_m	Mass of a mole of gas	kg
N	Number quantity	1
N_s	Sample space	1
i	Imaginary unit	-
p	Static pressure	Pa
p_0	Pressure in undisturbed medium	Pa
p_{ac}	Acoustic pressure	Pa
r	Specific acoustic resistance	Pa· $\mathrm{s/m}^3$
R	Ideal gas constant ($R = 8.315$)	J/(mol·K)
R	Reflection coefficient (acoustics)	1
R_s	Specific Gas constant ($R_s = 287$, dry air)	J/(kg·K)
s	Microphone spacing	m
$S_{"11"}$	Auto-spectral density of signal 1	-
$S_{"12"}$	Cross-spectral density of signal 1 and 2	-
S_C	Continuity source term	$\mathrm{kg/(s{\cdot}m^3)}$
S_M	Momentum source term	$\mathrm{kg/(m^2{\cdot}s^2)}$
S_E	Energy source term	$\mathrm{kg{\cdot}J/(s{\cdot}m^3)}$
t	Time	s
T	Temperature	K

T_s	Sampling time interval	s
$\mathcal{U}$	Continuous uniform distribution	1
v	Velocity, characteristic velocity	m/s
v_0	Initial velocity	m/s
v^*	Friction velocity	m/s
v_f	Fluctuating acoustic velocity at inlet	m/s
v_p	Particle velocity (acoustics)	m/s
v_u	Uniform constant velocity	m/s
V	Volume	m^3
V_c	Resonator house volume	m^3
w	Vorticity	1/s
W	Sound power	W
x	Specific acoustic reactance	Pa$\cdot s/m^3$
x'	Local normal coordinate from flow boundaries	m
$x_{i,j,k}$	Spatial coordinate representation of x,y,z	m
y^+	Non-dimensional wall distance	m
z	Specific acoustic impedance	Pa$\cdot s/m^3$

Dimensionless numbers

Variable	**Description**	**Definition**
Re	Reynolds number	$Re = \frac{\rho L v}{\mu}$
St	Strouhal number	$St = \frac{f_r L}{v}$

Accents

Accent	**Description**
$\bar{\cdot}$	Time average
$\tilde{\cdot}$	Cell average
$\hat{\cdot}$	Fourier transform

Subscripts

$+$	Incident sound wave
$-$	Reflected sound wave
n	Neck
u	Upstream
d	Downstream
i, j, k	Einstein summation convention index for spatial coordinate dimensions
ref	Reference value
eff	Effective value
m	Mean
max	Maximum

min	Minimum

Superscripts

$'$	Turbulent fluctuating value

Software

Star-CCM+	Commercial CAE CFD software
ANSA	Commercial CAE pre-processing software
MATLAB	Multi-functional numerical computing software including its own programming language
Actran	Commercial FEM-based acoustic CAE software

1 Introduction

Noise pollution is a common problem and source of discomfort for both humanity and nature in today's society and generally caused by unwanted sounds from transportation, industry or recreational activities. [1, 2, 3] The problem will possibly further aggravate in the future due to an increasing density of the aforementioned noise generating sectors with a larger world population and increase in demand for related services. Noise is therefore studied, regulated and monitored by many countries, authorities and establishments due to the negative effects.

Noise from the transportation sector, and more specifically road vehicles with internal combustion engines, is something people interact with in a day-to-day basis making it an important area for noise control. Manufacturers of all kinds of road vehicles strive to mitigate as much noise as possible to produce silent vehicles both due to legislation and competition. The topic of noise reduction in passenger cars is related to efficient mitigation of harmful noise as well as reducing unwanted sounds for improved comfort and sound quality experience. Road vehicles can be characterized by many different noise sources and some typical noise generation areas are; powertrain, engine-breathing system, exterior flow noise, road tire noise and HVAC-systems. This study will focus on the engine breathing system which can be separated in three parts; intake, exhaust and gas-exchange in the engine. All three parts have their respective noise characteristics, where the common noise generator is the engine (low frequency) but could also include flow induced noise (high frequency) in valves, ducts and turbo-compressors in the intake system. The use of turbo-compressors in air intake systems as part of the powertrain, is common practice in automotive industry due to several beneficial factors. Special attention is therefore needed to mitigate the increased generation of flow noise from the turbo-compressor.

Turbo-compressors in internal combustion engines are a major source of noise depending on engine operating condition, causing undesirable sounds in current passenger cars. The noise can further be amplified by the acoustic resonances of the air intake duct system. The turbo-compressor generates a broad frequency spectrum of noise while operating, for example the characteristic blow off/bypass valve noise and whoosh noise (close to surge operating condition). To mitigate noise in the air intake system, two approaches exist; a proactive approach by studying and reducing aeroacoustic noise generation in the turbo compressor itself or dampening the propagating sound in the duct system. Mitigation of noise generated by/in the turbo compressor is hard to achieve due to the complex aeroacoustic physics and behaviours. Hence, main focus is often put on dissipative or reactive noise cancellation in the duct system. Dissipative noise dampening is achieved by lining the inside of ducts with acoustically dissipative materials such as porous foam. Adding dissipative materials in the intake ducts is however normally unwanted as the foam might degrade with time, reducing efficiency or breaking and possibly harming the engine. Reactive noise cancellation is therefore preferred and achieved by implementing acoustic broad band side-branch silencers in close proximity to the turbocharger in the duct system. One type of side-branch silencer that could achieve broad-band noise reduction is a silencer that includes several narrow band Helmholtz-like resonators coupled in series to cover the broad frequency band of noise generated by the turbocharger. If intake noise is not mitigated by silencers in the duct system, the noise will either propagate to the duct orifice, cause structural vibrations and radiate noise through the duct walls, affecting either vehicle passengers or external environment. Generally, the Helmholtz resonator has been studied thoroughly due to its effective narrow band acoustic dampening abilities at low to medium frequencies. By studying different design options and geometry it is possible to affect the acoustic performance of the Helmholtz resonator. Developing and designing effective resonators to reduce noise in the problematic frequency bands requires accurate and robust methods for performance prediction.

A Helmholtz resonator is a type of side-branch silencer where a closed volume of air is attached to the duct with one or several smaller ducts, called necks. Interesting geometrical parameters to change when designing the acoustic properties of a Helmholtz resonator are size and shape of neck and volume, number of necks as well as location of the resonator in relation to the duct system. The interesting acoustic properties when studying design options are; resonance frequency, frequency band and amplitude of noise reduction, also called resonator attenuation. [4] Further, experimental studies have shown differences in resonator attenuation when the resonator is working under different air flow conditions (air flow present in the duct, grazing the neck openings). [5, 6, 7, 8] The flow effect is important to have in mind when designing engine air intake silencers as flow is always present and varying due to the constant forced aspiration of the engine. McAuliffe [5] experimentally studied Helmholtz resonators under flow effect. Meyer *et al.* [6], Phillips [7] and Anderson [8] further investigated the effects of flow on resonator attenuation for different Helmholtz resonators. Meyer *et al.* [6], Phillips [7] and Anderson [8] observed that the resonance frequency of the Helmholtz resonator increased with increasing mean duct flow velocity as well as noting a velocity range where no flow effects could be observed. It was also concluded that the acoustic resistance of the neck increases linearly with increasing flow speed which explained the linear increase in resonance frequency. Hersh and Walker [9] showed through experiments and semi-empirical models the flow effects on the impedance of a Helmholtz resonator, thus being able to show a linear increase of acoustic resistance and diminishing reactance with increasing mean flow speed. Thus, grazing duct mean flow causes an acoustic degradation of the Helmholtz resonator acoustic performance, increasing resonance frequency and diminishing efficiency with increasing duct mean flow.

To effectively assess different resonator designs (Helmholtz resonator and duct system) during product development, acoustic computer aided engineering (CAE) can be used. Acoustic CAE is based on the governing acoustic wave equation and can numerically describe the acoustic properties of the resonator previously defined with good accuracy in the frequency domain. The current practise in industry is to simulate the acoustic properties of the resonator without considering the influence of air flow through the resonator. Simulation is performed where standing sound wave formation in the frequency domain is calculated in space without hydrodynamic movements. This methodology creates discrepancies between the results of CAE and reality due to the interaction between sound waves and air flow driven by the aspiration of the engine. Hence, the acoustic wave equation-based CAE is not able to capture effects from duct mean flow and flow excited acoustic resonances without further modelling. Semi-empirical models describing mean flow effect on impedance was implemented in acoustic CAE by Allam *et al* [10] to describe flow effect on Helmholtz resonators with reasonable accuracy. The discrepancies are often caused by non-linear effects in the interface between the Helmholtz resonator and the duct.

The early experimental investigations are useful to asses the effects of mean flow on the acoustic properties of Helmholtz resonators and frequency-domain based CAE can describe the acoustic properties without mean flow. But to be able to design effective resonators with consideration for flow effects, a computational technique able to capture the fluid physics and acoustic behaviour in the time-domain accurately is necessary. A simplified way of describing the interaction between fluid flow and acoustic wave propagation is applying the linearized Navier-Stokes equations (LNSE). The LNSE methodology is based both on computational fluid dynamics (CFD) and acoustic CAE governed by the acoustic wave equation. Du *et al.* [11] employed the LNSE methodology for a three-dimensional (3D) geometry of a silencer composed of two multi-neck Helmholtz-like resonators. Du *et al.* studied and captured flow effects on the acoustic property transmission loss (TL) for Mach numbers between 0-0.2 and acoustic frequency range of 500-2500 Hz. Transmission loss characteristics are often used to determine the acoustic performance of noise reducing devices such as silencers and resonators. In duct acoustics, TL is generally defined as the difference in sound power between incident and transmitted sound wave of a noise suppressing device. [12] Transmission loss is directly depending on resonance frequencies and acoustic resistance of studied acoustic devices. Thus, TL of acoustic devices is affected both in amplitude reduction and frequency shift previously mentioned in [6, 7, 8], with increasing duct mean flow. Transmission loss calculations also require that no acoustic wave reflections occur from inlet and outlet boundaries. The way of capturing flow effects with LNSE is limited to one-way coupling between fluid flow and acoustic wave propagation, where only sources from the flow influence the acoustic wave equation but not the vice-versa. Another way of fully capturing the two-way coupling between flow and sound waves is using computational fluid dynamics to capture 3D, unsteady, non-linear, viscous and compressible turbulent flow, including acoustic wave propagation and flow-acoustic coupling behaviours in the CFD solver. One of the earliest time-domain based numerical models to capture grazing mean flow effects on acoustic properties of a Helmholtz resonator was presented by Cummings [13]. Through a quasi one-dimensional (1D) approach with consideration of flow effect on acoustic resistance, Cummings was able to calculate resonator cavity pressure. With CFD and the Lattice Boltzmann method (LBM) Ricot *et al.* [14] numerically studied "sunroof buffeting", closely resembling unsteady flow past a Helmholtz-like cavity, to investigate resonance velocity range and the maximum sound pressure level (SPL) in the cavity. The dissipation mechanism of acoustic liners (small and high density packed Helmholtz resonators) was studied by Tam and Kurbatskii [15] and Tam *et al.* [16], employing direct numerical simulation (DNS) for the CFD simulation.

More recently, Iqbal and Selamet [17] simulated the flow effects on a Helmholtz resonator with a non-commercial two-dimensional (2D) unsteady Reynolds-averaged Navier-Stokes (URANS) solver. The study by Iqbal and Selamet captured trends in their simulations that has previously been observed experimentally [5, 6, 7, 8, 9] but was limited to studying a 2D computational domain and the study was absent of experimental data for comparison. The main purpose of the study was to investigate the flow effects on transmission loss with a duct flow Mach number range of 0-0.3 and frequency range of 70-210 Hz. Selamet *et al.* [18, 19] expanded and continued on the studies by Iqbal and Selamet [17] with a 3D URANS CFD simulation of two simple Helmholtz resonators (one for each study). The study focused on flow effects on transmission loss for the simple geometries as well as looking in to the effect of numerical discretization of the governing flow equations. Selamet *et al.* successfully showed good resemblance between numerical and experimental data obtained in a flow-impedance tube for the studied frequency and Mach number range of 50-200 Hz and 0-0.1. The numerical technique established by Iqbal and Selamet [17] and Selamet *et al.* [18, 19] acts as a strong foundation for further investigations, where this Master's Thesis project will continue on.

1.1 Aim

The present Master's Thesis study is performed in cooperation with Volvo Car Group, a passenger car manufacturer in Sweden. Using Volvo Car Group's computational resources, an already commercially existing intake duct system including an adjunct broad band silencer composed of two complex multi-neck Helmholtz resonators is studied. The commercially existing air intake system with studied part of the system highlighted in dark gray can be seen in Figure 1.1. Starting from the studies by Iqbal and Selamet [17] and Selamet *et al.* [18, 19], their initial numerical CFD model will be explored, used, expanded and streamlined to investigate flow effects on acoustic properties of the complex silencer. A numerical CFD investigation in meshing methodology, turbulence modelling and technique to measure transmission loss is performed. Here the CFD simulation will describe both the turbulent flow field and acoustic wave propagation within the flow field. The CFD simulations are performed using the commercial CAE software Star-CCM+ version 11.06.010. To obtain a reference case for the silencer with no flow effects, the acoustic acoustic wave equation based CAE software Actran version 16.0 is used to obtain silencer acoustic properties in the frequency domain. The 3D mesh of the computational domain for CFD will be created in the volume mesh generator of Star-CCM+. To create the volume mesh in Star-CCM+, a surface mesh is imported from the CAE pre-processing software ANSA version 16.2.0 where an association with a computer aided design (CAD) model is made. The 3D computational mesh used in Actran for the acoustic acoustic simulations is created directly in ANSA. Post-processing will mainly be done using MATLAB.

The resulting data is validated using experimental data of the given silencer obtained at the Marcurs Wallenberg Laboratory for Sound and Vibration Research at the Royal Institute of Technology (KTH) in Stockholm. Here, the main acoustic property studied is transmission loss. The studied frequency and Mach number range is set to 500-1750 Hz and 0-0.2 respectively, chosen based on the ability to capture resonance frequencies and relevant duct air flow velocities for a vehicle engine air intake system. For further investigation of the acoustic degradation of the Helmholtz resonators with increasing air flow, geometrical duct changes will be studied to alter flow conditions to suppress the diminishing acoustic flow effect. The aim with this is to understand and mitigate transmission loss reduction and frequency shift that occurs with increasing duct mean air flow.

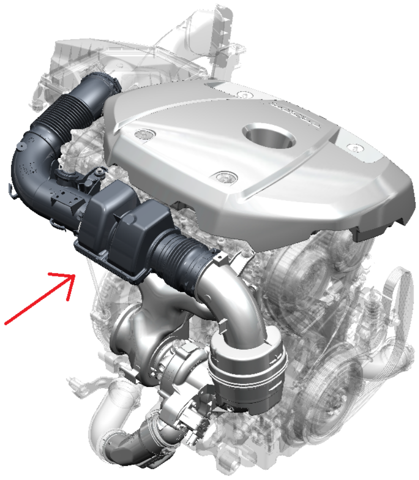

Figure 1.1: Highlighted studied part of the air intake duct system with silencer (red arrow) of a 4-cyl. turbo Volvo engine, upper connection (part flow inlet) to air filter box and lower connection (part flow outlet) to continuing pipe system with another silencer and turbo-compressor.

1.2 Purpose

The purpose of this Master's Thesis project is to be able to predict the resonator acoustic behaviour under air flow condition using a commercial CFD software for a complex commercial air intake duct system and Helmholtz resonator silencer; to understand what causes the coupling behaviour between flow and acoustics. Using this model it is planned to study different design options in regards to physics and geometry, and how they affect the flow and acoustic properties of the resonator. Together, it is interesting to understand how to mitigate the acoustic degradation with increasing duct mean flow. This in turn might lead to a new understanding of effective design options for air intake silencers, in the form of improved transmission loss characteristics when air flow is present in the duct, for automotive industry and other potential applications.

1.3 Limitations

The main focus of this Master's Thesis study is to investigate one designated air intake system with three discretely chosen constant air flow velocities. Frequencies outside of the chosen frequency range are also out of interest. Potential acoustic noise generation in the form of whistling or turbulent shearing will not be investigated and physically described with the simulations, but will be discussed. Possibility to manufacture the different design options through mass production is not of interest to this study.

1.4 Methodology

A flow scheme is presented in Figure 1.2, depicting the work flow of a CFD simulation setup. Initially a CAD model is created or in this case imported to the CAE software ANSA to create the computational domain. The computational domain in the form of a pre-processed surface mesh is imported into Star-CCM+ where a volume mesh is generated. When the mesh is generated all the models for physics is defined including material properties, flow and energy coupling, turbulence and numerical schemes. Here, the fluid physics are defined and the acoustic physics are embedded into the fluid physics directly. Further, the boundary conditions are defined in Star-CCM+ with input data from MATLAB, where the acoustic waves will be introduced into the simulation. In preparation for post-processing, certain points of interest must be defined where solution data will be saved specifically. When all model parameters and boundary conditions are set the solution can be initialized and the calculation can be started. After the simulation has finished, data can be extracted in the computational domain for post-processing in either Star-CCM+ or MATLAB. The last step is made iteratively depending on the quality of the evaluated results or if further simulations with different setups are needed.

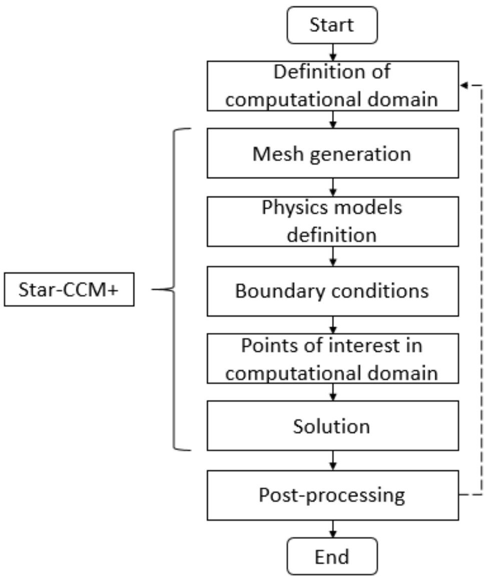

Figure 1.2: Flow scheme of CFD methodology.

1.5 Report Structure

In this short chapter the structure of the report is presented. The next-coming Chapter 2 will describe the theories of interest regarding mathematical descriptions of acoustics and the dynamic behaviour of a turbulent fluid including acoustic waves. The given part of the air intake system including the side-branch Helmholtz-like resonator silencer is further presented in Chapter 3. In Chapter 4, all methodologies used will be presented encapsulating both numerical methodology treating the governing equations in Chapter 2 and how the numerical methodologies are used in the simulation methodologies. The report will further continue with a presentation of results and discussed in Chapter 5. A small summary and full conclusion will be shown in Chapter 6 and finally the report ends with some remarks about future work in Chapter 7.

2

Theory

This chapter aims to provide a theoretical background in all areas of interest in fluid dynamics and acoustics related to the study. Initially the governing equations of viscous, turbulent fluid flow as well as describing the turbulence models used in the simulation setup and boundary layer flow theory is presented. The chapter will further continue to present the acoustical theories behind Helmholtz resonators and acoustic waves followed by measuring techniques for acoustical devices regarding transmission loss. The chapter will end with a small description of the flow effects on a Helmholtz resonator.

2.1 Fluid Dynamics

Fluid dynamics is the scientific description of fluid flow (liquid or gas) in mathematics and physics. To describe a fluid motion and propagating acoustic waves in a pipe with time, fluid dynamic theory is needed. This theoretical chapter aims to describe the governing equations for both general and turbulent flow, the coupling between physical phenomena in the fluid and turbulence modelling.

2.1.1 Governing equations of conservation

The fundamental principles of a fluid in motion is mathematically described with the **equations of conservation**. More specifically they originate from the fundamental laws of mass conservation, momentum conservation (Newton's second law of motion) and energy conservation (second law of thermodynamics). To be able to write the equations of conservation, the fluid must obey the continuum assumption. The assumption states that

- the fluid is seen as a continuous media rather than seeing what the fluid is chemically composed of, a discrete number of molecules
- fluid properties like velocity, density, temperature and pressure are continuously defined in the fluid media over infinitesimally small spacial grid points instead of defining fluid properties for each molecule

The continuum assumption is fulfilled if the fluid is dense enough, which is applicable for air at atmospheric condition. A fluid and its motion can hence be mathematically described with the three continuum equations of conservation.

Conservation equation of continuity:

$$\frac{\partial \rho}{\partial t} + \frac{\partial \rho v_i}{\partial x_i} = S_C \tag{2.1}$$

Conservation equations of momentum (Navier-Stokes equations):

$$\frac{\partial \rho v_i}{\partial t} + \frac{\partial \rho v_j v_i}{\partial x_j} = -\frac{\partial p}{\partial x_i} + \frac{\partial \tau_{ij}}{\partial x_j} + S_{M,i} \tag{2.2}$$

Conservation equation of energy:

$$\frac{\partial \rho e}{\partial t} + \frac{\partial \rho v_i e}{\partial x_i} = -p\frac{\partial v_i}{\partial x_i} + \tau_{ij}\frac{\partial v_i}{\partial x_j} + \frac{\partial}{\partial x_j}\Big(\kappa\frac{\partial T}{\partial x_j}\Big) + S_E \tag{2.3}$$

Here the viscous stress tensor τ_{ij} is defined with Equation (2.4), originating from the definition of an **isotropic Newtonian viscous** fluid, where viscous stresses are linearly proportional to the strain rate. The local fluid strain rate is related to the viscous stress through the dynamic viscosity μ.

Isotropic Newtonian viscous relation:

$$\tau_{ij} = \mu\Big(\frac{\partial v_i}{\partial x_j} + \frac{\partial v_j}{\partial x_i}\Big) - \frac{2}{3}\mu\frac{\partial v_k}{\partial x_k}\delta_{ij} \tag{2.4}$$

Equations (2.1-2.4) governs the physical behaviour of a transient, compressible, viscous, Newtonian fluid with arbitrary source terms in three dimensions, written in Einstein tensor notation. The indices i, j and k are written as subscripts on variables to define the spatial coordinate x, y and z of the variable. This is done by letting the indices i, j and k range independently over the set of $\{1, 2, 3\}$ where the numbers represent the three spatial dimensions. If an index notation appears twice in a term, the variables with the same indices are summed. An example of this can be seen in Equation (2.5).

$$\frac{\partial \rho v_i}{\partial x_i} = \frac{\partial \rho v_1}{\partial x_1} + \frac{\partial \rho v_2}{\partial x_2} + \frac{\partial \rho v_3}{\partial x_3} = \frac{\partial \rho v_x}{\partial x} + \frac{\partial \rho v_y}{\partial y} + \frac{\partial \rho v_z}{\partial z} \tag{2.5}$$

In Equations (2.1)-(2.4), v_i is the velocity in dimension i, x_i is the spatial coordinate in dimension i, t is the time, ρ is density, p is the static pressure, e is the internal energy, T is the temperature of the fluid, κ is the thermal conductivity and $S_{\{C,(M,i),E\}}$ are source terms for each equation of conservation. In Equation (2.4) the variable δ_{ij} represents the Kronecker delta function taking on a value of 1 if $i = j$, otherwise

0 if $i \neq j$. Most often the source terms can be neglected but the source term of continuity will play a role in further methodology. It is also utmost important to keep the first term describing transient behaviour in Equation (2.1), (2.2) and (2.3). This keeps the temporal dependency of the flow which is necessary when involving propagating acoustic waves in the fluid. Further, the density $\rho = \rho(t, x, y, z)$ is varying in space and time, also known as allowing the fluid to compress. This makes it possible for acoustic waves to exist in the fluid as acoustic waves are adiabatic compressions and decompressions of the fluid. The energy equation is present in the formulation to calculate a varying temperature field in space and time through the relation between internal energy and temperature, $e = C_v T$, for a compressible fluid. Here C_v is the specific heat at constant volume which can either be set as constant or varying with other variables. [20]

If one assumes that the source terms are negligible or known and inserting Equation (2.4) in Equation (2.2) and (2.3), the conservation equations ends up containing five equations (one continuity, three momentum and one energy) to solve for six unknown variables (density ρ, velocity in three dimensions v_i, pressure p and temperature T). The fluid properties specific heat C_v and thermal conductivity κ is already known through being constant material property and the dynamic viscosity μ can be related to temperature through Sutherland's law in Equation (2.6).

Sutherland's law:

$$\mu(T) = \mu_{ref}\Big(\frac{T}{T_{ref}}\Big)^{\frac{3}{2}}\Big(\frac{T_{ref} + T_{eff}}{T + T_{eff}}\Big) \tag{2.6}$$

where T_{ref} and μ_{ref} are referential values for temperature and dynamics viscosity and T_{eff} is the effective temperature or also known as the Sutherland's constant. [21]

Hence, the equation system is unsolvable if not another equation can be expressed for the material. In this case, the material fluid is air at atmospheric condition and thus the ideal gas law can be utilized as an **equation of state** for the material.

Equation of state:

$$p = \rho R_s T \tag{2.7}$$

Here R_s represents the specific gas constant for dry air at atmospheric condition. The equation of state relates gas properties thermodynamically, describing the gaseous state under a given physical conditions. Now, the equation system of conservation are closed and solvable. Analytically they are only applicable on simple flow problems as laminar flow over a flat plate. The partial differential equation (PDE) system needs to be solved numerically for more complex flows including turbulence.

Numerically the equation system can be solved without modelling either assuming laminar flow or through direct numerical simulation (DNS), where turbulent flow is numerically resolved at the smallest flow scales. However, turbulent velocity, time and length scales vary widely in space and time leading to the method of DNS requiring very high temporal and spatial resolution to capture all turbulent flow phenomenons. Applying DNS correctly will also make it possible to capture full turbulent noise generation and wave propagation, called direct noise simulation. The high temporal and spatial resolution results in a very computationally expensive and time consuming simulation method only applicable in academia or simple flows. In the case described in this thesis, the intake air flow is turbulent and the scope of the project as well as limited computational resources hinders the use of DNS, deeming it is unnecessary and too expensive. [20]

2.1.2 Turbulent flow

Turbulence is present in the most common fluid flows including air pipe flow at relatively high mean flow speed. Turbulence is also physically undefined but can be characterized. Turbulent flow is irregular and chaotic but follows the Navier-Stokes equations, fundamentally increases diffusivity of the flow and always unsteady three-dimensional. Turbulence is also dissipative, meaning that turbulent kinetic energy in the turbulent flow structures (eddies) are dissipated from the largest scales down to the smallest turbulent scales called the Kolmogorov scales through the cascade process. Turbulent kinetic energy present at the Kolmogorov scales follows the second law of thermodynamics by dissipating to heat through viscous forces. For turbulence to continuously exist spatially and temporally, a steady supply of energy is needed from the mean flow. Turbulence also generally fulfills the continuum assumptions as the characteristic Kolmogorov scales in turbulent flow are considerably larger than molecular scales. [20]

To describe turbulence mathematically and implement turbulence in the previously documented equations of conservation through modelling, the most general approach is to look at an arbitrary turbulent instantaneous variable $\phi(t, x, y, z)$. The arbitrary variable ϕ can be separated in two parts; a time-averaged part $\bar{\phi}(x, y, z)$ representing mean flow and one instantaneous turbulent fluctuating part $\phi'(t, x, y, z)$ leading to Equation (2.8).

$$\phi = \bar{\phi} + \phi' \tag{2.8}$$

Where the accent $\bar{\cdot}$ represents a discrete temporal average as expressed in Equation (2.9).

$$\bar{\phi}(x, y, z) = \frac{1}{(t_1 - t_0)} \int_{t_0}^{t_1} \phi(t, x, y, z) dt \tag{2.9}$$

Some general mathematical definitions and formulas for arbitrary turbulent variable ϕ and ψ can be seen in Equation (2.10).

$$\begin{aligned} &\bar{\phi}' = \bar{\psi}' = 0, \quad \bar{\bar{\phi}} = \bar{\phi}, \quad \overline{\frac{\partial \phi}{\partial s}} = \frac{\partial \bar{\phi}}{\partial s}, \quad \overline{\phi + \psi} = \bar{\phi} + \bar{\psi}, \\ &\overline{\phi\psi} = \bar{\phi}\bar{\psi} + \overline{\phi'\psi'}, \quad \overline{\bar{\phi}\bar{\psi}} = \bar{\phi}\bar{\psi}, \quad \overline{\phi'\bar{\psi}} = 0 \end{aligned} \tag{2.10}$$

With the definitions of a decomposed turbulent variable in Equation (2.8),(2.9) and (2.10) it is possible to decompose the flow variables surrounding the governing equations of fluid flow described previously. Decomposing the temporally and spatially dependant variables in Equation (2.1), (2.2) and (2.3), time-averaging all equations in the equation system and using the mathematical formulas in Equation (2.10) leads to the **Reynolds-averaged Navier–Stokes** (RANS) equation system. By time-averaging the conservation equations over a discrete temporal step, the mean turbulent flow field is solved for. Keeping the transient term even though a time average is executed keeps a temporal dependency of turbulent variables, describing larger turbulent transients and acoustic wave propagation. By keeping the unsteady part in the RANS equations, one can call the equation system the **Unsteady Reynolds-averaged Navier-Stokes** (URANS) equations. The URANS equation system is a physical simplification compared to DNS as the URANS-method is incapable of resolving turbulence at the same refinement. However, solving the equation system requires substantially less computational effort in comparison to DNS as the temporal and spatial resolution required are coarser in relation to DNS. The URANS equations are presented in Equations (2.11)-(2.14).

Time-averaged equation of continuity:

$$\frac{\partial \bar{\rho}}{\partial t} + \frac{\partial \bar{\rho}\bar{v}_i}{\partial x_i} = S_C \tag{2.11}$$

Time-averaged equations of momentum:

$$\frac{\partial \bar{\rho}\bar{v}_i}{\partial t} + \frac{\partial \bar{\rho}\bar{v}_j\bar{v}_i}{\partial x_j} = -\frac{\partial \bar{p}}{\partial x_i} + \frac{\partial \bar{\tau}_{ij}}{\partial x_j} - \frac{\partial \bar{\rho}\overline{v_i' v_j'}}{\partial x_j} + S_{M,i} \tag{2.12}$$

Time-averaged equation of energy:

$$\frac{\partial \bar{\rho}\bar{e}}{\partial t} + \frac{\partial \bar{\rho}\bar{v}_i\bar{e}}{\partial x_i} = -\overline{\left(p\frac{\partial v_i}{\partial x_i}\right)} + \overline{\left(\tau_{ij}\frac{\partial v_i}{\partial x_j}\right)} + \frac{\partial}{\partial x_j}\left(\kappa\frac{\partial \bar{T}}{\partial x_j}\right) - \frac{\partial \bar{\rho}\overline{v_i' e'}}{\partial x_i} + S_E \tag{2.13}$$

$$\bar{\tau}_{ij} = \bar{\mu}\left(\frac{\partial \bar{v}_i}{\partial x_j} + \frac{\partial \bar{v}_j}{\partial x_i}\right) - \frac{2}{3}\bar{\mu}\frac{\partial \bar{v}_k}{\partial x_k}\delta_{ij} \tag{2.14}$$

Equations (2.11)-(2.14) now governs the physics of a time-averaged transient, compressible, viscous, Newtonian fluid with source terms in three dimensions including turbulence. When expanding multiplied decomposed variables, new terms appear related to turbulent fluctuations. First, all expanded terms including a time-average of fluctuating density ρ' or fluctuating dynamic viscosity μ' multiplied with arbitrary turbulent variable/s are approximated to be negligible, $\overline{\rho'\phi} \approx 0$ and $\overline{\mu'\phi} \approx 0$. An example of this would be a triple correlation $\overline{\rho' v_i' v_j'}$ expanded from the convection term in the momentum equation. This approximation is valid due to turbulent fluctuations in density nor dynamic viscosity being large enough to influence the turbulent flow phenomenons, Mach numbers above 2-3 are needed for such phenomena to be influential. Neither density differences of acoustic waves are strong enough to influence mean flow characteristics. Second, two important terms have appeared second to last in Equation (2.12) and (2.13), $\overline{\bar{\rho} v_i' v_j'}$ and $\overline{\bar{\rho} v_i' e'}$. The first term, $\overline{\bar{\rho} v_i' v_j'}$, is called the turbulent stress tensor (also called **Reynolds stress tensor**) and with it nine new unknown variables are introduced. The second term, $\overline{\bar{\rho} v_i' e'}$, is analogous to the Reynolds stress tensor but here describing the turbulent heat flux vector, also introducing three unknown variables. The RANS equation system is now open and unsolvable with six equations (including ideal gas law) and $6+9+3=18$ unknown quantities that needs to be solved for. More unknown variables could appear depending on how you expand and simplify the two first terms on the right-hand side in the time-averaged equation of energy (2.13). Two options now exist in how to solve the equation systems, either the computationally expensive method of DNS is used or the new turbulent terms need to be modelled through turbulence modelling theory, simplifying the problem. [20]

2.1.3 Turbulence modelling

One of the most common ways of closing the URANS equation system is to use the **Boussinesq assumption**. This way of closing the equation system is also generally called the eddy viscosity turbulence models. The unknown Reynolds stress tensor is analogously written as a turbulent diffusion term closely resembling the previously defined viscous stress tensor (See Equation (2.4)). Boussinesq assumption approximates a linear behaviour between Reynolds stress and strain rate through the turbulent dynamic viscosity μ_t. Additionally the trace of the left-hand side $\frac{1}{3}\overline{\bar{\rho} v_k' v_k'}\delta_{ij}$ must be added to the right-hand side to validate the assumption. The quantity turbulent kinetic energy $k = \frac{1}{2}\overline{v_i' v_i'}$ is now introduced and can be inserted into Boussinesq assumption, which is presented in Equation (2.15).

Boussinesq assumption:

$$\overline{\bar{\rho} v_i' v_j'} = -\mu_t\Big(\frac{\partial \bar{v}_i}{\partial x_j} + \frac{\partial \bar{v}_j}{\partial x_i}\Big) + \frac{1}{3}\overline{\bar{\rho} v_k' v_k'}\delta_{ij} = -\mu_t\Big(\frac{\partial \bar{v}_i}{\partial x_j} + \frac{\partial \bar{v}_j}{\partial x_i}\Big) + \frac{2}{3}\bar{\rho} k \delta_{ij} \tag{2.15}$$

A Boussinesq approach can be used to approximate the turbulent heat flux vector by linearly relating it with heat flux through the turbulent thermal conductivity κ_t. Here the turbulent thermal conductivity is related to the turbulent dynamic viscosity μ_t and turbulent Prandtl number σ_θ which is an empirical model constant. The Boussinesq assumption for closure of the turbulent heat flux vector is presented in Equation (2.16).

Boussinesq assumption:

$$\overline{\bar{\rho} v_i' e'} = -\kappa_t \frac{\partial \bar{e}}{\partial x_i}, \quad \kappa_t = \frac{\mu_t}{\sigma_\theta} \tag{2.16}$$

The Boussinesq assumption simplifies the previously twelve unknown variables to four unknowns (turbulent dynamic viscosity μ_t and the three diagonal elements of the Reynolds stress tensor $\overline{v_i'v_i'}$). It can further be simplified to two unknowns if the turbulent kinetic energy k is solved for instead of the diagonal elements of the Reynolds stress tensor.

Now, the URANS equation system can be closed and numerically solved if the turbulent dynamic viscosity is formulated with turbulent mean flow properties and a partial differential transport equation expressing the turbulent kinetic energy. Usually the turbulent dynamic viscosity is expressed with the turbulent kinetic energy and another turbulent quantity, thus requiring two additional transport equations including one for the turbulent kinetic energy. This methodology gives rise to the two-equation turbulence models and all their extensions, such as the $k-\varepsilon$ and $k-\omega$ turbulence models. [20]

2.1.3.1 The $k-\varepsilon$ turbulence model

In the $k-\varepsilon$ turbulence model, partial differential **transport equations for turbulent kinetic energy** k and **turbulent dissipation rate** ε are used to express the turbulent dynamic viscosity. The transport equations and expression for turbulent dynamic viscosity have been presented by Launder and Spalding [22] and shown here in Equation (2.17), (2.18) and (2.19).

Transport equations for turbulent kinetic energy:

$$\frac{\partial \rho k}{\partial t} + \frac{\partial \rho \bar{v}_i k}{\partial x_i} = \frac{\partial}{\partial x_i}\Big[\Big(\mu + \frac{\mu_t}{\sigma_k}\Big)\frac{\partial k}{\partial x_i}\Big] + P_k - \rho\varepsilon \tag{2.17}$$

Transport equations for turbulent dissipation rate:

$$\frac{\partial \rho \varepsilon}{\partial t} + \frac{\partial \rho \bar{v}_i \varepsilon}{\partial x_i} = \frac{\partial}{\partial x_i}\Big[\Big(\mu + \frac{\mu_t}{\sigma_\varepsilon}\Big)\frac{\partial \varepsilon}{\partial x_i}\Big] + \frac{\varepsilon}{k}(C_{\varepsilon 1} P_k - C_{\varepsilon 2}\rho\varepsilon) \tag{2.18}$$

$$\mu_t = C_\mu \rho \frac{k^2}{\varepsilon} \tag{2.19}$$

The turbulent dynamic viscosity is derived from dimensional analysis. The values σ_k, σ_ε, $C_{\varepsilon 1}$, $C_{\varepsilon 2}$ and C_μ are empirical model constants shown as numbers in Table 2.1. The variable P_k represents the production of turbulent kinetic energy, a source term expanded in Equation (2.20).

$$P_k = -\bar{\rho}\overline{v_i'v_j'}\frac{\partial \bar{v}_i}{\partial x_j} \tag{2.20}$$

The production of turbulent kinetic energy is modelled with the Boussinesq assumption.

Constant	C_μ	$C_{\varepsilon 1}$	$C_{\varepsilon 2}$	σ_k	σ_ε
Value	0.09	1.44	1.92	1	1.3

Table 2.1: Experimental constants for Standard $k - \varepsilon$ turbulence model.

The $k - \varepsilon$ turbulence model can be used as it is or expanded with more underlying realizable constraints and complex empirical constants for improved resolving of turbulence. In general the $k - \varepsilon$ turbulence model is a cheap, powerful and robust turbulence model which predicts turbulent free flows including small pressure gradients with good accuracy. However, it lacks capability to resolve flows in proximity to walls without further adjustments and additions of numerical models. In the studies by Iqbal and A. Selamet [17] and E. Selamet *et al.* [18, 19], the $k - \varepsilon$ turbulence model was used to predict turbulent air pipe flow including acoustic propagating waves with good accuracy.

2.1.3.2 The $k - \omega$ turbulence model

Wilcox [23] presented a new turbulence model by rewriting the transport equations in the $k-\varepsilon$ model to describe turbulent kinetic energy k and specific dissipation rate ω by relating $\omega \propto \varepsilon/k$. This led to the two-equation model called $k - \omega$ turbulence model. The model works in the same way as the $k - \varepsilon$ model but now describes the turbulent dynamic viscosity μ_t with turbulent kinetic energy k and specific dissipation rate ω. The governing equations in the standard $k - \omega$ turbulence model are presented in Equations (2.21), (2.22) and (2.23).

$$\frac{\partial \rho k}{\partial t} + \frac{\partial \rho \bar{v}_i k}{\partial x_i} = \frac{\partial}{\partial x_i}\Big[\Big(\mu + \frac{\mu_t}{\sigma_k^\omega}\Big)\frac{\partial k}{\partial x_i}\Big] + P_k - \beta^* \rho \omega k \tag{2.21}$$

$$\frac{\partial \rho \omega}{\partial t} + \frac{\partial \rho \bar{v}_i \omega}{\partial x_i} = \frac{\partial}{\partial x_i}\Big[\Big(\mu + \frac{\mu_t}{\sigma_\omega}\Big)\frac{\partial \omega}{\partial x_i}\Big] + \frac{\omega}{k}(C_{\omega 1} P_k - C_{\omega 2} \rho k \omega) \tag{2.22}$$

$$\mu_t = \rho \frac{k}{\omega} \tag{2.23}$$

The values β^*, $C_{\omega 1}$, $C_{\omega 2}$, σ_k^ω and σ_ω are empirical model constants shown as numbers in Table 2.2. The variable P_k represents the production of turbulent kinetic energy, a source term previously presented for the $k-\varepsilon$ turbulence model in Equation (2.20).

Constant	β^*	$C_{\omega 1}$	$C_{\omega 2}$	σ_k^ω	σ_ω
Value	0.09	0.44	0.0828	2	2

Table 2.2: Experimental constants for Standard $k - \omega$ turbulence model.

One advantage with $k-\omega$ model in comparison to $k-\varepsilon$ model is that boundary layer flow prediction is calculated with higher accuracy, especially for problems related to adverse pressure gradients. The $k-\omega$ model also has the capability to be applied through the full boundary layer without modifications of the model which $k-\varepsilon$ model is not capable of handling. However, the $k-\omega$ model is sensitive to free stream ω values which will affect the models sensitivity to boundary conditions and initial conditions. [20, 24, 25]

2.1.3.3 The SST $k-\omega$ turbulence model

The $k-\varepsilon$ and $k-\omega$ turbulence models were combined and developed by Menter [26] in the Shear Stress Transport (SST) model by utilization of blending functions. With Menter's SST approach, the advantages of each model separately were collected in the SST model to improve performance. To get the full advantage of each model, the blending function made it possible for the $k-\omega$ model to be used when calculating boundary layer flow and $k-\varepsilon$ model for free stream flow. Menter called it the SST $k-\omega$ model.

The SST $k-\omega$ model has seen extensive use in a wide array applications for complex turbulent flow problems like; strong swirling flow, streamline curvature, shear layer flow and/or boundary layer flow where anistropic turbulence is common. Eddy viscosity turbulence models tend to under predict anistropic turbulence and its representation in the Reynolds stress tensor due to the simplification being made. [24] To account for anistropic turbulence in the SST $k-\omega$ model, Spalart [27] suggested changing the linear constitutive relation in the Boussinesq assumption to a quadratic non-linear behaviour by adding and multiplying tensors of strain and vorticity.

2.1.3.4 Transition model

Menter et al. [28] developed a one-equation correlation based transition model for turbulent intermittency γ to improve prediction performance of turbulent boundary layer transition. The model solves the transport equation for turbulence intermittency as well as computing momentum thickness Reynolds number through local variables algebraically. The transport equation for turbulence intermittency γ is given in Equation (2.24).

$$\frac{\partial \rho\gamma}{\partial t} + \frac{\partial \rho v_i \gamma}{\partial x_i} = \frac{\partial}{\partial x_i}\Big[\Big(\mu + \frac{\mu_t}{\sigma_f}\Big)\frac{\partial \gamma}{\partial x_i}\Big] + P_\gamma - E_\lambda \tag{2.24}$$

Here σ_f is an empirical model constant, P_γ and E_λ represent production and destruction of turbulence intermittency respectively. The turbulence intermittency is introduced in the SST $k-\omega$ turbulence model's transport equation for turbulent kinetic energy through an additional production term. This increases the generation of k at points of transition for increased prediction capabilities of boundary layer flow transitions.

2.1.4 Boundary layer flow

Fluid flow adjacent to a solid wall is slowed down by shear stresses from wall friction forces causing the creation of a boundary layer flow. An illustrative picture of a developing two-dimensional boundary flow over an endless flat plate is shown in Figure 2.1. Initially, flow with a uniform velocity v_0 is introduced over the flat plate on the left side. A laminar boundary layer is starting to grow immediately close to the wall surface. When inertial forces in the fluid overcome viscous forces acting on the fluid, laminar boundary layer flow transitions into a more chaotic and irregular turbulent boundary layer flow. Now, the boundary layer flow in the closest proximity to the wall stays laminar due to the viscous forces. Moving further away from the wall, reduces influence of wall forces, increases turbulence and a fully turbulent region can be found. Between the flow closest to the wall and the outer parts of the boundary layer, a transitional region where laminar flow is transitioning in to turbulent flow is found. After a certain length downstream of the plate, the mean boundary layer flow will not change with respect to the wall normal direction thus a fully developed turbulent boundary layer flow is created with a velocity profile $v(y)$. [29]

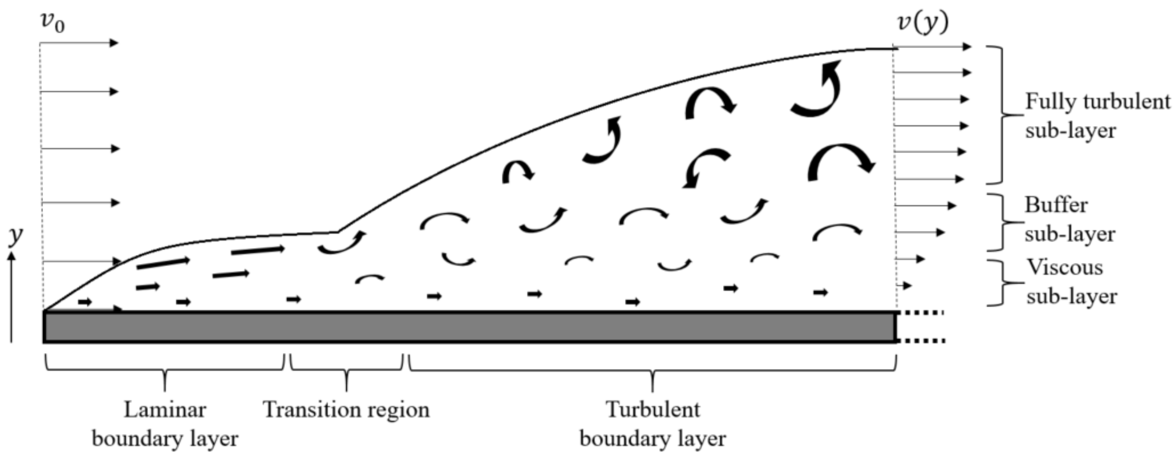

Figure 2.1: Schematic picture of the creation of boundary layer flow at a flat plate. [29]

An important variable to quantify flows in proximity to a wall is the non-dimensional wall distance y^+. It can be defined as

$$y^+ = \frac{v^* y}{\nu} \tag{2.25}$$

where ν is the kinematic viscosity, y is the general wall normal coordinate for a wall surface in three dimensions and v^* is the friction velocity. The friction velocity is defined as

$$v^* = \sqrt{\frac{\tau_w}{\rho}} \tag{2.26}$$

where τ_w is the wall shear stress. The wall shear stress is defined in Equation 2.27.

$$\tau_w = \mu \frac{\partial v}{\partial y}\bigg|_{y=0} \tag{2.27}$$

As the velocity drops down to zero at the wall over a small wall normal distance "∂y" due to high viscous forces, large velocity gradients are created inside the boundary layer. These rapid changes in velocity are generally much larger in comparison to free stream flow gradients or flow gradients in wall parallel direction. To predict the high gradients and capture the rapid changes of flow properties, high spatial resolution is required for the solution method. This way of fully capturing the boundary layer down to the wall is called **low-Reynolds number wall treatment**. The high spatial resolution can however be a problem due to insufficient computer resources and simulation time requirement. Hence, a common approach in how to circumvent this problem is to use wall functions. The wall functions are empirically established models for flow variables close to the walls. Thus, a solution for flow variables close to the wall can be acquired without the high spatial resolution with some sacrifice of wall flow accuracy. This methodology is called **high-Reynolds number wall treatment** or just **wall functions**. It can under certain circumstances be essential to use wall functions for some turbulence models like the standard $k-\varepsilon$ model which is not valid for flow close to the wall. [25]

Wall functions assumes that any arbitrary three dimensional wall bounded flow can analogously be described with a plate boundary layer flow. Here the non-dimensional wall distance is used as a parameter to describe the mean flow velocity profile close to the wall. The interesting regions that need to be modelled with wall functions can be seen in Figure 2.1; viscous, buffer and fully-turbulent sub-layer. In the viscous sub-layer, parallel flow velocity has experimentally and numerically shown to inherit a linear increase with y^+ in the range between $0 < y^+ < 5$. Further away from the wall $30 < y^+$, in the fully-turbulent sub-layer, flow velocity increases logarithmically following the law of the wall established by Kármán [30]. Between the two sub-layers $5 < y^+ < 30$, a transitional sub-layer called the buffer layer exists where flow velocity is transitioning between a linear to a logarithmic behaviour. For low-Reynolds-number wall treatments where all sub-layers are numerically captured, the first cell height in wall normal direction need to be chosen as $y^+ < 1$. Cell growth percentage in this region also need to be smaller than 20% for stability and spatial resolution requirement. In contrast, for high-Reynolds-number wall treatments to fully be utilized in describing wall bounded flows the first cell height in wall normal direction need to be set in the fully-turbulent sub-layer, far from the buffer sub-layer. A general recommendation is setting the height in the order of $50 < y^+ < 150$ to ensure that no cell height happens to exists in the buffer layer as wall functions perform poorly starting from inside the buffer layer. [20, 25, 31]

2.2 Acoustics

Acoustics is the scientific disciplinary of studying mechanical waves in solids, liquids and gases. The acoustics discipline include topics as vibrations and sound. This sub chapter will focus on sound wave propagation in gases, theory and sound interaction of a Helmholtz resonator and acoustical measuring techniques.

2.2.1 Acoustic wave theory

Acoustic oscillating waves (sound) in gases and liquids propagate in the medium as longitudinal waves, seen in 1D. In the medium the oscillations can be seen as regions of compression and expansion as the wave is propagating. Commonly, acoustic disturbances propagate as plane waves where acoustic properties such as sound pressure p_{ac} is constant in any plane perpendicular to the motion direction of the wave propagation. The propagating acoustic waves are governed by the **source-free linearized acoustic wave equation**. To define the wave equation in this simplified way, it must be assumed that

- the medium of the acoustic waves is homogeneous, isotropic and linearly elastic
- system is adiabatic
- viscous and gravitational effects are negligible
- acoustic fluctuations are small

Pressure and density in the medium can thereafter be decomposed in two quantities respectively; undisturbed constant quantities p_0, ρ_0 and acoustically disturbed quantities $p_{ac}(x, y, z, t)$ and $\rho_{ac}(x, y, z, t)$. [4]

$$\begin{aligned} p(x, y, z, t) &= p_0 + p_{ac}(x, y, z, t) \\ \rho(x, y, z, t) &= \rho_0 + \rho_{ac}(x, y, z, t) \end{aligned} \tag{2.28}$$

To define the wave equation one must first look at the **linear conservation equation of continuity** which relates density and particle velocity v_p in the medium. The decomposed definition of density have been inserted and higher-order terms are neglected. [4]

Linear conservation equation of continuity:

$$\frac{\partial \rho_{ac}}{\partial t} + \rho_0 \frac{\partial v_{p,i}}{\partial x_i} = 0 \tag{2.29}$$

The **linear inviscid conservation equations of momentum** are also needed. Assuming that viscous effects can be neglected, the equation system relates velocity of the sound wave with acoustic pressure. Here, higher-order terms are also neglected. [4]

Linear inviscid conservation equations of momentum:

$$\rho_0 \frac{\partial v_{p,i}}{\partial t} + \frac{\partial p_{ac}}{\partial x_i} = 0 \tag{2.30}$$

Equation (2.29) and (2.30) include five unknown variables to solve but only four equations, similarly as in fluid dynamics the **equation of state** must be used to complete the equation system. [4]

Equation of state for acoustics:

$$(p_0 + p_{ac}) = (\rho_0 + \rho_{ac})RT/M_m \tag{2.31}$$

The acoustic wave equation can then be defined by subtracting the time derivative of continuity (2.29) from the spatial derivative of momentum (2.30) and eliminating ρ_{ac} by inserting the equation of state (2.31). The governing acoustic wave equation is defined as

Source-free linearized acoustic wave equation:

$$\frac{\partial^2 p_{ac}}{\partial x_i^2} - \frac{1}{c^2}\frac{\partial^2 p_{ac}}{\partial t^2} = 0, \tag{2.32}$$

where the constant c is the speed of sound and defined as

Speed of sound:

$$c = \sqrt{\frac{\gamma p_0}{\rho_0}} = \sqrt{\frac{\gamma RT}{M_m}}, \tag{2.33}$$

defining the propagation speed of an acoustic wave in the medium. [4] The partial differential equation system from the linearized wave equation together with chosen boundary and initial conditions yields the possibility to calculate the sound field at any given time and space. The system of equations can be solved with an analytic solution (for certain studied geometries) as well as a numerical solution. To solve the equation system, the acoustic **wavenumber** must be defined

Wavenumber

$$k_w = \frac{\omega_f}{c} \tag{2.34}$$

where $\omega_f = 2\pi f$ is the acoustic angular wave frequency. [4] Assuming that the acoustic sound waves can be treated as a periodic process, the waves can therefore be defined mathematically in Fourier analysis by a summation of harmonic, sinusoidal functions with different frequencies, also called Fourier series. In the definition of Fourier series, each discrete frequency can be defined independently and the sound pressure field is a summation of all discrete frequency components at any given time and location. The **complex harmonic solution for free, one-dimensional, plane wave propagation** is defined as

Complex harmonic solution for free, one-dimensional, plane wave propagation:

$$\mathbf{p}(x,t) = \breve{p}_+ e^{i(\omega_f t - k_w x)} + \breve{p}_- e^{i(\omega_f t + k_w x)} \tag{2.35}$$

where the exponential argument $(2\pi f t \pm k_w x)$ defines the phase and $\breve{p}_{+/-}$ defines the pressure amplitude of the positively and negatively propagating acoustic wave in x-direction. [4] To interpret the complex sound pressure solution $\mathbf{p}$ in Equation (2.35), the real part of the solution is required

Real harmonic solution for free, one-dimensional, plane wave propagation:

$$p(x,t) = \breve{p}_+ \cos(\omega_f t - k_w x) + \breve{p}_- \cos(\omega_f t + k_w x). \tag{2.36}$$

However, the linearized wave equation in Equation (2.32) needs to be modified when solving acoustic wave propagation in ducts with mean flow. The **convective wave equation** can be written as

Source-free convective acoustic wave equation:

$$\frac{\partial^2 p_{ac}}{\partial x_i^2} - \frac{1}{c^2}\left(\frac{\partial}{\partial t} + v_u \frac{\partial}{\partial x_i}\right)^2 p_{ac} = 0, \tag{2.37}$$

assuming that a uniform constant cross-sectional velocity v_u is present in the duct. The equation system in Equation (2.37) can also be solved analytically and numerically but the solution will not be presented. However, applying the solution for a cylindrical duct system disregarding flow, it can be deduced which acoustic modes that are present in the duct acoustic wave propagation for a certain frequency range. Acoustic waves that propagate with a discrete frequency below the first "cut-on" frequency $f_{c,01}$ are defined as plane waves, first-order mode. This condition is important to fulfill, as it is a requirement to solve the modified acoustic wave equation. Propagating acoustic waves with higher frequency than the first "cut-on" frequency could propagate in higher-order modes. The "cut-on" frequency depends on the cross-sectional shape of the duct and can be defined as

"Cut-on" frequency:

$$f_{c,01} = 1.841\frac{c}{\pi D}, \tag{2.38}$$

where Equation (2.38) assumes rigid duct walls. [4] Finally, for further theoretical description the acoustic quantity **specific acoustic impedance** $z(\omega_f)$ is introduced as the ratio of the Fourier transform of acoustic pressure and particle velocity.

Specific acoustic impedance:

$$z(\omega_f) = \frac{\mathcal{F}[p_{ac}](\omega_f)}{\mathcal{F}[v_p](\omega_f)} = \frac{\hat{p}_{ac}}{\hat{v}_p} \tag{2.39}$$

The accent $\hat{}$ describes Fourier transform. Specific acoustic impedance is a measure on resistance of an acoustic system for acoustic propagation as a result of an acoustic pressure field present in the system. Impedance is a complex variable and can be decomposed in to a real and imaginary part; specific acoustic resistance $r(\omega_f)$ and specific acoustic reactance $x(\omega_f)$,

$$z(\omega_f) = r(\omega_f) + ix(\omega_f) \tag{2.40}$$

Here, the specific acoustic resistance describes the energy transfer of an acoustic wave when the pressure wave and motion of air is in phase. Specific acoustic reactance also describes energy transfer of an acoustic wave but when the pressure wave and motion of air is out of phase, resulting in no net average energy transfer. [32]

2.2.2 Helmholtz resonator

A Helmholtz resonator can geometrically be defined in many ways but, as described in the introduction chapter, it is always composed of an enclosed volume of air connected to a duct system with one or several necks. The Helmholtz resonator can analogously be seen as a mass-spring mechanical system. The column of air in the neck acts as a mass, oscillating rigidly back and forth, while the volume of air in the house acts as a spring, absorbing the external load from the neck oscillations. A Helmholtz resonator is maximally attenuated, fully dampening propagating duct acoustic waves, when the inlet specific impedance of the Helmholtz resonator is zero. Specific acoustic impedance is zero when the frequency of the sound waves matches the eigenfrequency of the Helmholtz resonator, causing a system resonance. Here the eigenfrequency of a Helmholtz resonator f_r can analytically be defined as

Helmholtz resonator eigenfrequency:

$$f_r = \frac{c}{2\pi}\sqrt{\frac{A_n}{V_c(L_n + \delta_n)}} \tag{2.41}$$

where c is the speed of sound, A_n the neck cross-sectional area, V_c the volume of the resonator house, L_n the length of the neck, and δ_n the end correction. A schematic illustration of a Helmholtz resonator can be seen in Figure 2.2 where incident, reflected and transmitted acoustic waves can be seen in the duct. The reflected wave in Figure 2.2 is a result of an induced impedance to the acoustic duct system caused by attaching the Helmholtz resonator to the duct system. [4]

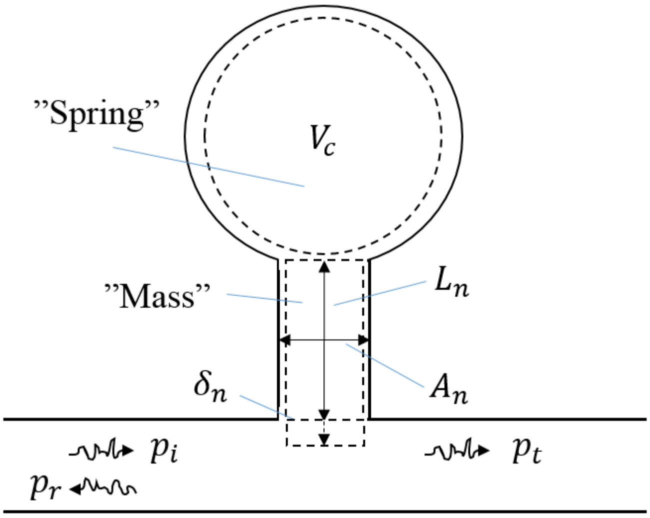

Figure 2.2: Schematic illustration of a Helmholtz resonator including duct acoustic behaviour in 2D. [4]

For complex geometrical designs of Helmholtz resonators, the analytic equation of eigenfrequency only gives a rough estimate due to the lumped definition. The lumped definition does not take effects of higher order modes of resonance into account which could exist due to the geometry itself. The end correction term in the Equation (2.41) describes an extension of air that is excited together with air inside the neck, increasing the effective length of the neck L_n, affecting the eigenfrequency of the system. [4] Usually, the end correction term is hard to define analytically but geometry and neck placement relative to the duct plays a key role. [4, 33]

2.2.3 Two-microphone method

Chung and Blaser [34, 35, 36] presented an experimental technique for duct acoustics, both with and without flow. The theory involves decomposition of a random acoustic signal (generated by a speaker) into its incident and reflected parts. The decomposition is performed using a transfer-function relation between the acoustic pressure at two microphone locations, schematically showed in Figure 2.3. By doing the decomposition it is possible to define the complex reflection coefficient that in turn can be used to determine important acoustic properties of the duct system.

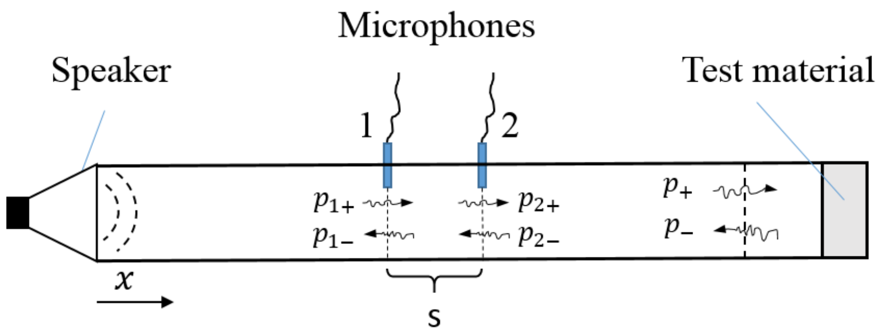

Figure 2.3: Incident and reflected acoustic pressure waves at duct section and microphones. [34, 35, 36]

The specific test apparatus setup in Figure 2.3 can measure the acoustic impedance and sound absorption coefficient of the test material but also generally for other acoustical systems and devices. Introducing a random acoustical wave in the duct as $p(x,t)$ as well as its values at the two microphone locations $p_1(t)$ and $p_2(t)$, they can be written in their decomposed form as

$$p(x,t) = p_+(x,t) + p_-(x,t) \tag{2.42}$$

$$\begin{aligned} p_1(t) &= p_{1+}(t) + p_{1-}(t) \\ p_2(t) &= p_{2+}(t) + p_{2-}(t) \end{aligned} \tag{2.43}$$

where $+$ represent propagating acoustic wave in positive x-direction (incident signal) and $-$ represent propagating acoustic wave in negative x-direction (reflected signal). Equations (2.44)-(2.48) relate their respective pressure signals with impulsive responses r_1, r_2, h_+, h_- and h_{12} using convolution integral.

$$p_{1-}(t) = \int_0^\infty r_1(\tau)\; p_{1+}(t-\tau)\; d\tau \tag{2.44}$$

$$p_{2-}(t) = \int_0^\infty r_2(\tau)\; p_{2+}(t-\tau)\; d\tau \tag{2.45}$$

$$p_{2+}(t) = \int_0^\infty h_+(\tau)\; p_{1+}(t-\tau)\; d\tau \tag{2.46}$$

$$p_{2-}(t) = \int_0^\infty h_-(\tau)\; p_{1-}(t-\tau)\; d\tau \tag{2.47}$$

$$p_2(t) = \int_0^\infty h_{12}(\tau)\; p_1(t-\tau)\; d\tau \tag{2.48}$$

where the impulsive responses are defined as:

- r_1 and r_2: Impulsive responses corresponding to the reflected signal evaluated at the first and the second microphone locations respectively. [34]
- h_+ and h_-: Impulsive responses corresponding to the incident and reflected signals, respectively evaluated between the first and the second microphone locations. [34]

- h_{12}: Impulsive response corresponding to the combined incident and reflected waves evaluated between the two microphone locations. [34]

Fourier transform of the impulsive responses r_1, h_+, h_- and h_{12} yields

$$R_1(\omega_f) = \mathcal{F}[r_1](\omega_f) = \frac{S_{1+,1-}(\omega_f)}{S_{1+,1+}(\omega_f)}, \tag{2.49}$$

$$H_+(\omega_f) = \mathcal{F}[h_+](\omega_f) = \frac{S_{1+,2+}(\omega_f)}{S_{1+,1+}(\omega_f)}, \tag{2.50}$$

$$H_-(\omega_f) = \mathcal{F}[h_-](\omega_f) = \frac{S_{1-,2-}(\omega_f)}{S_{1-,1-}(\omega_f)}, \tag{2.51}$$

$$H_{12}(\omega_f) = \mathcal{F}[h_{12}](\omega_f) = \frac{S_{1,2}(\omega_f)}{S_{1,1}(\omega_f)}, \tag{2.52}$$

where H_+, H_- and H_{12} are the acoustic transfer functions corresponding to their respective impulsive response. The quantity R_1 is called the complex reflection coefficient at the first microphone location. On the right-hand side of Equation (2.49)-(2.52), ratios of different spectral densities corresponding to different acoustic signals are equal to their respective acoustic transfer function. A value of S with two equal subscripts signal descriptions ($S_{1,1}, S_{1+,1+}$) denote a auto-spectral density of the two respective sub scripted acoustic pressure signals. Two different signal subscripts ($S_{1,2}, S_{1-,2-}$) correspond to cross-spectral density between the two acoustic signals. Equation (2.49)-(2.52) can be rearranged, giving rise to a new expression of the complex reflection coefficient which is useful for determining acoustic properties.

$$R_1(\omega_f) = \frac{H_{12}(\omega_f) - H_+(\omega_f)}{H_-(\omega_f) - H_{12}(\omega_f)}, \tag{2.53}$$

The complex reflection coefficient R_1 corresponds to the amplitude ratio of the reflected and incident pressure signals at the first microphone location according to Equation (2.49). The square of the absolute value of the acoustic transfer function H_{12} is introduced as

$$|H_{12}(\omega_f)|^2 = \frac{S_{2,2}}{S_{1,1}} = \frac{|\hat{p}_2(\omega_f)|^2}{|\hat{p}_1(\omega_f)|^2} \tag{2.54}$$

where the auto-spectral density of the total acoustic signal at microphone location one ($S_{1,1}$) and two ($S_{2,2}$) are also defined. It is possible to express the incident and reflect acoustic transfer function H_+ and H_- assuming; plane wave propagation, no mean flow, and neglecting losses at the tube wall, as:

$$\begin{aligned} H_+(\omega_f) &= e^{-ik_w s} \\ H_-(\omega_f) &= e^{ik_w s} \end{aligned} \tag{2.55}$$

where s is defined as distance between the two microphones. The microphone spacing is an important parameter when setting up the two-microphone measurement method as it decides which frequency band the technique is capable of capturing. From Equation (2.53), it can be seen that equation is indeterminate if $H_- - H_{12} = 0$, which occurs when the incident and reflected acoustic transfer functions are equal $H_+ = H_-$. The condition $H_+ = H_-$ occurs if:

$$\begin{aligned} & k_w s = n\pi, \quad n = 1, 2, 3, ..., \\ & \text{or} \\ & s = n\frac{\lambda}{2}, \quad n = 1, 2, 3, ..., \end{aligned} \tag{2.56}$$

Equation (2.56) implies that for discrete acoustic frequencies, the reflection coefficient is not valid when the microphone spacing is equal to an integer multiple of half the wavelength λ. This leads to the choice of microphone spacing, by knowing the highest frequency f_{max} of acoustic waves present in the measurement, the microphone spacing must follow the inequality:

$$s < \frac{c}{2f_{max}}. \tag{2.57}$$

By not following the inequality, discrete frequencies following Equation (2.56) will be unavailable in the measurement. [34, 35, 36] Bodén and Abom extended this requirement to

$$0.1\pi < k_w s < 0.8\pi \tag{2.58}$$

for reducing the total error when measuring acoustic signals with the two-microphone method. [37] When using the two-microphone method in a duct including duct mean flow, convective effects must be taken into account. The mean flow will affect the wave propagation speed of acoustic waves, acoustic waves moving in the same direction as the mean flow has increased propagation speed and vice-versa, $c \pm v_m$. Equation (2.55) for the incident and reflect acoustic transfer function is rewritten for a duct with mean flow as

$$\begin{aligned} H_+(\omega_f) &= e^{-ik_w s/(1+\mathrm{M})} \\ H_-(\omega_f) &= e^{ik_w s/(1-\mathrm{M})} \end{aligned} \tag{2.59}$$

where M is the average cross-sectional Mach number. [36] The convective effect also affects the microphone spacing, where the lower limit is governed by acoustic waves travelling in the same direction as the mean flow while the upper limit is controlled by acoustic waves propagating against the mean flow direction.

$$\frac{0.1(c + v_m)}{2f} < s < \frac{0.8(c - v_m)}{2f} \tag{2.60}$$

2.2.4 Transmission loss

There are several acoustic quantities to define the noise mitigating performance of a silencer in a duct system. The most common quantities are noise reduction (NR), insertion loss (IL) and transmission loss (TL). The NR is defined as the difference in sound pressure level (SPL) before and after the silencer. A quantity that is easy to measure and calculate but does not say much about the silencing characteristics. The IL is calculated as the difference in SPL at a point outside the duct-silencer system, with and without silencer attached to the duct. IL yields a better picture of the silencing characteristics and can be useful in industrial applications. However, IL is not easy to calculate and very case specific as it depends on silencer geometry but also the acoustic source and duct radiation properties. Finally, the TL is a measure of difference in sound power level between incident and transmitted propagating acoustic wave, entering and exiting the silencer in the duct. The calculation of TL generally assumes that the duct termination is anechoic, no reflections of acoustic waves from the duct termination interfering with the measured incident and transmitted acoustic waves. TL ends up being an acoustic property of the silencer itself and hence is a good property to compare different silencer designs. However, TL is hard to measure experimentally due to the anechoic termination requirement but can be surpassed with different methodologies. This sub chapter aims to introduce and explain two different approaches in how to measure TL for a silencer-duct system. [4, 38]

2.2.4.1 Decomposition method

The first presented method for calculating transmission loss is called the decomposition method. The method is based on the two-microphone method, wave decomposition is performed before and after the silencer to separate the sound pressure in its incident and reflected waves. The drawback with the decomposition method is the strict requirement of anechoic termination. A fully anechoic termination is hard to achieve in a real experimental environment as well as in a numerical setup. Decomposition method can be used with and without flow. TL with decomposition method is defined as

$$\mathrm{TL} = 10\log_{10}\frac{W_i}{W_t} \tag{2.61}$$

where W_i and W_t denote incident and transmitted sound power level of the acoustic wave present in the silencer-duct system. The incident and transmitted sound power level can be determined from the complex reflection coefficient measured upstream (u) and downstream (d) of the silencer using the two-microphone method. Introducing upstream and downstream reflection coefficients R_u and R_d and the sound power levels can be calculated according to:

$$W_i = \frac{S_{uu}A_u}{\rho c|1+R_u|^2} \tag{2.62}$$

$$W_t = \frac{S_{dd}A_d}{\rho c|1+R_d|^2} \tag{2.63}$$

where S_{uu} and S_{dd} represent auto-spectral density upstream and downstream of the silencer. The values A_u and A_d correspond to the duct cross-section area upstream and downstream of the silencer. A schematic picture of an experimental setup using the decomposition method including flow is shown in Figure 2.4.

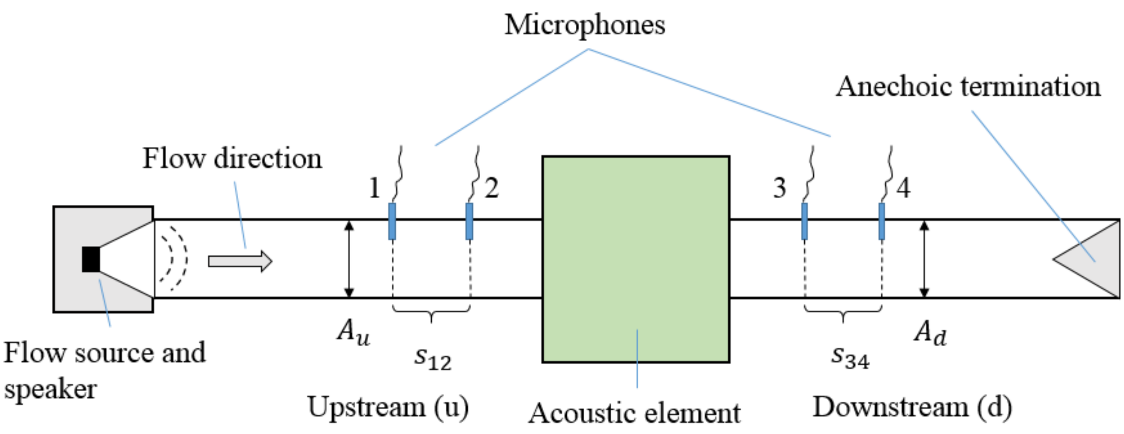

Figure 2.4: Experimental acoustic measurement setup to use the decomposition method with flow. [34, 35, 36, 38]

Inserting Equation (2.62) and (2.63) into Equation (2.61) yields a formulation for TL depending on complex reflection coefficient, duct cross-sectional area and acoustical element transfer function shown in Equation (2.64).

$$TL = 20\log_{10}\left|\frac{1+R_d}{1+R_u}\right| - 20\log_{10}|H_t| + 10\log_{10}\frac{A_u}{A_d} \tag{2.64}$$

Here, H_t corresponds to the transfer function for the measured acoustical element defined as

$$|H_t| = \left|\frac{S_{dd}}{S_{uu}}\right|^{1/2}. \tag{2.65}$$

Equation (2.64) can be simplified if it is assumed that;

- upstream and downstream cross-sectional areas are close to equal $A_u \approx A_d$
- non-dimensional wavenumber is constant through the acoustical element, $(k_w s)_u = (k_w s)_d$ leading to $H_{u+} = H_{d+}$ and $H_{u-} = H_{d-}$

- average cross-sectional Mach number upstream and downstream of the acoustical element is close to equal $\mathrm{M}_u \approx \mathrm{M}_d$

Using Equation (2.53) from two-microphone theory to define the reflection coefficient, it is possible to rewrite Equation (2.64) as

$$TL = 20\log_{10}\left|\frac{H_{-} - H_{12}}{H_{-} - H_{34}}\right| - 20\log_{10}|H_t| \tag{2.66}$$

where H_{12} and H_{34} is the transfer function between the two microphone pairs upstream and downstream of the acoustical element. Assuming $S_{uu} = S_{11}$ and $S_{dd} = S_{33}$ for H_t, using the definition of auto-spectral density and utilizing Equation (2.54) for H_{12} and H_{34}, Equation (2.66) can now be written in its final form as

$$TL = 20\log_{10}\left|\frac{\hat{p}_1(\omega_f)e^{ik_{wr}s} - \hat{p}_2(\omega_f)}{\hat{p}_3(\omega_f)e^{ik_{wr}s} - \hat{p}_4(\omega_f)}\right| \tag{2.67}$$

where k_{wr} is the reflected wavenumber, $k_{wr} = \frac{k_w}{1-\mathrm{M}} = \frac{2\pi f}{c(1-\mathrm{M})}$. Equation (2.66) is the final form of the decomposition method used when calculating TL in the simulation. Hence, acoustic pressure signals are needed at two positions in the duct before and after the silencer as well as an average Mach number. [34, 35, 36, 38]

2.2.4.2 Two-source method

The second method to calculate TL is called the two-source method, based on four-pole theory (two-port network). An arbitrary acoustical element in a duct system can be modelled with its four-pole parameters. The four-pole theory relates acoustic pressure and particle velocity before and after an acoustic element with a transfer matrix assuming plane wave propagation. By knowing the transfer matrix it is possible to calculate TL for the acoustic element. A schematic picture of the four-pole technique is shown in Figure 2.5. The transfer matrix is defined for the system as

$$\begin{bmatrix} \hat{p}_1(\omega_f) \\ \hat{v}_{p,1}(\omega_f) \end{bmatrix} = \begin{bmatrix} A & B \\ C & D \end{bmatrix} \begin{bmatrix} \hat{p}_2(\omega_f) \\ \hat{v}_{p,2}(\omega_f) \end{bmatrix} \tag{2.68}$$

where $\hat{p}_1$ and $\hat{p}_2$ are the Fourier transforms of the acoustic pressure signals before and after an acoustic element. The quantities $\hat{v}_{p,1}$ and $\hat{v}_{p,2}$ correspond to the Fourier transform of the particle velocity signals before and after an acoustic element. Finally, the values A, B, C and D represent the four-pole parameters of the acoustic element.

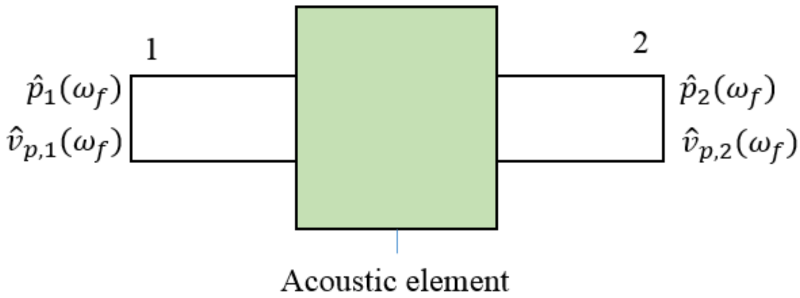

Figure 2.5: Definition of four-pole transfer matrix for acoustical element assuming positive particle velocity to the right. [38]

The four-pole parameters can not be calculated directly by measuring sound pressure and particle velocity in the duct as the equation system includes two equations and four unknown parameters. There are several different measuring methods in how to calculate the four-pole parameters and the two-source method is one of them. The two-source method can be used both with and without duct flow. In the two-source method, two different measuring configurations are created. Configuration a looks similar to the decomposition method setup, flow and acoustic source are located on the same side of the acoustic element. Now, the acoustic particle velocity signal is needed but hard to measure directly. However, the particle velocity signal can be calculated using the two-microphone method and thus two microphones are located both upstream and downstream of the acoustic element. Configuration a yields acoustic pressure signal and particle velocity signal before and after the acoustic element. The second configuration b changes the location of the acoustic source to the downstream side, where acoustic waves will move upstream against the flow. Acoustic pressure signals and particle velocity signals are captured again at the same microphone locations as in configuration a. A schematic drawing of the measurement setup and the two acoustic source configurations can be seen in Figure 2.6.

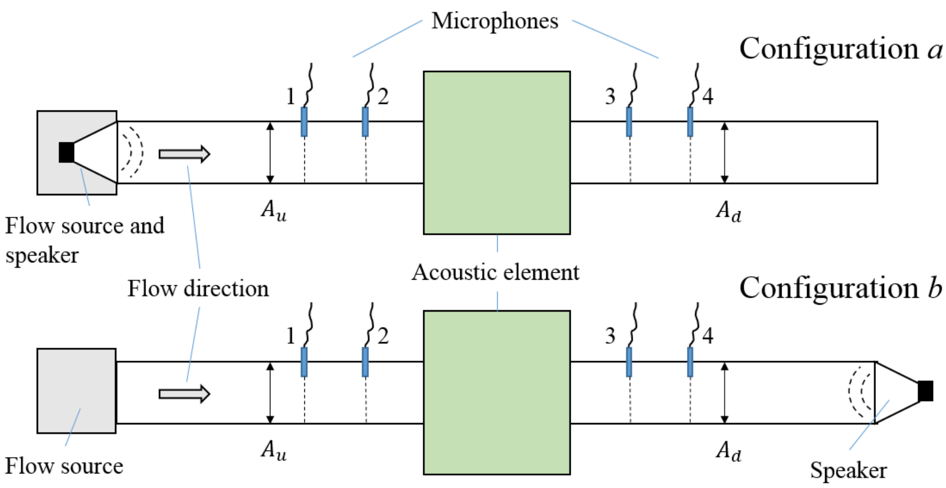

Figure 2.6: Experimental acoustic measurement setup to use the two-source method with flow. [38]

Assuming that the particle velocity signal is directly known at the microphone two and three, two matrix multiplications and one system of equations can be defined in Equation (2.69) and (2.70). A change when defining the two-port matrix for configuration b occurs because the direction of the propagating acoustic waves is changed.

$$\begin{bmatrix} \hat{p}_{2a}(\omega_f) \\ \hat{v}_{p,2a}(\omega_f) \end{bmatrix} = \begin{bmatrix} A_{23} & B_{23} \\ C_{23} & D_{23} \end{bmatrix} \begin{bmatrix} \hat{p}_{3a}(\omega_f) \\ \hat{v}_{p,3a}(\omega_f) \end{bmatrix} \tag{2.69}$$

$$\begin{bmatrix} \hat{p}_{3b}(\omega_f) \\ \hat{v}_{p,3b}(\omega_f) \end{bmatrix} = \begin{bmatrix} A_{23} & -B_{23} \\ -C_{23} & D_{23} \end{bmatrix}^{-1} \begin{bmatrix} \hat{p}_{2b}(\omega_f) \\ \hat{v}_{p,2b}(\omega_f) \end{bmatrix} = \frac{1}{\Delta} \begin{bmatrix} D_{23} & B_{23} \\ C_{23} & A_{23} \end{bmatrix} \begin{bmatrix} \hat{p}_{2b}(\omega_f) \\ \hat{v}_{p,2b}(\omega_f) \end{bmatrix} \tag{2.70}$$

Here, $\Delta = A_{23}D_{23} - B_{23}C_{23}$ represents the determinant of the four-pole matrix. Now, the unknown four-pole parameters can be calculated using the four equations in the equation system. The TL can thereafter be calculated using the four-pole parameters according to

$$\mathrm{TL} = 20\log_{10}\left\{\frac{1}{2}\left|A_{23} + \frac{B_{23}}{\rho c} + \rho c \cdot C_{23} + D_{23}\right|\right\} + 10\log_{10}\frac{A_u}{A_d} \tag{2.71}$$

where the second term can be neglected if the cross-sectional area is equal on the upstream and downstream side of the acoustic element. The positive thing about the two-source method is that it neglects the influence of reflections at the inlet and outlet boundaries. Making the method less sensitive to reflection errors from the boundaries. However, the method require two measurements setups for one geometry and hence is more time consuming than the decomposition method. [4, 38]

2.3 Flow effect on a Helmholtz resonator

When mean flow is present in a duct including sound waves, grazing the orifice of the Helmholtz resonator, the acoustic communication between the Helmholtz resonator and sound propagation is degraded. A strong shear layer is created at the resonator orifice between the semi-stagnant neck air and moving duct fluid. The fluid will travel inside the resonator cavity through the neck, often creating a large recirculation in the neck and house cavity as the fluid flows out of the resonator. Initially, if flow is introduced in a stagnant duct a transient behaviour occurs where flow will move in and out of the Helmholtz resonator cavity in pulses. When the flow has fully developed, a complex steady flow behaviour between resonator and duct is present. Especially when complex turbulent duct flow interferes with a geometrically complex multi-neck Helmholtz resonator. Hence, the neck region where fluid-sound interactions occur is the most important part when studying the degradation of acoustic performance for Helmholtz resonators with duct mean flow. A schematic drawing of how a steady flow pattern could look like for a single-neck Helmholtz resonator is shown in Figure 2.7.

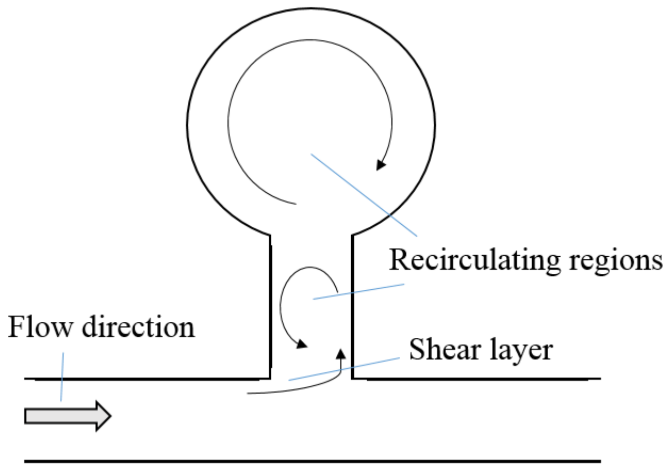

Figure 2.7: Schematic illustration of a Helmholtz resonator including duct mean flow, not definitive.

It has been noted that the specific acoustic resistance r of a Helmholtz resonator is almost linearly proportional to the grazing flow speed. The specific acoustic reactance x of a Helmholtz resonator is at the same time decreasing with grazing flow speed. The diminishing reactance could possibly be explained by a loss and reduction of the orifice end correction. The grazing flow destroys the duct-resonator interaction, reducing the effective length of the neck by taking away parts of the effective inertial mass that oscillates in the neck. This can be described by a reduction of end correction and thus the eigenfrequency of the Helmholtz resonator is increased with increasing duct mean flow. [5, 6, 7, 8, 9, 17]

Performance in this case is evaluated in transmission loss which is heavily impacted by the flow as TL peaks at resonator eigenfrequency. As the eigenfrequency is increased with increasing grazing flow speed, so is the TL peak. Transmission loss is also inversely proportional to the absolute magnitude of the specific acoustic impedance,

$$\mathrm{TL} \propto \frac{1}{|r(\omega_f) + ix(\omega_f)|} \tag{2.72}$$

which explains why amplitude of TL is reduced with increasing duct mean flow. [17, 18, 19, 39]

Turbulent fluctuations in a shear layer at the orifice could also attenuate and excite the resonator if the oscillating turbulent frequency matches the eigenfrequency of the resonator. If turbulent flow and its fluctuations are present in the duct they could be damped by the resonator causing a reduction in turbulence intensity. [40] However, the turbulent fluctuations could also generate sound waves at the orifice by itself or together with duct propagating sound. An oscillating separation of flow between the upstream (leading) and downstream (trailing) edge could create a self-sustained acoustic oscillator (whistle) directly related to the Strohaul number. The Strohaul number can be defined according to

$$\mathrm{St} = \frac{fL}{V} \tag{2.73}$$

where f is oscillating frequency of flow separation (vortex shedding), L characteristic length (neck diameter for a Helmholtz resonator) and V is the characteristic flow velocity. Instabilities occur at discrete ranges of the Strohaul number, most prominent where it corresponds to the two first acoustical modes, $\mathrm{St} = 0.3 - 0.4$ and $\mathrm{St} = 0.6 - 0.9$. [17, 41, 42]

3

Geometry

The given part of the air intake system including the silencer is presented in this section. In the engine, this part of the duct system is positioned directly after the air filter box and before the turbo-compressor. Schematic pictures of the received CAD-geometry are shown in Figure 3.1. The geometry includes two expanding duct parts in the duct terminations, which are not part of the real geometry in the engine. These expanding parts are however included in the experimental study that is used for comparison to the numerical data obtained in this study. The expanding parts are therefore included in the geometry definition since this study aims to predict the silencer acoustic performance under duct flow while being comparable to the experimental setup. The studied silencer of the air intake system can be seen in Figure 3.1 as the two protrusions. The silencer is composed of two serially positioned Helmholtz resonators, where each protrusion represent one of the resonators. Two corrugated duct parts, one large upstream of the bend and one smaller downstream of the two Helmholtz resonator (flow inlet positioned in the lower right of Figure 3.1a are also part of the geometry.

In Figure 3.2, the necks of the two Helmholtz resonators can be seen. Each resonator connects to the duct with a multitude of necks. Helmholtz resonator one has 25 necks (five rows of five necks) and resonator two has 35 necks (seven rows of five necks). It can be seen that the neck rows align with the duct direction. The two resonators can therefore be called multi-neck Helmholtz-like resonators since the resonators are mixes between a Helmholtz resonator and a perforated duct silencer. Figure 3.3 shows how the necks are connected to the resonator cavity. In Table 3.1, the geometrical variables and their respective values of the studied air intake system part and silencer are presented. The diameter of the expanded duct part D_{exp} is varying slightly due to design and manufacturing. The length of the necks L_{neck} are also slightly varying, the rows furthest away from the center are longer than the center-row of necks to have a constant distance between the resonator cavity and duct under the cavity. Using the analytic definition of Helmholtz resonator eigenfrequency presented in Section 2.2.2, the eigenfrequency of the two resonators can be estimated with the resonator geometry values of Table 3.1. Calculating the volume of the two resonator cavities as 3.09e-4 m^3 and 3.928e-4 m^3 and using the total neck area for each resonator yields an eigenfrequency approximation of resonator one as 760 Hz and resonator two as 799.6 Hz, without considering neck end correction.

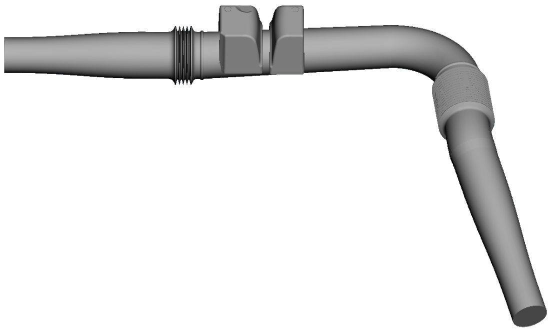

(a) Side view

(b) Top view

Figure 3.1: Unaltered real geometry of given air intake duct-silencer system, Helmholtz resonator 1 (right) and 2 (left) in (a) as the cavities.

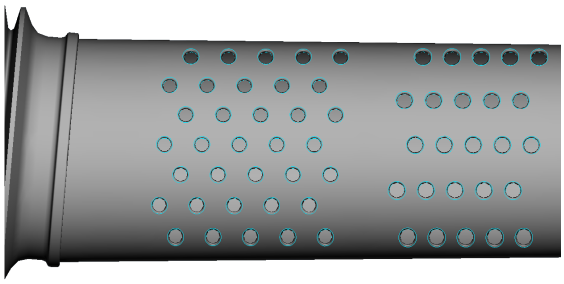

(a) Top view

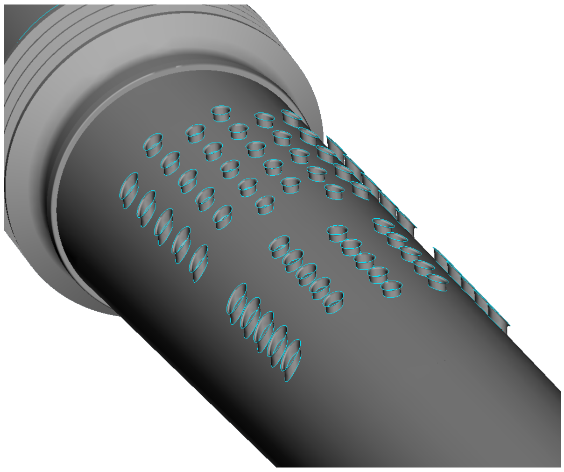

(b) Side view

Figure 3.2: Geometry of the resonator necks.

Variable	$D_{in,out}$	D_{exp}	D_{neck}	L_{neck}	N_{neck}
Value	57 mm	70-74 mm	4.5 mm	2-3 mm	25,35 (60)

Table 3.1: Geometrical variables of the given air intake system including silencer.

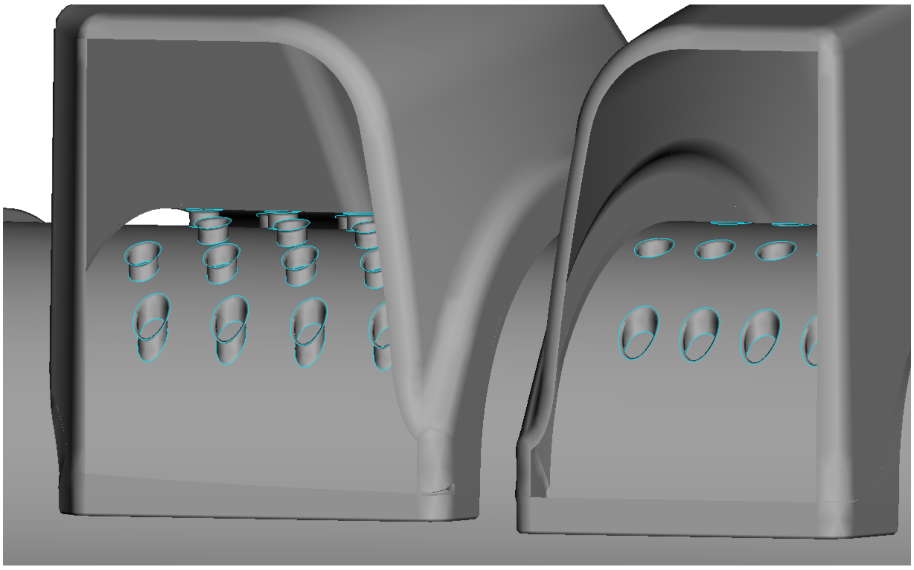

Figure 3.3: Geometry of resonator cavities including internal connection to resonator necks, walls removed for visual improvement.

4

Methods

In the following chapter, all methodologies used or studied are presented. The chapter is divided in three parts: numerical methodology, experimental methodology and simulation methodology. The section of numerical methodology describes all mathematical methods used to solve fluid dynamics numerically. An experimental study performed at KTH separately from this project is briefly introduced in the experimental methodology section. The simulation section describes both CFD setup and acoustic CAE setup, with emphasis on CFD.

4.1 Numerical methodology

This sub chapter aims to present the numerical methods used in the further simulations to describe the mathematical models presented in Chapter 2. Only numerical methods related to CFD and how the methods are implemented in Star-CCM+ are of interest. This means that numerical methods related to the acoustic CAE are not presented.

4.1.1 Finite volume method for unsteady flows

The finite volume method (FVM) discretizes continuous PDE into sets of algebraically solvable equation systems, making it possible to solve complex transport problems numerically. Initially, the spatial computational domain is divided in a finite number of cells, in this case volume-cells as the problem presented in this thesis is 3D. The first step is called creating a mesh or spatial grid. The PDE governing the computational domain is then integrated in each volume-cell using the divergence theorem and with FVM, algebraic equations for each cell are obtained. Information about flow variables is stored in the centre of cells called cell-nodes. The flow variables are cell-averaged meaning that any flow variable is spatially constant inside each cell. Hence, spatial resolution of the solution is directly limited by the cell sizes. The FVM also fulfills conservativeness for a transport property ϕ in the whole computational domain. Where the flux of ϕ leaving a cell through the cell-boundary (cell-face) must be equal to the flux of ϕ entering the neighbouring cell through the same shared boundary. The FVM has the capability to be expanded, describing discretization of time-dependant PDE. The finite volume integration described above is initially done over a computational domain and then the PDE is integrated over a finite time step Δt. Through the divergence theorem and FVM, the integrals corresponding to both the temporal and spatial dimension can be discretized in algebraic equation systems. [31]

A transient convective-diffusion PDE describing an arbitrary transport property ϕ can be written as

$$\underbrace{\frac{\partial \rho \phi}{\partial t}}_{T} + \underbrace{\frac{\partial \rho v_i \phi}{\partial x_i}}_{C} = \underbrace{\frac{\partial}{\partial x_i}\left(\Gamma \frac{\partial \phi}{\partial x_i}\right)}_{D} + S(\phi) \tag{4.1}$$

- T: Transient term
- C: Convection term
- D: Diffusion Term

where Γ is the diffusion coefficient and S is a source term possibly depending on ϕ. The governing equations for flow variables in Chapter 2: $\bar{v}_i$, T, k, ε, ω and γ are defined in a similar fashion as the PDE in Equation (4.1). An exception to this is the conservation equation of continuity in Chapter 2 which is defined as a transient convection problem and hence is discretized slightly different since the diffusion term is missing. Through integration in time and space, Equation (4.1) can be written algebraically with FVM and a fully implicit time discretization as

$$a_P^{(1)} \phi_P^{(1)} = \sum_{nb} a_{nb} \phi_{nb}^{(1)} + a_P^{(0)} \phi_P^{(0)} + S_u \tag{4.2}$$

where $a_P^{(1)}$, $a_P^{(0)}$, S_u and S_p are defined as

$$a_P^{(1)} = \sum_{nb} a_{nb} + a_P^{(0)} - S_p, \tag{4.3}$$

$$a_P^{(0)} = \rho^{(0)} \frac{\Delta V}{\Delta t}. \tag{4.4}$$

$$\int_{\Omega_{cd}} S(\phi) dV = \tilde{S} \Delta V = S_u + S_p \phi_P \tag{4.5}$$

In these equations;

- $\phi_P^{(0)}$ and $\phi_P^{(1)}$: Values of arbitrary transport variable in present cell at time t and $t + \Delta t$ respectively
- $\phi_{nb}^{(1)}$: Values of arbitrary transport variable in neighbouring cells at time $t + \Delta t$
- $\tilde{S}$, S_u and S_p; Cell-average source strength, constant- and first order transport variable depending -source amplitudes respectively

- $a_P^{(0)}$ and $a_P^{(1)}$: Discretization coefficients corresponding to the present cell at time t and $t + \Delta t$ respectively
- a_{nb}: Discretization coefficient corresponding to the present cell's interaction with neighbouring cells.
- $\int_{\Omega_{cd}} dV$ and ΔV: Volumetric integral of computational domain and volume of present cell

The discretization coefficients a_P and a_{nb} depend on the chosen spatial discretization scheme, approximating values of the studied transport variable on cell-boundaries and nodes. The algebraic equation system can be written in many different ways in regards to which time step t or $t + \Delta t$ transport variables are evaluated at, determined by the temporal discretization scheme. By choosing the appropriate spatial and temporal discretization scheme, the discretization coefficients and fundamental structure of Equation (4.2) can be determined, yielding a numerically solvable algebraic equation system. [31]

4.1.2 Spatial discretization scheme

When a general PDE like Equation (4.1) is integrated over a discrete volume in a computational domain, the different terms need to be discretized mathematically in the volume mesh. The convection and diffusion term can be discretized using many different spatial numerical schemes that aims to describe the studied transport property at the boundary of the present cell. The diffusion term is generally discretized with the central differencing scheme where a cell boundary transport variable value is interpolated using the closest cell-node values. The convection term on the other hand requires additional informational input in the numerical scheme from flow direction. The first-order upwind spatial scheme calculates the cell boundary transport variable value between two cells in a local flow with the first upstream cell's value. For increased spatial accuracy, the convection term can be discretized with the second-order upwind scheme where a cell boundary value is calculated using the two closest upstream cell values. [31]

Fluid calculations including acoustic wave propagation are very sensitive to the choice of spatial discretization scheme. Using lower-order schemes often result in high numerical diffusion in the solution for both fluid data and especially the small scale acoustic perturbations values. Numerical diffusion or dissipation is the effects of using low-order schemes, low spatial and temporal resolution leading to a solution incapable of producing highly accurate results for small numerical fluctuations as turbulence or acoustics. A mix of using both higher-order central differencing and upwind scheme is common for aeroacoustic simulations but mostly used for more complex numerical models including large eddy simulations (LES), detached eddy simulations (DES) or DNS to resolve acoustic noise generation.

4.1.3 Temporal discretization scheme

As introduced earlier, a temporal discretization scheme is needed when a transient PDE is integrated in time between t and $t + \Delta t$ as well as the spatial discretization. The transient transport variable values need to be evaluated at a certain time between t and $t + \Delta t$ in the computational domain. The FVM was presented earlier with the fully implicit temporal discretization scheme which evaluates transport variables in the next-coming time step $t + \Delta t$. However, transport variables are not explicitly known in the future time step and thus an internal iteration to find the values for the implicit time integration is required. The implicit discretization scheme is unconditionally stable, meaning that the iterative solution in space and time is stable for all values of chosen time step. If a large time step is chosen, more internal iterations are needed. On the other spectrum of evaluating transport variables in time, it is possible to calculate values for the next time step $t + \Delta t$ using only transport variable values from the old time step t. This is called the explicit temporal discretization scheme and does not require an internal integration as all transport values are already known. However, explicit time integration is not unconditionally stable. If the time step of the simulation is not chosen sufficiently small, the iterative solution looses robustness and could diverge. The requirement on a sufficiently small time step could possibly result in a highly computationally expensive simulation. Generally the explicit scheme is more expensive than the fully implicit time integration even though a second internal iteration is required. A mix between evaluating the future time step with both the old and the new time step also exists, for example the Crank-Nicholson scheme. [31]

Aeroacoustic simulations require a high order of accuracy in the simulation which also extends to the choice temporal discretization scheme. However, the choice of temporal scheme is mostly dictated by choice of turbulence model and thus available computational resources. But generally, second-order fully implicit time discretization is sufficient to solve aeroacoustic problems with both acoustic wave propagation and noise generation for all types of numerical models.

4.1.4 Flow and energy coupling

The governing equations of fluid dynamics in 3D described in Chapter 2 include five governing PDE and one equation of state to solve for six unknown flow transport variables assuming that material properties and source terms are known. It is then possible to list the flow variables needed to solve each equation and what flow variable the equation solves for:

- v_i → Continuity equation → ρ
- $\rho,\ p$ → Momentum equations → v_i
- $\rho,\ p,\ v_i$ → Energy equation → T
- $\rho,\ T$ → Equation of state → p

where the variables on the left-hand side are input values and the values on the right-hand side are output values for the respective equation.

The equation system can be solved in two ways; coupled or segregated. In the coupled flow and energy solver, all equations that govern the fluid are solved simultaneously with proper initialization and boundary conditions of transport variables. The coupled solver is often time and memory consuming but performs well even when the spatial and temporal resolution is low, compared to the segregated flow and energy solver. The segregated flow and energy solver integrates and calculates all governing equations in a sequential order. Each governing equation is iteratively solved separately from the other equations. Most often, the segregated solver requires additional numerical methods for incompressible, isothermal system or non-gaseous materials because the pressure field is not solved explicitly from the governing equations. Hence, the pressure field is linked to the velocity field though the continuity equation, called pressure-velocity coupling. However, if the governing equations are to solve flow for a compressible, thermally varying and gaseous fluid, pressure can be obtained through the equation of state $p = p(\rho, T)$. [31]

4.1.5 Convergence criteria

To evaluate if a numerical solution has reached sufficient amount of convergence for the calculated governing equations, it is of interest to observe the flow variable residuals in each numerical iteration. Convergence is achieved when all initial simulation flow fluctuations have stopped and the solution is not varying after each iterative solution step. Convergence principles can be applied to periodically unsteady flow phenomenons as well and not just steady problems. Residuals are one way to numerically monitor if convergence has been reached and is defined as the imbalance between the left-hand and right-hand side of a discretized transport equation, see Equation (4.2). Introducing a unscaled residual for an arbitrary steady transport variable as Λ_ϕ, which can be calculated with summation of residual errors in all cells as

$$\Lambda_\phi = \sum_{i=1}^{N_{cell}} \left| \sum_{nb} a_{nb}\phi_{nb} + S_u - a_P\phi_P \right| \tag{4.6}$$

where N_{cell} denotes the total number cells in the mesh. As flow variables exists in vast amount of different values, so will the residuals that are calculated from the respective flow variable residual equation. To be able to compare and relate different residuals it is necessary to scale the residual with a factor to make the residuals dimensionless.

When performing unsteady simulations it is often a good idea to start with a steady simulation of the same flow problem prior to calculating the unsteady solution. Ensuring that the steady simulation reaches convergences will reduce the time necessary to reach convergence in the unsteady simulation. When using the fully implicit temporal scheme, an internal iteration process to solve the next time step is required. Each iteration process has to reach convergence in the solution until moving to the next time step.

4.2 Experimental methodology

A flow acoustic study was performed at the Marcurs Wallenberg Laboratory for Sound and Vibration Research at the Royal Institute of Technology (KTH) in Stockholm on several silencer-duct systems. The study was performed separately from this Master's thesis project with limited amount of information regarding the methodology of the experimental setup. In these studies however, the presented geometry of this project was also studied. The transmission loss characteristics with duct mean flow were studied for four discrete flow speeds: 0, 21, 41 and 61 m/s. The flow speed is measured in the middle of the duct (top speed). In Figure 4.1, both the studied silencer-duct system (up-side down) and full measurement setup of the lab can be seen. It can be seen how the expanding parts of the ducts described in Section 3 is used in the experimental setup to fit the silencer-duct part to the flow measurement setup, the white duct part in Figure 4.1b. A schematic picture of the experimental setup is non-existent. The measurement setup is based on the two-source method presented in Section 2.2.4.2.

All measurements are performed using narrow band analyses with white noise excitation in the frequency band of 0-3200 Hz and a frequency resolution of 2 Hz. The measured pressure signals need to be sampled over a time to reduce influence of noise in the signal. The flow speeds between 21 and 41 m/s use 10000 samples when averaging the pressure signals from the experimental microphones. The maximum flow speed could only average around 5000 samples due to a limitation in the capacity of the system (overheat problem). The no-flow conditions uses a sample size of 2000. Six microphones are used in total to measures the acoustic pressure signal at various locations. The microphones are numbered in relation to the flow inlet, where number 1 is the most upstream microphone and number 6 at the most downstream.

The microphone spacing between microphone 1 and 2 as well as 2 and 3 (upstream microphones) is 34.25 mm. The distance between the downstream microphones 4 and 5 as well as 5 and 6 is 35 mm. The distance between the upstream connection ring (expanding silencer-duct parts connects to flow pipe) and microphone 3 is 305 mm and the distance between microphone 4 and the downstream connection ring is 435 mm. The inner pipe diameter is 57 mm.

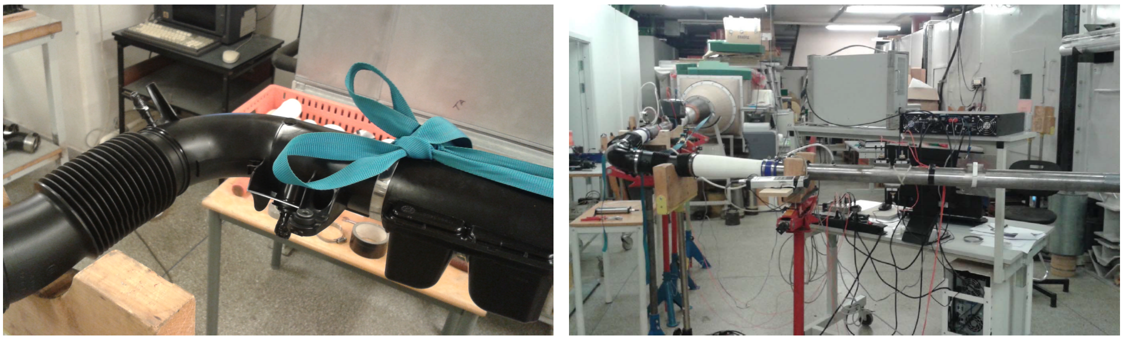

(a) **(b)**

Figure 4.1: Measurement setup of the experimental study on given silencer-duct system, (a) close picture of the geometry and (b) overview of the whole setup.

4.3 Simulation methodology

This section describes the simulation setup both for the different CFD simulations as well as the acoustic CAE simulations briefly.

4.3.1 CFD

The full simulation methodology and setup in the CFD analysis is described in this section. The description of CFD methodology follows the presented procedure for CFD simulations shown in Figure 1.2. This section includes a definition of; computational domain from given geometry, mesh and time step, model and material property, boundary conditions, points of interest, solution and post processing. Finally, a sub section to define all simulation cases and operating conditions.

The CFD simulation setup is based on theories in both technical acoustics and fluid dynamics as well as previous studies by Iqbal and Selamet [17] and Selamet *et al.* [18, 19]. The numerical setup in CFD mimics a real experimental acoustic two-microphone measurement setup including flow for a silencer-duct system. This ensures that the simulation is as relatable to the experimental results as possible. The computational domain is then slightly changed from the given geometry to resemble the experimental setup described in Section 4.2. Flow enters the computational domain through the inlet boundary and terminating boundaries are chosen to inherit non-reflecting properties for the acoustic waves. Acoustic waves are then generated in the computational domain causing a propagation through the silencer-duct system. Probes in the computational domain are defined to capture a varying pressure signal caused by the propagating acoustic waves during the simulation time, acting as virtual microphones. The pressure signals are then extracted from the simulation for post-processing and calculation of TL. Three different inlet velocities are then studied, chosen with respect to the experimental results (v_m = [21, 41, 61] m/s) and compared to the experimental results.

The presented general CFD setup above is then varied by changing different setup parameters to obtain a numerical setup best fit to describe the acoustic performance of a duct-silencer system including flow with high accuracy. The varied parameters include:

- Three different meshing approaches
- A variation of meshing parameters for two of the meshing approaches, meshing study
- Two different turbulence models
- Two different experimental techniques to obtain transmission loss
- Two different microphone positions for one of the measurement setups

After the numerical setup was studied to obtain the optimal simulation methodology, the simulation methodology was used to simulate geometrical changes to the duct in order to change flow behaviour and to improve transmission loss characteristics. Each varied parameter will be described separately in each corresponding section and then combined in the section describing simulation cases and operating conditions.

4.3.1.1 Computational domain

The geometry of the silencer-duct system presented in Chapter 3 was obtained from a CAD model. The CAD model is imported into the pre-processing software ANSA version 16.2.0 where the geometrical surfaces outlining the computational domain are defined. The computational domain is defined from the internal volume of air in the duct system limited by the walls of the duct and silencer as well as the inlet and outlet orifices. The given geometry is simplified by removing the corrugated parts of the duct called bellows. Two bellows are included in the duct system design to make the duct system easier to fit the inside the engine compartment. Flow passing a corrugated pipe is complex and often include large generation of turbulence, making it hard to describe numerically in CFD with high accuracy. The corrugated part is thus removed to reduce possibility of numerical errors in describing the turbulent flow. Assuming that the corrugated parts of the pipe have little effect on the acoustic wave propagation and flow effect on the silencer validates the simplification. The necks are also simplified by removing the slightly expanding part of the neck connected to the resonator housing. Instead of expanding, the necks are now straight in both ends. Since the difference between the straight necks and real expanding necks is small, this simplification results in no or a small difference in acoustic performance between the two geometries.

Further, two extensions of the given duct system are also created in preparation of the computational domain. The inlet and outlet orifices of the duct is extruded normally straight outwards to create a constant diameter inlet and outlet duct section, $D_{in,out} = 0.057$ m. The purpose of this is to mimic the experimental setup in Section 4.2, to let the inlet flow fully develop in the duct before entering duct system where measuring is conducted and to include duct parts with constant diameter, where virtual microphone measurement points can be placed. The length of the inlet and outlet ducts are defined by L_{in} and L_{out}. The computational domain and geometry presented is from now on referred to as the *bent duct geometry* (BD). The bent duct geometry is used for all simulations where the numerical setup is studied and can be seen in Figure 4.2 and 4.3. Figure 4.2 shows an overseeing picture of the full domain including the two extensions where the lower right end is the flow inlet, (a). It also shows a close view of the silencer where the two bellows are removed and replaced by straight ducts (b), see Figure 3.1 for reference geometry. A closer look of the straight necks and the resonator cavities can be seen in Figure 4.3.

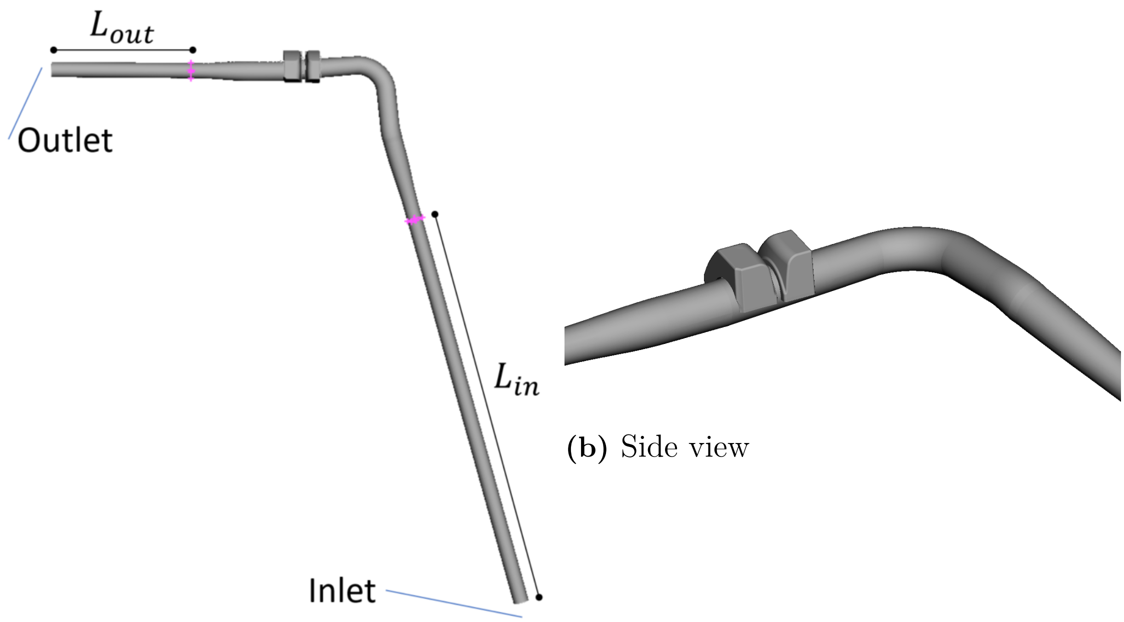

(b) Side view

(a) Top view

Figure 4.2: Computational domain of bent duct geometry, purple points show extension points.

When the optimal numerical CFD setup had been established and geometrical duct changes in order to improve silencer performance were performed, a new computational domain was defined. The new computational domain is referred to as the *straight duct geometry* (SD) and has the same silencer acoustic properties as the bent duct geometry since the silencer geometry defined in Chapter 3 is kept intact. The duct system on the other hand is changed by straightening the ducts

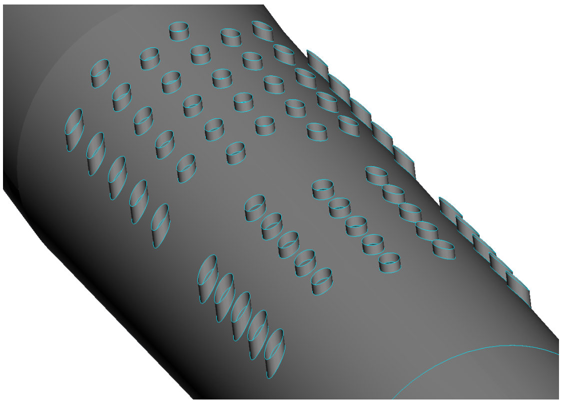

(a) Top view

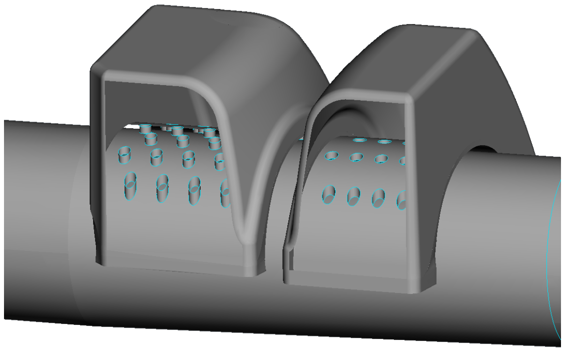

(b) Side view

Figure 4.3: Computational domain of the resonator necks and cavity for the bent duct geometry, where (b) has removed walls to able to see neck details in the geometry.

directly upstream and downstream of the silencer. In the expanded parts of the duct, close to the silencer, the full real duct geometry extending to the inlet and outlet is removed. The inlet and outlet pipes are replaced by extruded ducts of constant diameter with the same diameter as the cut-off point in the expanded part of the real duct geometry. The length of the extruded straight inlet and outlet ducts correspond to the same duct centerline length from the same cut-off point in the bent duct geometry. This keeps the total length between the inlet and outlet of the duct system constant between the bent and straight duct computational domain. Keeping the total length of the two duct system constant, implies that potential standing acoustic wave formations formed by the total duct length remains unaltered between the two computational domains. Since the expanded part of the real geometry duct diameter is slightly expanding when travelling downstream passing the silencer, causes the inlet and outlet straight ducts to have a slightly different diameter: $D_{in} = 0.07$ m and $D_{out} = 0.074$ m. The straight duct geometry is shown in Figure 4.4 and 4.5. The full computational domain is present in Figure 4.4 where the blue lines represent cut-off points. Figure 4.5 shows a closer look on the silencer, where the geometry is equal to the bent duct computational domain.

Figure 4.4: Full computational domain of the straight duct geometry, inlet on the right and flow direction to the left.

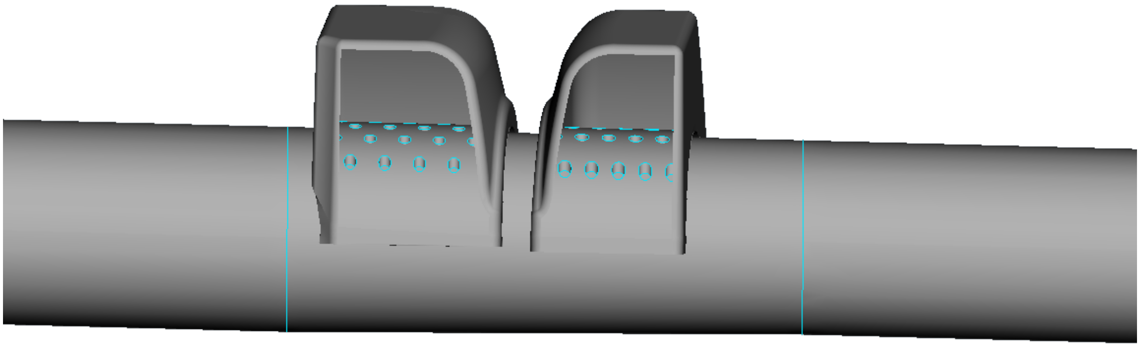

Figure 4.5: Resonator cavity and neck connection of the straight duct computational domain.

4.3.1.2 Mesh and time step

After the computational domain had been defined, a surface mesh made of triangular 2D cells is exported from ANSA with high resolution and imported to Star-CCM+. The surface mesh initially outlines the defined computational domain (walls and orifices) and the 3D volume mesh describing the internal air is calculated in Star-CCM+. Introducing meshing concepts for a 3D wall-bounded mesh: *re-meshed surface mesh*, *prism layer mesh* and *core mesh*.

Re-meshed surface mesh is a re-defined surface mesh of the imported surface mesh where new meshing parameters are defined like: cell-type, cell-size or orientation. The purpose of the re-meshed surface mesh is to describe the spatial resolution of the mesh in tangential direction of the outlining wall, with increased efficiency and control compared to the initial imported surface mesh. The re-meshed surface mesh of the full volume mesh is required for prism layer and core meshes to be initialized and grown from. Prism layer mesh describes the spatial resolution in direct proximity of walls, in the wall-normal direction. The mesh technique controls the cell size closest the wall (in y^+), cell-growth and thickness of the prism layer mesh normal to the wall. By controlling the prism layer parameters, it is possible to control the spatial resolution of the boundary layer flow which is important to consider when choosing different turbulence models and wall-treatment models, see Section 2.1.3 and 2.1.4. The core mesh is the main part of the mesh, where 3D cells grow from the outer part of the prism layer mesh to fill the remaining computational domain. Important parameters of the core mesh that dictate the spatial resolution of the simulation is: cell-type (controlling the whole computational domain or region), minimum/maximum cell-size and cell-growth. The core-mesh in Star-CCM+ is calculated in an unstructured way, where cells are generated automatically to fill the computational domain, growing from interfaces, prism layers or wall-surfaces following the governing meshing parameters. Hence, the first core mesh cell-size is controlled by the size of the cell it grows from. Using an unstructured meshing method is an efficient and flexible way of meshing complex geometries and its geometrical features.

Three different meshing methods were developed to describe the computational domain spatially. The three different meshes are from now on referred to as: *basic mesh* (BM), *intermediate mesh* (IM) and *advanced mesh* (AM). Where the basic mesh is created to describe turbulence models with wall functions (high-Reynolds number wall treatment) and the intermediate and advanced meshes can fully describe turbulent flow down to the wall (low-Reynolds number wall treatment). The basic mesh could be altered to also function with low-Reynolds number wall treatment but would require a high cell count (number of cells in computational domain) and thus increase computational cost. Hence, the main purpose of developing the intermediate and advanced meshing methods was to be able to use turbulence models with a low-Reynolds number wall treatment and still keep the cell count low for increased computational efficiency. The intermediate and advanced meshing methods were also developed to reduce numerical dissipation and increase flow resolution in regions of importance. The mesh cell count of the three different mesh methods resulted in; basic mesh included roughly 4 million cells; intermediate mesh included roughly 7.5 million cells and advanced ended up having roughly 13 million cells.

The main reason behind the resolution requirement of all three meshes was to be able to describe a fully turbulent flow including propagating acoustic waves with low numerical dissipation and high accuracy. Usually, the necessary resolution requirement is often defined by flow characteristics and choice of turbulence models but in this case the requirement is defined by the need to describe acoustic waves with certain wavelengths. This is due to acoustic waves travelling at the speed of sound $c \approx 340$ m/s, substantially larger than the studied mean flow speed of Mach number 0-0.2. A common practise in CFD including acoustic wave propagation is having at least twenty spatial grid points for the shortest wavelength of acoustic waves present in the simulation. In other words, the maximum cell length in the acoustic wave direction for all three meshing methods is smaller than 5 % of the shortest acoustic wavelength (highest frequency), $\Delta x_{max} \leq \lambda_{min}/20$. Since the studied frequency range is chosen to be 500-1750 Hz for all simulations, the maximum mesh cell size for all meshes can be calculated as $\Delta x_{max} \approx$ 9.7e-3 m. By choosing a cell-size smaller than Δx_{max}, the numerical dissipation of the acoustic waves are minimized. The maximum cell-size is thus chosen to be $\Delta x_{max} =$ 8e-3 m. [43]

The *basic mesh* is spatially discretized as one continuous fluid region. Polyhedral cells are chosen as cell-type to describe the whole computational domain since polyhedral cells have good geometrical flexibility and low numerical dissipation. However, polyhedral cells are computationally inefficient due to the high cell-boundary count. Prism layer cells are used on all duct and silencer walls to describe the turbulent boundary layer flow. Since the basic mesh is developed to describe turbulence models with wall functions, the first cell of the prism layer (closest to the wall) is set in the fully turbulent sub-layer, $y^+ > 50$. The prism layer thickness normal to the wall is set in outer parts of the fully turbulent sub-layer $y^+ > 150$, close to being outside the boundary layer flow. However, since y^+ of a cell is directly linked to the local passing flow speed, the first cell and thickness of the prism layer are changed based on the different inlet flow speeds studied. Hence, three basic meshes are created with the same mesh properties except some minor changes to the prism layer mesh. The changes between the three meshes are calculated rigorously to be comparable and only related to a change in inlet flow speed. Cell-transition between prism layer mesh and core mesh is smooth to reduce numerical difficulties. Cell-growth for all cells is kept under 30 % to also reduce numerical problems and dissipation. Cell-resolution is increased in all neck regions of the silencer to have twenty grid points over both the hole diameter and neck length. The neck region mesh resolution is applied by reducing the re-meshed surface cell-size and defining small cylindrical regions for each neck where a constant cell-size is defined. The required cell count in the neck area is studied but initially follows from the studies by Iqbal and Selamet [17]. The basic mesh is shown in Figure 4.6 with pictures of the core duct mesh and the refined neck region mesh presented on a duct centerline plane section.

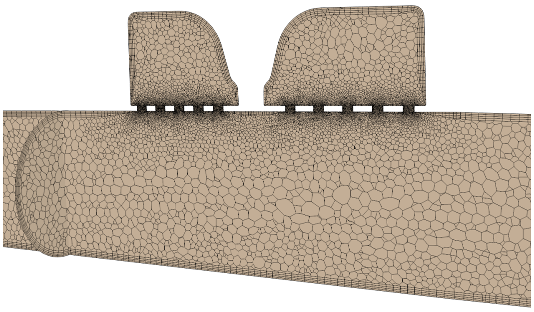

(a) Core duct

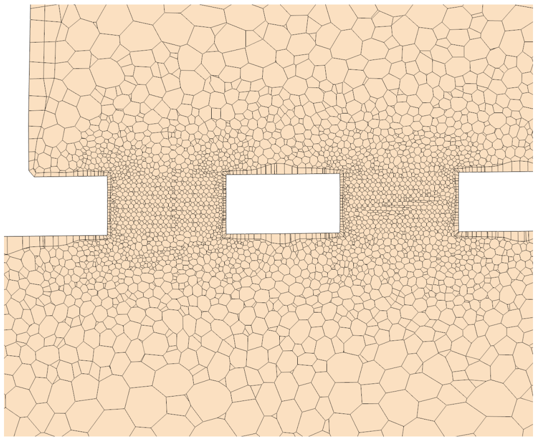

(b) Neck region

Figure 4.6: Overview of the basic mesh methodology generated in Star-CCM+.

The *intermediate mesh* is developed from the basic mesh by changing wall treatment from high-Reynolds number to low-Reynolds number. This is done by increasing the resolution of the boundary layer flow with the prism layer layer. The first prism layer cell is now set in the viscous sub-layer, $y^+ < 1$. The thickness of the prism layer is still set in the outer parts of the fully turbulent sub-layer, $y^+ > 150$. Keeping the cell-growth lower than 30 % requires a large number of prism layer cells to reach the outer turbulent sub-layer compared to the basic mesh. Since y^+ is proportional to the local flow speed, the first cell size normal to all walls is calculated with the highest of the three studied inlet flow speeds. Hence, y^+ will reduce even further below one for the lower inlet flow speeds. There exists no lower limit for y^+ in low-Reynolds wall treatments, thus only one mesh is generated in the intermediate meshing methodology for all three inlet flow speeds. Due to the required increase in prism layer cells and that the flow is wall-bounded increases the total number of cells in the mesh drastically compared to the basic mesh. The computational domain is thus split in three regions; one duct region reaching from the inlet to a cross-section with a distance $L = 0.04$ m upstream of the silencer; one duct region reaching from a cross-section with a distance $L = 0.08$ m downstream of the silencer to the outlet and one geometrical region in-between composed of the duct and silencer. The extruded polyhedral cell-type is efficiently used in the inlet and outlet duct region where an extruded polyhedral cell is defined as a polygon (pentagon or hexagon) extruded in 3D parallel to the duct wall. It is easier to control the extrusion than randomly filled polyhedral cells and thus the total number of cells can be reduced. However, two interfaces are now present in the mesh where extruded polyhedral cells transition to normal polyhedral cells, since polyhedral cells are still used to mesh the silencer due to the flexibility. The transitions between the two cell-types are conformal, meaning that the cells on either side share the same cell-boundary on the interface. The two interfaces are placed sufficiently far away from the silencer to not interfere with propagating acoustic waves in regions of interest. The intermediate mesh methodology is shown in Figure 4.7 with an overview of the core duct mesh, neck region mesh and the interface transition region presented on a duct centerline plane section.

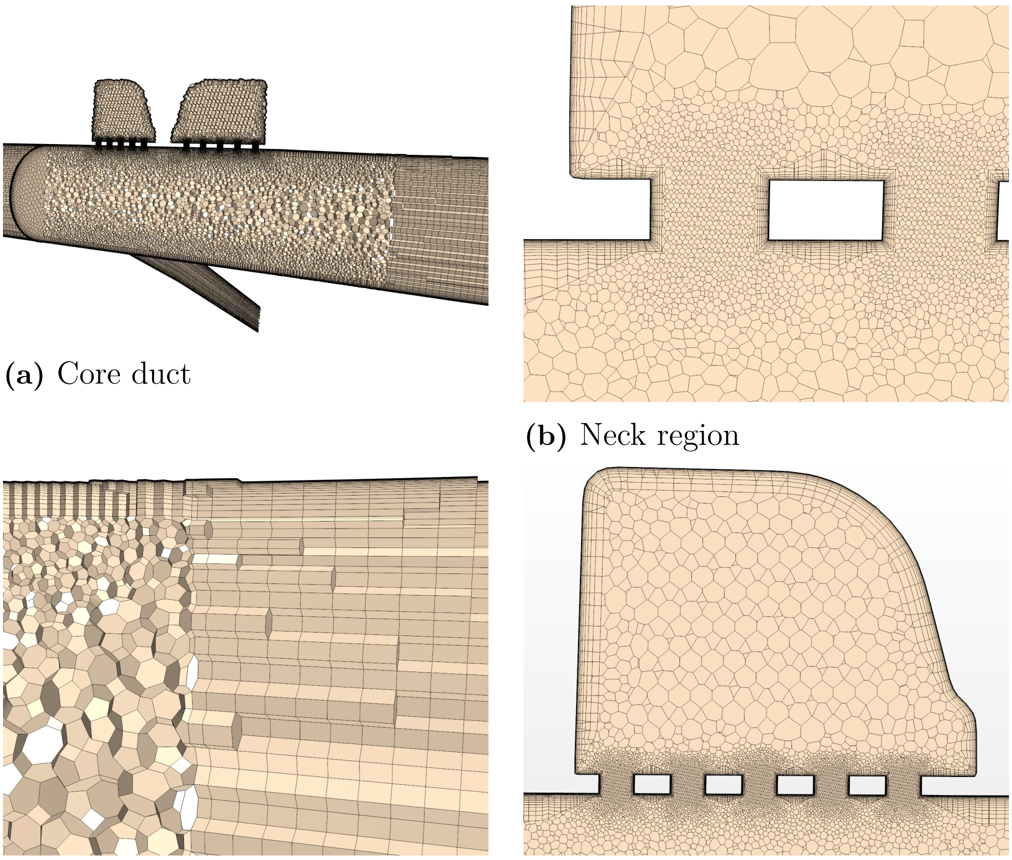

(a) Core duct

(b) Neck region

(c) Transition interface

(d) Resonator house

Figure 4.7: Overview of the intermediate mesh methodology generated in Star-CCM+.

The *advanced mesh* is continuation from the intermediate mesh as it is still generated to function with low-Reynolds number wall treatment and includes the two duct regions with extruded polyhedral cell type. Hence, the previous description of prism layer and core mesh parameters in the intermediate mesh applies to the advanced mesh as well. The aim with the advanced meshing method is to improve the way prism layer cells are generated in the neck region. In Figure 4.6b and 4.7b, the thickness of the prism layer has to be reduced in order for the prism layer to fit inside neck since the neck diameter is smaller than the prism layer thickness. This reduces the number of cells in the prism layer in those regions which is not wanted. Hence, the computational domain of the middle region is also split in three regions: duct, necks and resonator cavities. The interfaces are placed at the ends of the necks while letting the prism layer travel across the interface without retracting inside the holes, see Figure 4.8b. By letting the prism layer align with the flow passing the neck openings as well as reducing the cell-size normal to the neck openings, increases resolution of the grazing shear layer flow. Prism layers are also generated inside each neck as well as the two resonator cavities, separately from the duct mesh. A full overview of the advanced meshing methodology can be observed in Figure 4.8 presented on a duct centerline plane section.

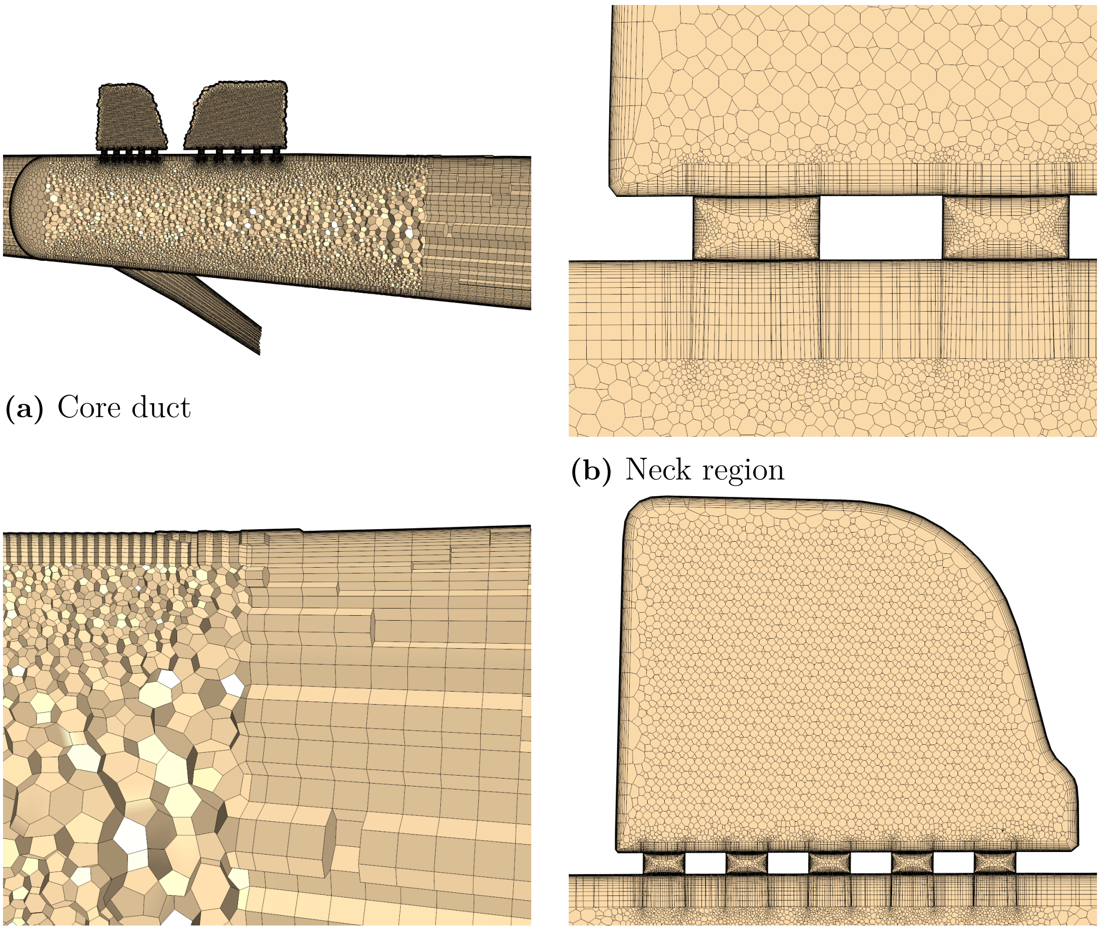

(a) Core duct

(b) Neck region

(c) Interface

(d) Resonator house

Figure 4.8: Overview of the advanced mesh methodology generated in Star-CCM+.

The temporal resolution or time step for all unsteady simulation setups is also chosen according to resolution requirement of propagating acoustic waves. Like the spatial resolution requirement, a common practice in CFD with acoustic waves is representing time marching with at least twenty time steps per shortest time period of acoustic waves present in the simulation. Since the studied frequency range is decided to be 500-1750 Hz, the maximum time step can calculated with $\Delta t_{max} = 1/(20 f_{max}) \approx 2.86\text{e-}5$ s. The time step for all simulations is thus chosen to be $\Delta t = 2\text{e-}5$ s, reducing the margin of error as well increasing convenience for further signal analysis in post-processing. The choice of time step ensures that numerical dissipation is minimized. [43]

A mathematical condition called the Courant–Friedrichs–Lewy (CFL) condition can be introduced for both mean flow and propagating acoustic waves when performing unsteady simulations. The CFL condition is important to fulfill to increase robustness in the simulation as it generally describes how far an infinitely small fluid parcel travels spatially over the grid during one time step. It can be altered to represent how far an acoustic wave travels over the mesh during one time step. Allowing the fluid or acoustic waves to travel over a large amount of cells during one time step can lead to a diverging solution.

$$\mathrm{CFL}_{convective} = \Delta t \sum_{i=1}^{n} \frac{|v_i|}{\Delta x_i} \leq \mathrm{CFL}_{max} \tag{4.7}$$

$$\mathrm{CFL}_{acoustic} = c \Delta t \sum_{i=1}^{n} \frac{1}{\Delta x_i} \leq \mathrm{CFL}_{max} \tag{4.8}$$

Here, $n = 3$ as the mesh is 3D and Δx_i is the local mesh size in all spatial dimensions. The convective and acoustic CFL number correspond to fluid flow and acoustic wave propagation respectively. The value of CFL_{max} is dictated by choice of temporal discretization scheme. It can be observed that as $|v_i| < c$, it is harder to fulfill the acoustic CFL compared to the convective CFL. [44]

4.3.1.3 Model and material property definition

Mathematical models and numerical methods as well as material properties are defined based on the theoretical background in Chapter 2 and Section 4.1. Two URANS turbulence models are studied including the Realizable $k-\varepsilon$ model and the SST $k-\omega$ model. Both models are selected with the all y^+ wall treatment, which blends low- and high-Reynolds number wall treatment depending on the local wall mesh size. When SST $k-\omega$ turbulence model is used in the numerical model, the gamma transition model as well as the quadratic constitutive relation are included. Air in the duct system is modelled as a compressible ideal gas where dynamic viscosity is modelled with Sutherland's law. Specific heat, thermal conductivity and turbulent Prandtl number of air are set as constant.

Numerical methods are selected in order to reduce numerical dissipation and increase accuracy of the solution. Hence, the second order upwind scheme is chosen for all convection terms (flow, energy, turbulence and transition). Diffusion terms are discretized with the central differencing scheme. Since the simulation is describing transient behaviours, the second order fully implicit time discretization scheme is used. Using the fully implicit time scheme does not impose such a strict CFL condition, meaning that CFL_{max} can be in the order of 10^{-1}-10^{1} (compared to explicit time scheme imposing $\mathrm{CFL}_{max} < 1$ strictly). However, keeping CFL low is always something to aim for when solving PDE numerically. The solution algorithm is solved using a segregated flow and energy solver.

4.3.1.4 Boundary conditions

Both the defined bent and straight duct computational domains are composed of three boundaries: inlet, outlet and walls. An overview of the positions of the inlet and outlet boundaries can be seen in Figure 4.2a. Wall boundaries make up most of the computational domain as it is used for all duct and silencer walls. All wall boundaries are selected with no-slip, adiabatic and rigid conditions.

Star-CCM+ offers the choice of one flow boundary which includes a non-reflecting behaviour, the *free stream* boundary. The free stream boundary allows plane acoustic waves to propagate through the flow boundary without reflecting back into the computational domain. It is required for non-reflecting boundaries to be present when using the decomposition method to calculate transmission loss, see Section 2.2.4.1. The free stream boundary is thus selected for both the inlet and outlet boundaries to remove acoustic reflections from both boundaries respectively. The free stream boundary requires five input flow parameters to be specified: Mach number, static pressure, temperature, turbulence intensity and turbulent length scale. Cross-sectional flow profiles of the five input parameters are selected as uniform along the inlet boundary. Hence, the increased inlet duct length is used to allow the flow to fully develop. However, the flow profiles of Mach number, static pressure and temperature are unknown at the outlet before the flow behaviour of the duct system is studied. Therefore, an initial flow simulation is performed for all simulation cases where velocity inlet and pressure outlet boundary conditions are selected. This allows flow profiles of the outlet to be saved for that simulation case and then be used when the simulation case is performed including free stream boundary conditions on inlet and outlet.

By applying a uniform Mach number profile on the inlet boundary, a mean duct flow will develop and travel downstream towards the outlet. The Mach number inlet profile can then be altered to also generate acoustic waves at the inlet in a certain frequency range and amplitude. Therefore, a time dependent fluctuating Mach number term is added on top of the mean Mach number to generate acoustic waves. Introducing total inlet Mach number profile as

$$\mathrm{M}_{in}(t) = \frac{v_m + v_f(t)}{c} \tag{4.9}$$

where v_m is the mean inlet velocity and $v_f(t)$ is time varying acoustic inlet velocity signal representing acoustic waves. The second fluctuating term varies around zero, and the variation in velocity transfers to variations in density, resulting in propagating acoustic waves. Iqbal and Selamet [17] introduced $v_f(t)$ in their inlet velocity boundary condition as a sinus wave with a specified amplitude and discrete frequency. Iqbal and Selamet then ran several simulations with different discrete frequencies to acquire a frequency band for one mean velocity. This is inefficient and too time consuming for the intended large frequency band of 500-1750 Hz with reasonable frequency resolution. Hence, the acoustic velocity $v_f(t)$ for this study is developed from the definition of Iqbal and Selamet to further represent all frequencies in the studied frequency band simultaneously. The acoustic velocity is therefore defined as a sum of sinus waves with discrete frequencies between 500-1750 Hz separated by a frequency step Δf (frequency resolution) and random uniform phase shift. The amplitude of the multi-frequency acoustic wave velocity is defined so the acoustic energy of the generated acoustic waves is in the same order as the generated acoustic waves by a single-frequency signal defined by Iqbal and Selamet. The multi-frequency acoustic velocity $v_f(t)$ now resembles a random noise signal but restricted to the studied frequency band. The mathematical definition of $v_f(t)$ is

$$v_f(t) = \frac{a_{in} a_{emp,1}}{N_f} \sum_{n=1}^{N_f} \sin\left(2\pi[f_n t + \mathcal{U}_n(0,1)]\right) \tag{4.10}$$

where f_n is a vector including N_f discrete frequencies between 500-1750 Hz with a constant frequency step Δf; $\mathcal{U}_n(0,1)$ is a continuously uniform distribution of N_f values between zero and one; a_{in} is the amplitude selected by Iqbal and Selamet in [17] and $a_{emp,1}$ is an empirical constant to increase the amplitude level of the acoustic velocity signal to the same level as a velocity signal generated with one frequency. This is done to ensure that sufficient energy is inserted in the simulation of the propagating acoustic waves, aiming to have acoustic waves in the duct corresponding to a SPL of 80-100 dB. The empirical constant $a_{emp,1}$ is directly related to the number of frequencies N_f studied. To efficiently evaluate the amplitude level of signals including different number of discrete frequencies, an inlet acoustic Mach number level (AML) is calculated as

$$\text{AML} = 20\log_{10}\frac{\text{RMS}[v_f(t)/c]}{M_{ref}} \tag{4.11}$$

where M_{ref} = 1e-7 is the reference acoustic Mach number. The inlet acoustic velocity in Equation (4.10) is inserted in Equation (4.9) to generate the corresponding inlet variations in Mach number.

The full inlet Mach number profile M_{in} is calculated as a time dependant vector in MATLAB with the same time step and time sample size simulated in the CFD simulation; then imported as a numerical table in the CFD setup of Star-CCM+ where values in the table are interpolated to the corresponding time step in the simulation. But, since the inlet velocity table is calculated with the respective time step used in the CFD simulation, interpolation is exact. The parameters used to define the inlet acoustic velocity can be seen in Table 4.1. The generated time varying inlet Mach number profile for $v_m = 61$ m/s with different number of frequencies and use of $a_{emp,1}$ is shown in Figure 4.9. The blue dashed line is a Mach number signal generated by inserting one frequency and setting $a_{emp,1} = 1$ in Equation (4.10). The red line corresponds to a Mach number signal generated with the full frequency band ($N_f = 251$) without amplification, setting $a_{emp,1} = 1$. The amplitude variation of the red line is lower than the blue dashed line due to the need of dividing the sum of sinus functions by the number of frequencies N_f in Equation (4.10). The black marked line corresponds to the final Mach number signal generated with the full frequency band ($N_f = 251$) including amplification, setting $a_{emp,1} = 15.858$. Calculating the AML value for the blue dashed line and the black marked line yields similar values. The black and red line correspond to the same frequency band but is different due to two different randomized phase shifts.

Variables	a_{in}	$a_{emp,1}$	Δf [Hz]	N_f
Values	0.01	15.858	5	251

Table 4.1: Numerical parameters selected for the inlet acoustic velocity boundary condition.

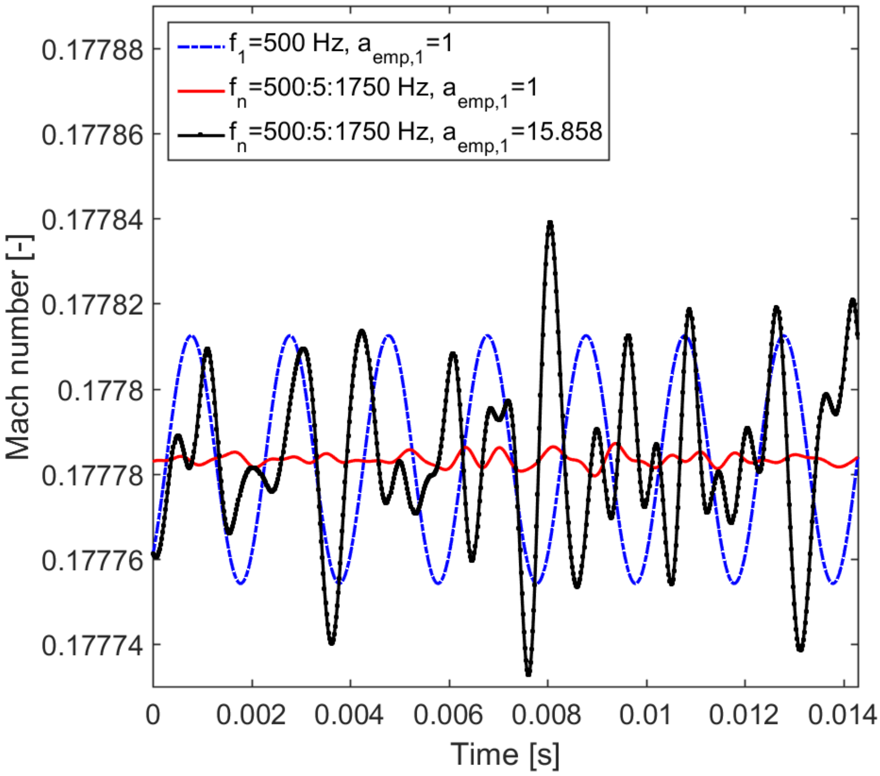

Figure 4.9: Time varying inlet Mach number signals for $v_m = 61$ m/s generated in MATLAB. Blue dashed line corresponds to a single frequency (from Iqbal and Selamet [17]), red line represents 251 frequencies without amplification from $a_{emp,1}$ and black marked line corresponds to 251 frequencies amplified by $a_{emp,1}$.

By allowing the total Mach number profile to define fluid mean flow and acoustic wave generation together with the free stream boundary condition on both inlet and outlet, the numerical setup is replicating the flow and acoustics of an experimental setup using the decomposition method, see Section 2.2.4.1.

Establishing the numerical environment for the two-source method (reference to Section 2.2.4.2), where flow is introduced at the inlet and acoustic waves can be generated both at the inlet and outlet, requires special attention. Generating acoustic waves at the inlet has already been established so generating acoustic waves at the outlet must be defined. Similarly as in the decomposition method, the acoustic waves could be generated from the outlet surface by capturing the Mach number profile and then adding the fluctuating acoustic term. However, this method is neglected due to the complicated nature of handling spatially and temporally varying tables (but is definitively possible). Another approach of acoustic wave generation is to introduce acoustic waves through a volumetric time varying mass source with zero-net mass flux in the computational domain, see Equation (2.1) in Section 2.1. The mass source utilizes the defined inlet Mach number table imported from MATLAB and applies the time varying acoustic velocity values to a specified volume. The source is evenly spread out over the specified volume to disregard any sudden steps in the computational domain, since the source term is zero outside the specified volume. A function can be defined that represents the time varying acoustic source term S_f as

$$S_f(x', t) = a_{emp,2}\delta_{vol}(x')v_f(t) \tag{4.12}$$

where $\delta_{vol}(x')$ defines where in the computational domain the source term is applied. The variable x' is a local coordinate normally directed inwards from either the inlet or outlet boundary surface describing the 3D duct with a 1D variable. The source term is varying in the x'-direction but is radially and tangentially constant (to create plane acoustic waves perpendicular to the duct), hence the source term is continuously equal over planes normal to the inlet or outlet bounded by the duct walls for arbitrary x'. The variable $a_{emp,2}$ is an empirical constant, defined by studying the amplitude of the generated acoustic waves. It is selected such that the power of the generated acoustic waves are in the same order as the acoustic waves generated in the decomposition method. $\delta_{vol}(x')$ can be written such that the source is bounded by a specified cylindrical volume in the computational domain as

$$\delta_{vol}(x') = \begin{cases} f(x') & \text{for} \quad x' \in [L_{S,min}, L_{S,max}] \\ 0 & \text{else} \end{cases} \tag{4.13}$$

and

$$f(x') = \cos^2(\frac{\pi}{\Delta L_S}(x' - \frac{L_{S,min} + L_{S,max}}{2})), \quad \Delta L_S = L_{S,max} - L_{S,min}. \tag{4.14}$$

Here, $L_{S,min}$ and $L_{S,max}$ are the lower and upper limits of the spatial source region in the x'-coordinate and $f(x')$ corresponds to volumetric dispersion of the mass source ($f(x')$ yields a value of 1 in $x' = \frac{L_{S,min}+L_{S,max}}{2}$ and 0 when $x' = L_{S,min}$ or $x' = L_{S,max}$). The mass source is then placed a distance from the boundary to not interfere with the boundary condition. The mass source approach can now be used to introduce acoustic waves in two separate numerical setups: one configuration where the mass source is placed close to the inlet and one configuration where the mass source is located close to the outlet. Figure 4.10 shows the two numerical configurations where the mass source is placed close to the inlet in (a) and close to the outlet (b).

(a) Inlet source on duct surface

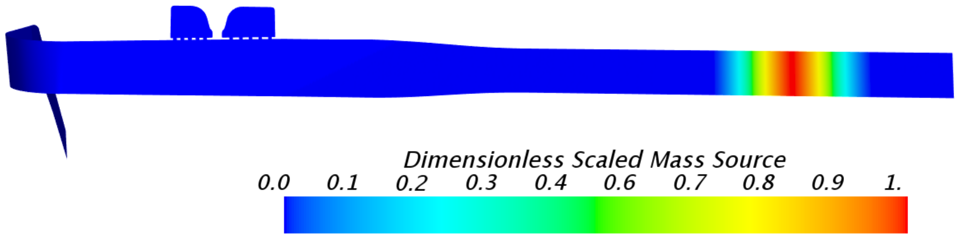

(b) Outlet source on centred plane

Figure 4.10: Schematic picture of the location and distribution of mass source in the computational domain for the two configurations, see Section 2.2.4.2.

The selected parameters for the mass source approach are presented in Table 4.2.

Variables	$a_{emp,2}$	$L_{S,min}$ [m]	$L_{S,max}$ [m]
Values	70	0.1	0.3

Table 4.2: Numerical parameters selected for the mass source approach.

In the mass source approach, free stream boundary conditions are still used at the outlet and inlet boundaries.

4.3.1.5 Points of interest in computational domain

To capture the time varying pressure of the propagating acoustic waves during the simulation time, probes are placed in the domain to function as virtual microphones. The probes measure the time varying pressure during the simulation time at specific points in space upstream and downstream of the silencer. Placing two or more microphones both upstream and downstream to capture the acoustic pressure at the respective microphones is based on theory of the two-microphone method, see Section 2.2.3. The theoretical description regarding microphone spacing s including the highest mean flow speed for the two-microphone method yields the conditions

$$\begin{aligned} f_{min} &= 500 \text{ Hz} \;\rightarrow\; 0.04 < s < 0.226 \text{ [m]}, \\ f_{max} &= 1750 \text{ Hz} \;\rightarrow\; 0.012 < s < 0.064 \text{ [m]}. \end{aligned} \tag{4.15}$$

The lowest frequency implies the lower limit of microphone space while the highest frequency implies the higher limit, leading to $0.04 < s < 0.064$ [m].

Two different sets of probes are defined in the computational domain for the bent duct geometry: *distant microphones* (DM) and *close microphones* (CM). The distant microphones are composed of eight probes in total, four upstream and four downstream. Moreover, the probes are positioned in the extruded inlet and outlet ducts of the computational domain to ensure that the duct diameter is constant with equal spacing between the probes and in the center of the duct section. The probes on the inlet side are placed sufficiently far downstream to allow the flow from the inlet to fully develop. The location of each probe in the distant microphone set can be seen in Table 4.3. The distant microphone spacing is chosen as $s_d = 0.05$ m. It can be seen by using formulas presented in Section 2.2.3, that the distant microphones can capture acoustic frequencies between approximately 400 Hz and 2250 Hz.

	Upstream (Inlet)				Downstream (Outlet)			
Microphone name	p_{d1}	p_{d2}	p_{d3}	p_{d4}	p_{d5}	p_{d6}	p_{d7}	p_{d8}
Distance from boundary [m]	1.15	1.2	1.25	1.3	0.3	0.25	0.2	0.15

Table 4.3: Definition of distant microphone (DM) locations in relation to their respective boundary.

The second set of probes are the close microphones, located in close proximity of the silencer both upstream and downstream. Four probes are included in the close microphone set, two on either side of the silencer. They are placed in a region where the duct is slightly changing diameter but it is assumed that the duct diameter is constant. The close microphones are placed on a centerline through the duct based on a position upstream of the silencer with equal microphone spacing $s_c = 0.04$ m and symmetrically placed in relation to the silencer. The close microphone spacing can capture acoustic frequencies in the frequency band of 500 Hz to 2820 Hz, based on formulas in Section 2.2.3. The locations of the four close microphones are presented in Table 4.4 and a schematic picture of the two probe sets in relation to the bent duct computational domain is shown in Figure 4.11.

	Upstream		Downstream	
Microphone	p_{c1}	p_{c2}	p_{c3}	p_{c4}
Distance from silencer central neck [m]	0.05	0.01	0.01	0.05

Table 4.4: Definition of close microphone (CM) locations in relation to the silencer.

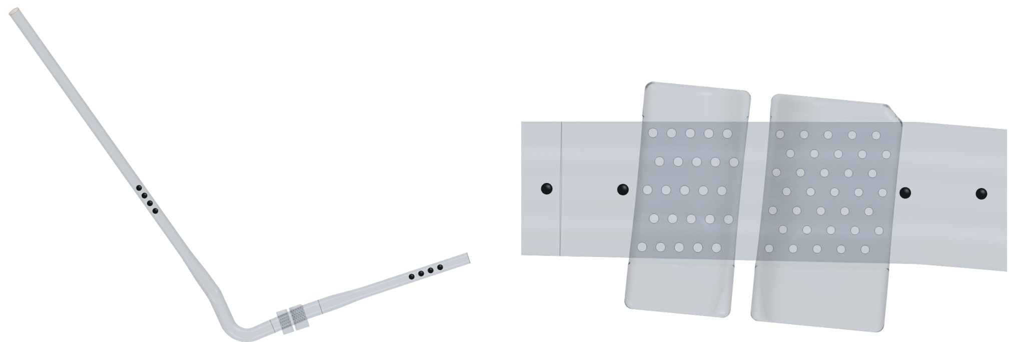

(a) Distant microphones

(b) Close microphones

Figure 4.11: Schematic picture of the location of the two probe sets in the bent duct computational domain.

The close microphone approach is used for the straight duct computational domain directly since the duct on both the upstream and downstream has constant diameter. The microphones are positioned in the center of the duct cross-section. The microphone positions for the straight duct geometry are presented in Table 4.5

	Upstream		Downstream	
Microphone	p_1	p_2	p_3	p_4
Distance from silencer central neck [m]	0.08	0.04	0.04	0.08

Table 4.5: Definition of microphone locations in relation to the silencer of the straight duct geometry.

4.3.1.6 Solution

As described in Section 4.3.1.4, prescribing the free stream boundary condition on the outlet requires previous simulation data. It is also more time efficient to run an initial steady simulation, allowing it to fully converge and then simulating an unsteady solution compared to simulating an unsteady solution from start, see Section 4.1.5. Hence, the solution procedure can be separated in three steps.

- Solution step 1: Steady simulation with velocity inlet and pressure outlet boundary conditions, including mean flow
- Solution step 2: Steady simulation with free stream boundary condition on inlet and outlet, including mean flow
- Solution step 3: Unsteady simulation with free stream boundary condition on inlet and outlet, including mean flow and propagating acoustic waves

Solution step 1 is run until all initial pressure fluctuations are removed from the solution by observing the pressure drop. The pressure drop convergence coincides with the calculated flow residuals convergence. Flow profiles on the outlet boundary surface are then saved to be used in Solution step 2. Now in step 2, the inlet and outlet boundary conditions are replaced with free stream boundary conditions using data from solution step 1 to define the outlet. Solution step 2 is then allowed to converge in the same way as step 1. When the solution has fully converged, the temporal behaviour is changed from steady to unsteady, defining the time step and temporal discretization scheme as well as changing the inlet Mach number profile to include acoustic wave generation. The solution is then allowed to run until a sufficiently large sample space N_s of acoustic pressure signals have been captured at the microphone locations. The sample space size is governed by the post-processing methods but generally the solution were run until $t_{end} =$ 0.3 s.

4.3.1.7 Post-processing

When a sufficiently large sample space of discrete acoustic pressure points had been sampled at the virtual microphones, the flow behaviour and acoustic pressure signals were analyzed. Flow behaviour were studied directly in Star-CCM+ through its post-processing visualization tools. The sample space of the acoustic pressure signals were tabulated and exported for post-processing in MATLAB. Since the pressure signal is calculated in the time domain and studying transmission loss characteristic is performed in the frequency domain, the pressure signals are converted to the frequency domain with Fourier transform. In the frequency domain the pressure signals can be analyzed in terms of energy content in each discrete frequency, rather than of time. Fourier transform converts a time dependant signal to a frequency dependant signal (and back again through inversion) as

$$\begin{aligned} \mathcal{F}[g(t)] = \hat{g}(f) &= \int_{-\infty}^{\infty} g(t) e^{-i2\pi f t} dt, \\ \mathcal{F}^{-1}[\hat{g}(f)] = g(t) &= \int_{-\infty}^{\infty} \hat{g}(f) e^{i2\pi f t} df, \end{aligned} \tag{4.16}$$

where $\hat{g}(f)$ is the Fourier transform of an arbitrary signal $g(t)$. Since the sample space of acoustic pressure values is discretely spaced by a time step Δt, the signal is discretely spaced in frequency by Δf and the size of the space is finite, it is not possible to utilize the continuous definition of Fourier transform presented in

Equation (4.16). The discrete-time Fourier transform (DTFT) is therefore used and defined as

$$\hat{h}_{1/T_s}(f) = \sum_{n=-\infty}^{\infty} T_s \cdot h(nT_s) e^{-2\pi f T_s n} \tag{4.17}$$

where $\hat{h}_{1/T_s}(f)$ is the discrete-time Fourier transform of any discrete time-dependant function $h(t)$, sampled at a time interval T_s [s] ($f_s = 1/T_s$ [samples/s] is the sample-rate). In MATLAB, the fast Fourier transform (FFT) algorithm is used to calculate the DTFT of the acoustic pressures signals. With FFT, discrete frequencies f_d are evaluated based on a correlation

$$f_d = \frac{d}{N_s T_s}, \; d = 1, 2, 3, ... \tag{4.18}$$

where d is an integer called the discrete frequency number or bucket number. Setting $d = 1$ yields the evaluated discrete frequency step of the FFT. Since the studied acoustic pressure signal includes discrete frequencies of multiplies of the frequency step Δf and the time interval T_s of the sample space is the chosen time step Δt. The sample space N_s must be chosen such that the discrete frequencies f_d of the FFT represent the studied frequency band. The ratio between the frequency step of the simulation Δf and discrete frequency f_d must be an integer n,

$$\frac{\Delta f}{f_d} = n. \tag{4.19}$$

It was seen from studying different sample spaces sizes N_s that it was sufficient to use the smallest sample space necessary, $n = 1 \;\; \rightarrow \;\; f_d = \Delta f$, to obtain DTFT of acoustic pressure signals with high quality. The sample space size can therefore be calculated with Equation (4.18) setting $d = 1$ and $f_d = \Delta f$.

$$N_s = \frac{1}{\Delta f \Delta t} = 10^4 \tag{4.20}$$

If N_s is chosen in such a way that Equation (4.18) calculates discrete frequencies f_d that in turn yields non-integer values of Equation (4.19), spectral leakage occurs. The simulation time required to obtain $N_s = 10^4$ samples of the acoustic pressure signals is thus at least $t_{end} \geq N_s \Delta t = 0.2$ s. With $N_s = 10^4$ samples and FFT in MATLAB, the Fourier transform of the acoustic pressure signals at different microphone locations can be calculated in order to obtain TL, see Section 2.2.4.

4.3.1.8 Simulation cases and Operating conditions

An overview of all simulation cases performed with different numerical setups as well as selected material properties for the domain and boundary conditions is presented in this section. For all simulations performed, the material properties and flow boundary condition for temperature, gauge pressure, turbulence intensity and turbulent length scale are the same. The definitions of material properties and boundary conditions can be seen in Table 4.6. Choosing turbulence intensity and turbulent length scale follow the studies by Iqbal and Selamet [17] and Selamet *et al.* [19].

Description	**Symbol**	**Value**
Specific heat	C_p	1003.62 J/(KgK)
Turbulent Prandtl number	σ_θ	0.9
Thermal conductivity	κ	0.0260405 W/(mK)
Temperature of inlet and outlet air	T_{in}, T_{out}	293 K
Gauge pressure of inlet and outlet air	p_{in}, p_{out}	0 Pa
Atmospheric pressure of air	p_{atm}	101325 Pa
Turbulence intensity	I_t	0.05 (5 %)
Turbulent length scale	L_t	$0.05 D_{in,out} = 0.0025$ m

Table 4.6: Definition of material properties and flow boundary conditions

The bent duct geometry was initially studied to compare results of different numerical setups and methods with experimental results. All simulation cases performed with the bent duct geometry are presented in Table 4.7. Boxes with "S" corresponds to a performed simulation. The decomposition method, SST $k-\omega$, IM and AM simulations with 61 m/s inlet velocity are performed four times respectively with different meshing parameters. Since the two-source method is performed with AM, the best mesh from the meshing study of AM is used.

Bent duct geometry (BD)					
TL method	**Turbulence model**	**Mesh**	**Inlet mean velocity v_m [m/s]**		
			21	41	61
Decomp.	$k-\varepsilon$	BM	S	S	S
		IM	-	-	-
		AM	-	-	-
	SST $k-\omega$	BM	S	S	S
		IM	-	-	Sx4
		AM	S	S	Sx4
Two-source	SST $k-\omega$	AM	-	-	Sx2

Table 4.7: Simulated cases for the bent duct geometry, "S" stands for performed simulation.

After the best numerical setup had been established, the straight duct geometry was studied in order to find ways to improve the acoustic performance of the silencer in relation to flow. Only inlet mean velocity equal to 41 m/s is studied to increase variation in geometrical changes instead of studying different velocities. All simulations performed with the straight duct computational domain including different geometrical changes are presented in Table 4.8.

Straight duct geometry (SD)	
Geometrical configuration name	**Inlet mean velocity v_m [m/s]**
	41
SD (Reference)	Sx2
SD + Ridge x1	S
SD + Ridge x2	S
SD + Stamp	S
SD + Stamp Half	S
SD + Stamp Rectangular Half	S
SD + Stamp Full	S

Table 4.8: Simulated cases for the straight duct geometry including names for geometrical configurations.

4.3.2 Acoustic CAE

A brief overview of the numerical setup used to calculate the acoustic performance of the studied silencer-duct system using acoustic CAE is presented in this section. The acoustic CAE software used is Actran version 16.0. Actran solves the linearized wave equation numerically using finite element method, where the governing equations are presented in Section 2.2.1.

The bent duct computational domain presented in Section 4.3.1.1 is used as the acoustic computational domain. The small simplifications that has been done on the bent duct computational domain in comparison to the real geometry does not influence the acoustic properties of the duct-silencer. The bent duct computational domain is therefore a good approximation of the real geometry when using acoustic CAE. A 3D volume mesh must be created in order to describe the linearized wave equation in the computational domain through spatial discretization. The volume mesh is created in ANSA from the computational domain. Mesh restrictions when calculating acoustic CAE are much less strict in comparison to CFD meshes. The volume mesh is created with tetrahedral cells, where the cell-size is defined as; duct cell-size equals 5 mm; resonator cavity cell-size equals 3 mm and resonator neck cell-size equals 1 mm. There are no prism layers and cell-growth is only needed in cell region transitions, since cell-size is uniform in the corresponding regions. The total number of tetrahedral cells resulted in 550 000 cells for the acoustic CAE mesh. Figure 4.12 shows pictures of the mesh used in the simulation with acoustic CAE. The mesh is then exported from ANSA and imported to Actran for simulation.

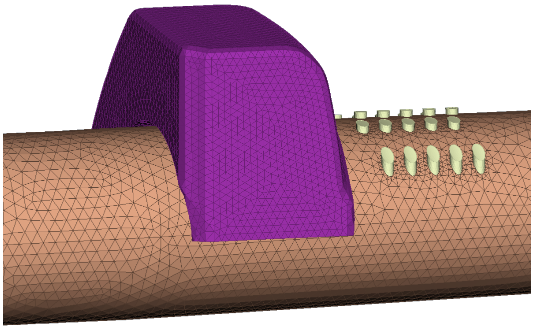

(a) Overview (without first resonator cavity)

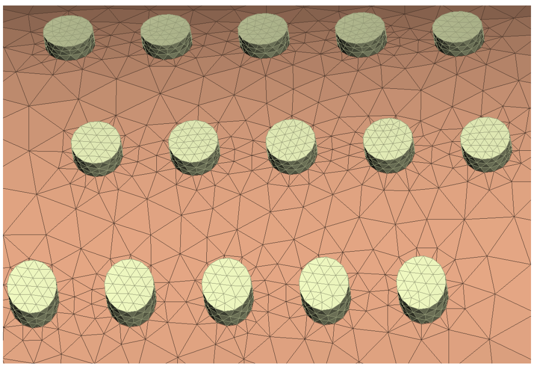

(b) Zoom on resonator necks

Figure 4.12: Schematic pictures of the mesh used in the acoustic CAE simulation.

In Actran, the silencer-duct system is studied using the direct frequency response analysis where the same frequency band of 500-1750 Hz with frequency resolution of 5 Hz as in the CFD setup is selected. The acoustic CAE simulates acoustic wave propagation in the frequency domain without consideration for mean flow effects. However, acoustic CAE in Actran still accounts for material properties and acoustic dissipation effects from the propagation medium and duct friction losses. The propagating medium is therefore selected as air with standard atmospheric material properties. However, the speed of sound is altered by adding 0.5 % complex dampening, $c = 340 + 1.7i$ m/s. The dampening on speed of sound accounts for acoustic dissipation effects and is usually chosen between 0.5-1 %. The inlet boundary inserts a propagating acoustic wave mode in the first order and at the same time allows reflected waves to be transmitted through the boundary. The outlet boundary also allows first order acoustic wave modes to transmit through the boundary, fulfilling the anechoic terminations. The simulation is calculated using the PARDISO-solver. The 3D spatial frequency response function of the simulated computational domain is calculated and post-processed to obtain the transmission loss characteristics.

5

Results and discussion

Results and discussion related to the different methodologies described in Chapter 4 are presented in this chapter. The results are divided in four respective parts: experimental results, results from acoustic CAE, CFD results with the bent duct geometry and geometrical changes studied using CFD with the straight duct geometry.

5.1 Experimental results

This section aims to present the experimental results of transmission loss characteristics of the studied intake air duct system with attached silencer, see section 4.2 for reference of methodology. The experimental study is performed at the Marcurs Wallenberg Laboratory for Sound and Vibration Research at the Royal Institute of Technology (KTH), separately from this Master's thesis project. Therefore, the results from the experimental study is regarded as a reference to the numerical study performed with CFD in this Master's thesis.

The experimental results include four different flow speeds: 0 m/s, 21 m/s, 41 m/s and 61 m/s. In Figure 5.1, the transmission loss characteristics of the silencer-duct system for the four studied mean inlet flow velocities are shown. Since it could be calculated theoretically that the two Helmholtz resonators included in the silencer have eigenfrequencies close to each other around 750-800 Hz, it can be seen in Figure 5.1 that the two resonators are working together to create one transmission loss peak around 830 Hz (without flow). If the two resonators would have been separated by a larger eigenfrequency difference, the two resonators would have been working independently of each other, creating two transmission loss peaks representing each resonator eigenfrequency. The second transmission loss resonance characteristic at around 1200-1300 Hz composed of two smaller peaks is created by higher order resonances due to resonator cavity design and location related to the duct. The resonance peaks will be named in the remaining chapter as: *peak 1*, *peak 2* and *peak 3*, where naming is shown in Figure 5.1. When mean flow is introduced in the duct system, the transmission loss characteristic is changed. The transmission loss remains almost unchanged for the lowest flow speed of 21 m/s, only a slight peak reduction can be seen for peak 1. Increasing the flow speed from 21 m/s to 41 m/s and 61 m/s increases the eigenfrequency of peak 1 from 835 HZ to 900 Hz and 950 Hz and reduces the peak amplitude from 45 dB to 35 dB and 21 dB. Peak 2 and 3 shifts slightly in eigenfrequency but increases in amplitude for inlet flow speed of 41 m/s. For 61 m/s, peak 2 and 3 merge into a single peak while shifting in peak frequency to 1320 Hz and reduces the peak amplitude to 21 dB. It is also possible to observe an increase in signal noise (non-smooth) for the higher flow speed conditions compared to the lower speed conditions. This is due to an increase in flow generated noise in the duct system disturbing the capturing of acoustic pressure at the experimental microphones.

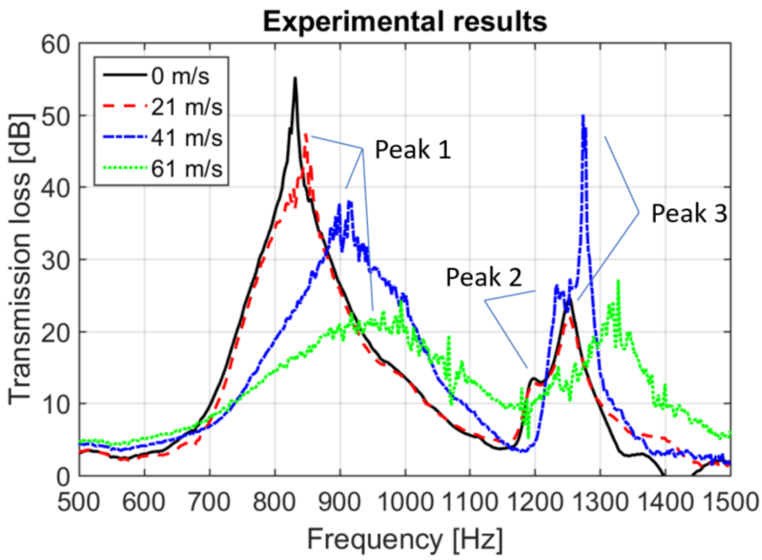

Figure 5.1: Experimental transmission loss results of duct-silencer system with different inlet mean velocities obtained at the Marcurs Wallenberg Laboratory for Sound and Vibration Research at the Royal Institute of Technology (KTH), see Section 4.2.

5.2 Acoustic CAE

This section presents the transmission loss result from the acoustic CAE simulation. Since the acoustic CAE simulates the acoustic properties of the duct-silencer system in the frequency domain without influence of mean flow, the results are compared to the experimental results with no-flow condition. The results of the acoustic CAE and comparison with experimental results can be observed in Figure 5.2. The result from acoustic CAE is comparable to the experimental results, with a slight difference in eigenfrequency where the acoustic CAE underestimates the frequency. By comparing the acoustic CAE in Figure 5.2 with the experimental results of transmission loss including duct mean flow in Figure 5.1, it is possible to see that acoustic CAE is not able to predict the behaviour of the duct-silencer system with high flow speeds.

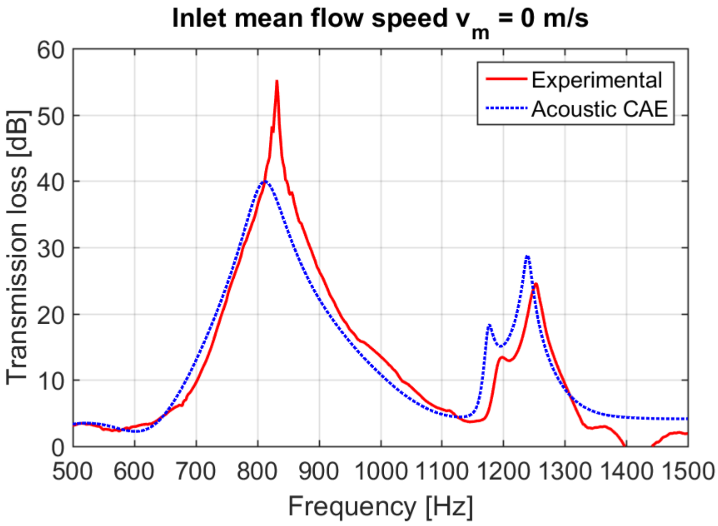

Figure 5.2: Transmission loss results of duct-silencer system obtained with acoustic CAE in Actran compared to experimental results of no-flow condition.

5.3 CFD - Bent duct geometry

In the following section, the CFD results obtained in Star-CCM+ of the bent duct computational domain are presented. The results are mainly focused on comparisons between different numerical setups and options in order to find the best CFD methodology to describe the flow and propagating acoustics of the computational domain. Five sub sections divide the results in: flow behaviour, mesh comparison, microphone positions, two-source method and finally a comparison between two turbulence models.

5.3.1 Flow behaviour

An overview of the mean duct flow behaviour is shown in Figure 5.3. The figure includes duct fluid streamlines coloured by the magnitude of a dimensionless velocity, scaled with the inlet mean flow speed. In this case, the mean inlet flow speed is 61 m/s. It can be observed that the flow is no longer uniform, a turbulent velocity profile where the highest flow speed is present in the center of the duct and reducing towards the walls has developed in the straight inlet duct, lower right corner of Figure 5.3. The flow speed is then reduced when it travels through the expanding part of the duct, creating zones of low velocity. A large duct vortex in the flow is created when the fluid passes the duct bend, changing from parallel duct flow to rotating duct flow. Defining a uniform outlet flow profile would therefore hinder the flow from developing naturally in the duct system since the flow vorticity reaches the outlet. Allowing a velocity inlet and pressure outlet simulation to converge in order to capture the flow profile on the outlet boundary is needed. When the flow travels through the contracting part of the pipe, the flow is again accelerated before leaving the computational domain through the outlet. Since the flow is turbulent and rotating when it passes the silencer, a closer look on the vortex and how the flow behaves in the silencer follows.

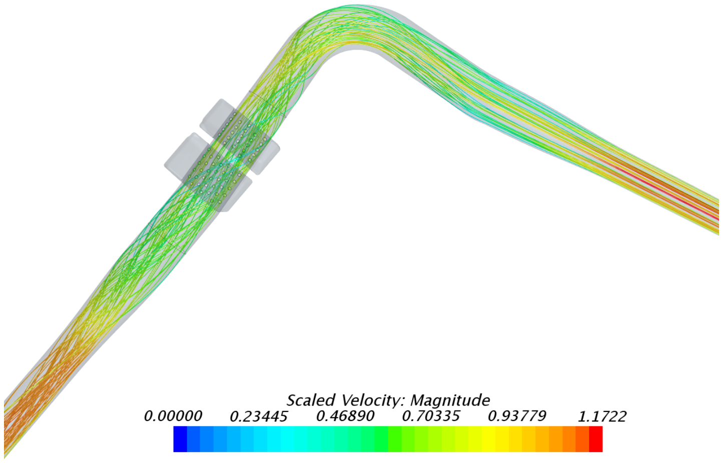

Figure 5.3: Duct fluid streamlines coloured by the magnitude of a dimensionless velocity, scaled by the inlet mean flow speed of 61 m/s.

In Figure 5.4, the flow velocity vectors are extracted and plotted on a cross-sectional surface before the silencer and after the bend. The vectors are again coloured by the dimensionless scaled velocity in the same simulation of mean flow inlet speed of 61 m/s. The beige circle which can be seen through the walls is the outlet, the flow direction is thus inwards. By studying Figure 5.4, it can be seen that the bend accelerates the fluid travelling in the outer parts of the bend while the fluid speed is diminished taking the short route of the inner corner. According to the right-hand rule of rotating bodies, the rotation is right-handed since the flow is travelling towards the outlet. Since all necks are parallel with the center row of necks, the outer-most row of neck on the left side (looking towards the outlet) are now aligned with the rotating flow travelling upwards in the duct. The rotating flow therefore governs the flow behaviour inside the resonator necks and cavities heavily.

A Cartesian coordinate system is created where one principle axis is aligned with the neck direction. The scaled flow velocity can thus be plotted at the neck interface to the duct, in the direction parallel to the necks. Positive direction is set as towards the resonator cavity, going inside the resonator. Figure 5.5 shows scaled flow velocity in the "Mid_Cyl_Hole" coordinate system where "[j]" is parallel to the resonator necks. The "Mid_Cyl_Hole[j]" coordinate system will be re-used further down in this chapter. It can be seen that the flow going inside the resonator cavity is strongest in necks aligned with the rotating duct flow travelling upwards. Almost all flow going inside the resonator cavity is present in this neck row, while the rest of the necks have flow going back to the duct. The strongest outflow is present in the row of necks aligned with the rotating duct flow travelling downwards, in the bottom row in Figure 5.5 or right-most row in Figure 5.4. Therefore, the flow inside the resonator house is part of the rotating duct flow, creating a complex flow interaction between duct, necks and resonator cavity.

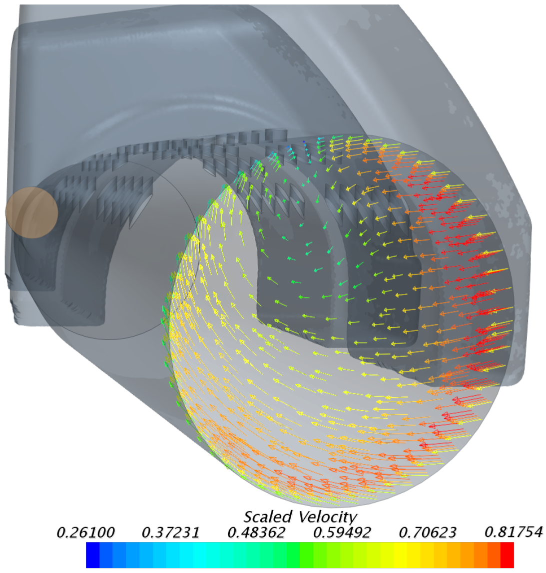

Figure 5.4: Flow velocity vectors coloured by dimensionless scaled velocity (inlet mean flow speed equals 61 m/s), plotted on a cross-sectional plane post duct bend and before silencer.

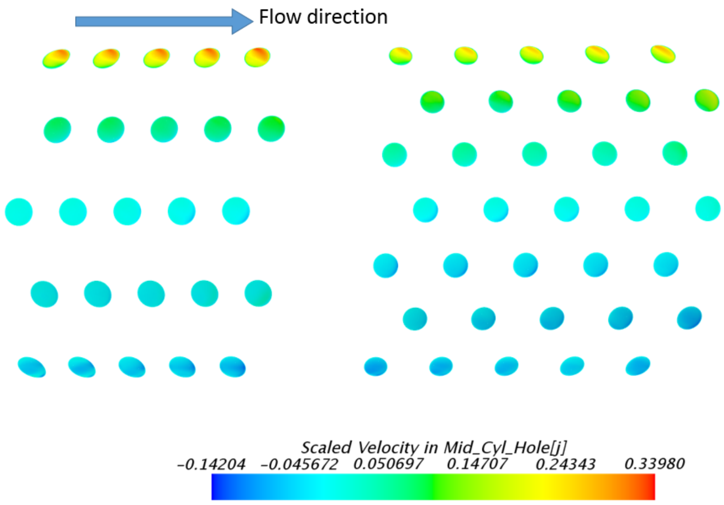

Figure 5.5: Dimensionless scaled velocity in the direction of the neck extrusions contour plotted on the neck orifice surface, positive direction towards the resonator cavity.

The flow behaviour passing in close proximity of the walls can be observed by plotting the friction velocity on the wall surface since the flow velocity is zero at the wall, see section 2.1.4 for definition. In Figure 5.6, the friction velocity is contour plotted on the duct surface region related to the silencer. From the figure, it can be seen that the grazing flow passing the neck opening is angled at an incline corresponding to the rotating duct flow. The hole pattern is misaligned with the inclined rotating flow. It can also be seen that the fluid traveling close to the inner part of the bend with lower velocity is affecting the flow far downstream. Streaks of low friction velocity can be seen downstream of holes where flow is injected into the duct from the resonator. In these small regions, it is most likely that the injected air forces the duct fluid to move around the jet, reducing wall grazing flow speed directly downstream of the hole.

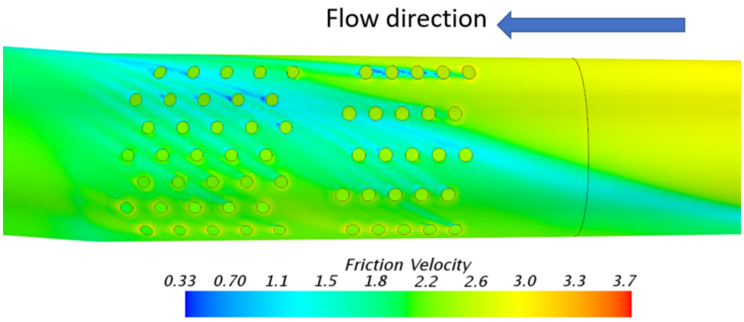

Figure 5.6: Friction velocity plotted on the duct wall surface in close proximity to the silencer.

All figures presented in this section is obtained with 61 m/s inlet mean flow speed and the same numerical setup including the $k - \varepsilon$ turbulence model. The mean flow behaviour in the duct for the bent duct geometry does not differ much between different numerical setups. Since no experimental data was obtained or provided on duct flow behaviour, it is thus hard to deduce which numerical setup best describes the duct flow behaviour. A closer look in how different numerical setups affect the acoustic properties simulated with CFD follows.

5.3.2 Meshing comparison

The first numerical parameter studied was the mesh methodology and its internal geometrical parameters. This section will present the results of both flow and acoustics from the three different mesh methodologies introduced in Section 4.3.1.2. Since both the intermediate mesh (IM) and advanced mesh (AM) are studied more in-depth with different cell sizes in regions of interest, the best mesh from these internal mesh studies respectively will be presented in this section. The BM is used in conjunction with the $k - \varepsilon$ turbulence model while IM and AM are used with SST $k - \omega$ turbulence model.

Since the basic mesh (BM) is generated in order to utilize high-Reynolds number wall treatment (wall functions) while IM and AM can resolve the full turbulent boundary layer without wall functions, it is interesting to see the resulting non-dimensional wall normal distance y^+. Figure 5.7 shows contour plots of y^+ for both types of wall treatments in a wall duct surface region close to the silencer. Figure 5.7a shows y^+ for the basic mesh where it can be seen that most of the duct region has $y^+ > 40$ in the expanded parts of the duct. Hence, the smaller duct diameter in the inlet and outlet pipes have even larger y^+ due to increased flow speed. Thus, the y^+-condition for wall functions of setting the first cell height of the mesh in the fully turbulent sub-layer is mostly fulfilled. However, in regions directly surrounding the necks it can be seen that y^+ is reducing down under $y^+ < 5$. This is due to prism layer mesh reducing in height to fit inside the necks, thus the first cell height has to reduce and exist in the buffer sub-layer of $5 < y^+ < 30$ which is not optimal. In the low flow speed region following the bend, it can be seen that y^+ is also calculated to be in the buffer sub-layer. One of the main reasons of developing a mesh functioning without wall function was to remove the uncertainty of having wall normal cell-heights located in the buffer sub-layer. The all y^+ treatment is selected along the choice of turbulence model, simulating flow using the basic mesh will use a blend of high- and low-Reynolds wall treatment around the holes. In Figure 5.7b, it can be observed that $y^+ < 1$ in the expanded duct region and around the holes fulfilling the requirement of using low-Reynolds number wall treatments. The figure is captured with the highest inlet flow speed of 61 m/s, causing lower inlet flow speeds to have an overall lower value of y^+ in the silencer-duct system continuing to fulfill the requirement. In the following three Figures 5.8-5.10, the magnitude

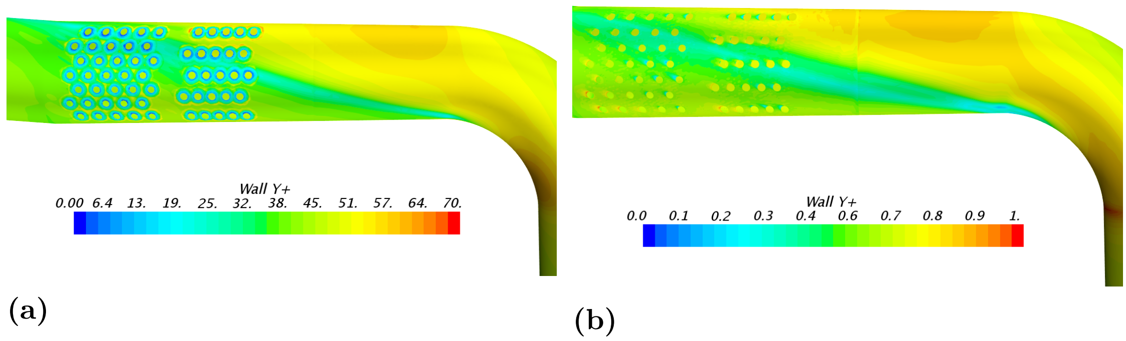

Figure 5.7: Non-dimensional wall normal distance y^+ plotted on the duct surface of the silencer region, (a) shows y^+ for BM with high-Reynolds number wall treatment and (b) corresponds to a low-Reynolds number wall treatment used in IM and AM.

of dimensionless velocity is contour plotted on a plane cutting the centerline of the middle-row of necks for all three mesh methodologies with inlet flow speed 61 m/s. It can therefore be observed how the flow is resolved in the neck region including: duct boundary layer flow, grazing shear flow and flow behaviour going inside the resonator cavity with the three different meshing approaches. Starting by looking at the boundary layer flow in the duct of all three figures. It can be seen that the boundary layer flow in Figure 5.8 is not resolved smoothly around the necks with wall functions, due to the retracting prism layer cell-size. It is possible to see how the first cell-size in relation to the duct wall is changing as it governs the height of the calculated boundary layer flow with wall functions. However, this behaviour is not present in Figure 5.9 and 5.10 where the boundary layer flow is smoothly calculated down to the wall with no numerical problems. It is therefore most likely that the IM and AM is resolving the boundary layer flow in close proximity of the neck openings with higher accuracy than BM does.

Looking at the shear layer generated by the low-speed fluid in the neck and the grazing duct flow in three figures, a large difference between the three meshes can be seen. In Figure 5.8 and 5.9 where the prism layer suddenly turns to enter the neck and resonator cavity for BM and IM, the shear layer flow is diffusely smeared due to the cells being misaligned with the flow direction and not sufficiently fine in the perpendicular direction of the flow (direction of the neck). In Figure 5.10 on the other hand, the created interface in the neck-duct opening where the prism layer is allowed to continue over the neck increases the shear layer flow resolution. A sharp edge between the flow inside the neck and grazing flow is present in Figure 5.10, where the shear layer thickens further downstream in the neck opening until the trailing edge.

All three figures show the same flow behaviour where the grazing flow hits the trailing edge, splits and then a portion of the flow enters the neck and resonator cavity. A strong behaviour of this can be seen in Figure 5.5 where the largest in-flow speed occurs close to the trailing edge of the left-most (upper) row of necks. In the center-row of necks, this behaviour is not as prominent as the mass-flow inside the necks is lower. However, a large difference can be seen by comparing the results of the three meshing methodologies. The magnitude of the flow velocity is increased greatly for the flow entering the resonator cavity in the simulations with IM and AM compared to BM. There are many factors that differ between the three different meshes and thus the difference in flow behaviour is hard to pin-point. The increase in resolution of the turbulent boundary layer flow as well as a small fundamental change in vorticity of the rotating flow is most likely the cause of the increased center-row neck inflow. By changing turbulence model from $k-\varepsilon$ in BM to SST $k-\omega$ in IM and AM could affect the calculation of vorticity in the duct and thus resulting in the neck region difference. A finer mesh resolution inside the resonator cavity of AM compared to IM could possibly increase flow inside the necks, explaining the difference between IM and AM where both setups use the SST $k-\omega$ turbulence model. However, without any experimental data or results from CFD with higher accuracy turbulence models (LES or DNS), leads to conclusions regarding which mesh methodology best describes the flow behaviour in the neck regions to be hard to make. But, since the main objective of this study is to describe the acoustic performance of the silencer-duct system including flow and not the flow behaviour specifically, it is possible to compare the acoustic performance of the silencer-duct system with the three different meshes in relation to their flow behaviour.

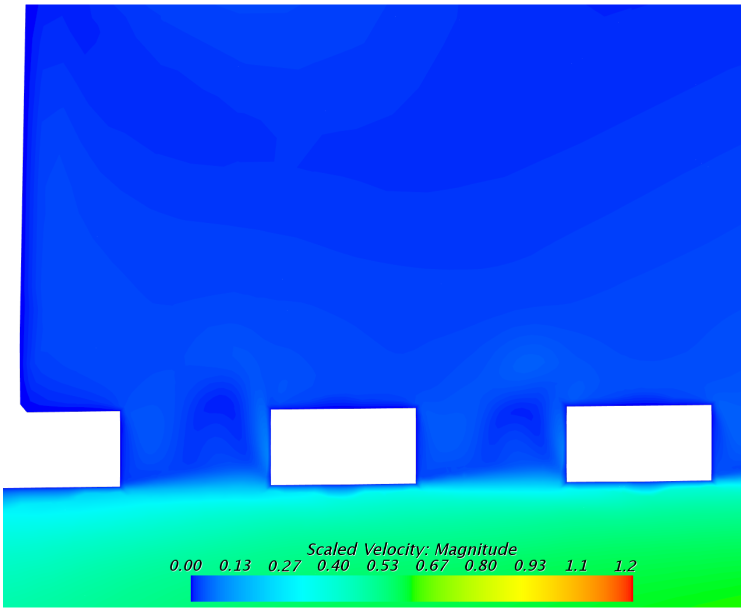

Figure 5.8: Magnitude of dimensionless velocity scaled with inlet mean flow speed of 61 m/s plotted on a plane cutting the center-row of necks zoomed in at the first two necks, using the **basic mesh** and $k-\varepsilon$ turbulence model where flow direction is to the right.

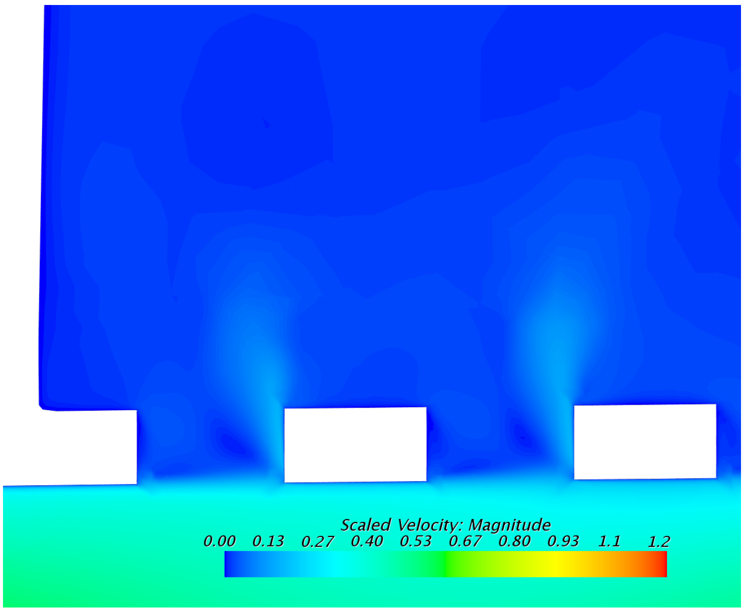

Figure 5.9: Magnitude of dimensionless velocity scaled with inlet mean flow speed of 61 m/s plotted on a plane cutting the center-row of necks zoomed in at the first two necks, using the **intermediate mesh** and SST $k-\omega$ turbulence model where flow direction is to the right.

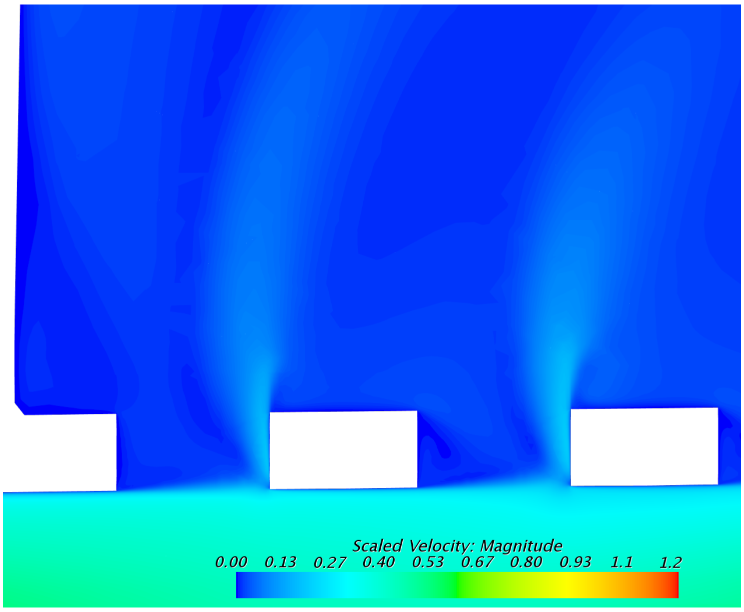

Figure 5.10: Magnitude of dimensionless velocity scaled with inlet mean flow speed of 61 m/s plotted on a plane cutting the center-row of necks zoomed in at the first two necks, using the **advanced mesh** and SST $k-\omega$ turbulence model where flow direction is to the right.

A comparison between transmission loss obtained experimentally and with the three different meshes for inlet mean flow speed equal to 61 m/s, using the decomposition method and the distant microphones (3,4 and 5,6) is presented in Figure 5.11. Generally, all three numerical setups and meshing methods of the CFD results are able to capture the characteristic first and second transmission loss peaks in comparable amplitude to the experimental data. However, all three setups lack the ability to fully describe the shift of eigenfrequency caused by the grazing duct mean flow for the first- and higher-order modes. The first peak eigenfrequency of the three meshing methods are in the region of 865-890 Hz compared to the experimental peak value of 950 Hz. It can also be observed that all three transmission loss curves inherit a periodic wave formation in the first peak, where three local minimums can be seen at frequencies 650, 800, 950 [Hz]. This wave formation is also present for the two lower inlet flow speeds of 21 and 41 m/s, which can be seen in Appendix A.1. Since the wave formation is absent in the experimental data and generally absent when studying transmission loss of Helmholtz resonators, the current calculation of transmission loss needs further studying and the wave formation is addressed in the following section.

Disregarding the wave formation, it can be observed that the basic mesh using the $k-\varepsilon$ turbulence model performs better in describing the acoustic properties of the silencer-duct system than IM or AM with SST $k-\omega$ turbulence model. This is also the case for the lower inlet flow speeds. The eigenfrequency of the first peak is captured using BM with higher accuracy than using IM or AM. A larger difference can be seen in difference of the second higher-order resonance, where the results with BM has higher amplitude and increases accuracy of the resonance frequency compared to the results from IM or AM in relation to the experimental results. Since there exists many different parameter differences between the three meshes it is hard to deduce the reason why BM outperforms IM and AM. The differences between the meshes in the first transmission loss peak are small, where the results of IM and AM are almost equal. Common parameters in numerical setup using IM and AM that differ from the numerical setup of BM is: wall treatment, turbulence model and separating the duct in three regions with two cell-type transitions. The amplitude reduction is governed by flow in the necks and frequency shift is governed by strength of the shear layer in the neck-duct orifice. It is therefore possible that the low-Reynolds number wall treatment in addition of using different turbulence models causes a slight difference in the neck orifice shear layer flow, thus altering the resulting acoustic propagating waves in comparison to the results from the BM simulation. A change of cell-type in duct due to the region separation could affect the propagating acoustic waves negatively but is not likely since no numerical errors or problematic regions were found in close proximity of the two interfaces where the duct region is separated. By studying different cell-sizes in the resonator cavity and how it affects TL, it was found that the cell-transition between prism layer cells on walls and volume cells governs the accuracy of the higher-order modes (the second peak exists due to resonances in the resonator cavity). Smooth transitions and sufficiently small cells increases accuracy of capturing the second transmission loss peak. It is thus most likely that the difference in TL of the second peak between the three meshing methods is a question of mesh quality inside the resonator cavity. The differences in core cell-size in the resonator cavity of IM and AM compared to BM (Figure 4.6, 4.7 and 4.8) is large where IM and AM have quite abrupt cell transitions between neck-cavity and wall-cavity.

It can however be concluded that using low-Reynolds number wall treatment does not necessarily correspond to an increase in accuracy of capturing flow effects on acoustic properties of the silencer-duct system. Since BM is more computationally efficient than both IM and AM including a slight increase in accuracy, BM is chosen as the best and most efficient mesh.

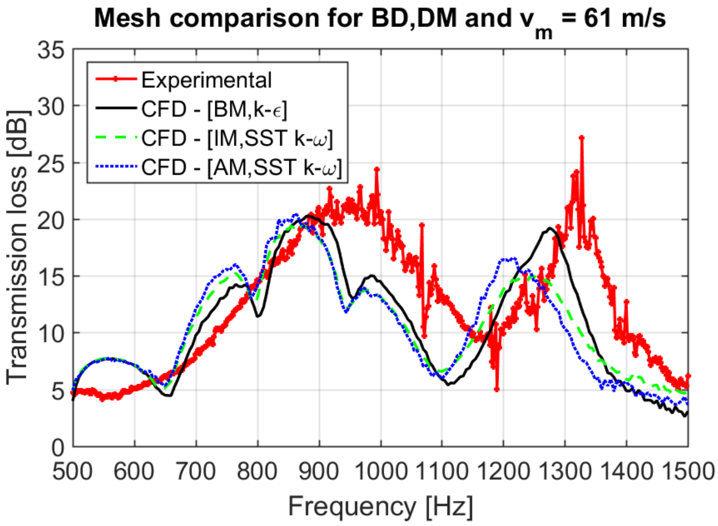

Figure 5.11: A comparison between transmission loss from the experimental study and CFD simulations of the bent duct geometry with the three different meshing methodologies and inlet flow speed 61 m/s, calculated using the decomposition method and the distant microphones.

5.3.3 Microphone positions

The formation of standing waves in the transmission loss curves presented in Figure 5.11 was unexpected and requires further attention. Since the formation appears to be periodic in its appearance in the transmission loss curve, it is most likely to be caused by some unwanted geometrical resonance. Using the decomposition method, two pressure signals are needed on both the upstream and downstream side to obtain transmission loss based on the two-microphone method. Four distant microphones were inserted on both the upstream and downstream side in the computational domain. Hence, three sets of two microphones on both sides can be formed for calculating TL. By studying different pairs of microphones on both the upstream and downstream side when calculating TL, it was found that the wave formation remained unchanged by choosing different pairs on the downstream side. However, by choosing another microphone pair on the upstream side the wave formation was significantly altered. In Figure 5.12a, the simulation setup with BM, $k-\varepsilon$ and 61 m/s inlet flow speed is shown where TL has been calculated with both microphone pairs 1,2 & 5,6 as well as 3,4 & 5,6.

It is previously known that a Helmholtz resonator induces an acoustic impedance in a duct system where it is used. The impedance causes propagating acoustic waves to be reflected by the resonator back towards the source of the sound waves. If the inlet boundary condition is assumed to be non-reflecting, the inlet duct region from inlet to silencer can be seen as a duct system with one infinitely long duct end (inlet) and one end corresponding to a change in impedance at the silencer location, where the impedance of the silencer causes acoustic waves to be reflected back towards and transmitted through the inlet boundary. Wave superpositions between incident and reflected sound waves are thus found in the duct, resulting in phase-cancellation/amplification. Acoustic waves in moving fluids are also subject to convective effects where acoustic waves moving in the same direction as the flow have increased wavelength (stretch) and waves moving the opposite direction as the flow have decreased wavelength (contract) compared to moving in stagnant fluid. One possible explanation to the wave formation seen in Figure 5.12a is that incident stretched waves interact with reflected contracted waves through phase-cancellation/amplification. The phenomena is therefore both governed by the chosen mean flow speed and microphone position in relation to the silencer. Further research is needed to understand the wave formation completely.

Due to the wave superpositions at the distant microphone positions, a new set of microphones were placed closer to the silencer. The comparison between using distant and close microphones can been observed in Figure 5.12b. The simulation result is the same as in Figure 5.12a. It can be seen that reducing the length between silencer and microphones on the upstream side removes the wave superpositions and a smooth transmission loss curve can be obtained. However, reflections from the silencer are also present at the close microphone location and thus influences the calculation of TL. Therefore, to validate that the close microphone location yields transmission loss result with sufficient accuracy and low influence of reflected acoustic waves the two-source method is used to calculate TL.

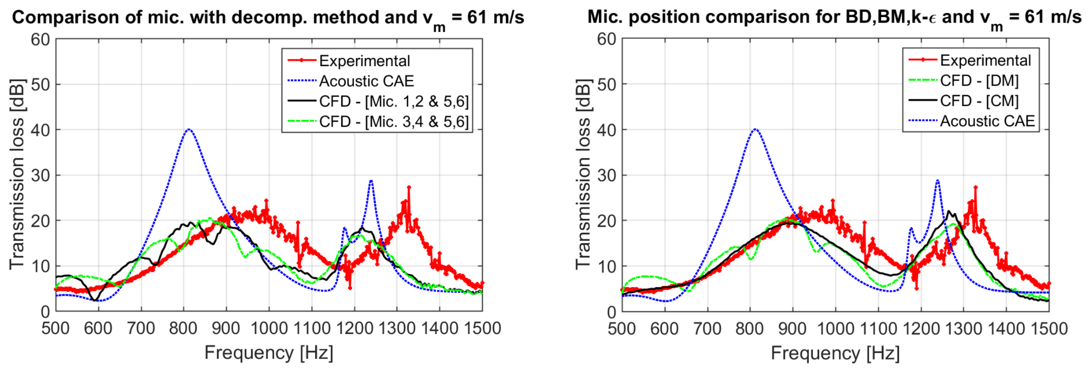

(a) **(b)**

Figure 5.12: Transmission loss calculated with different microphone pairs upstream of the silencer, (a) shows the change in wave formation by changing microphone pairs for the distant microphones and (b) presents the difference in TL when using the distant and close microphones.

5.3.4 Two-source method

The two-source method removes the strict requirement of acoustic wave reflections in the duct system. Hence, the two-source method removes the influence of microphone location on transmission loss calculation which is seen to be problematic using the decomposition method. However, transmission loss is in theory both affected by duct expansion and Helmholtz resonator resonances, both present in the silencer-duct system. Depending on the chosen location of microphones, the duct expansion can be included or excluded. Measuring pressure signals in the inlet and outlet ducts include the influence of the duct expansion on TL while measuring with the close microphones only calculates the TL characteristic of the silencer since the microphones are positioned in the expansion already. Transmission loss results calculated using the two-source method with two different inlet microphone pairs are presented in Figure 5.13a. A comparison between the two-source method and decomposition method using the close microphone is showed in Figure 5.13b. The two-source simulations are performed with AM, SST $k-\omega$ turbulence model and inlet mean duct speed of 61 m/s.

Figure 5.13a shows how the transmission loss characteristic using the two-source method is independent of chosen distant microphone pair. The wave formation seen in the TL curves correspond to the duct expansion and using the close microphones removes this wave formation since the two-port is calculated over the silencer only, see Appendix A.2. Hence, the calculation of TL is more accurate using the two-source method than using the decomposition method. Comparing TL calculated using the decomposition method with close microphones and two-source method using the distant microphones in Figure 5.13b, reveals that the calculation of TL using decomposition method with close microphones is still possibly under the influence of reflections on the upstream side. The general TL characteristics as eigenfrequency and frequency shift of the two peaks are captured with both numerical methods. However, the decomposition method using close microphones slightly overestimates TL compared to the two-source method. The decomposition method is also incapable of capturing the TL characteristic of the duct expansion when using the distant microphones, see Figure 5.12a. The two-source method requires twice the computational resources compared to decomposition method and TL calculated using decomposition method with CM yields results similar to the two-source method. Decomposition method is therefore used with CM due to its efficiency in the remaining presentations of TL. If computational resources are not a problem, the two-source method is recommended as choice of TL calculation method for its increased accuracy and reduction of parameters eventually influencing the results.

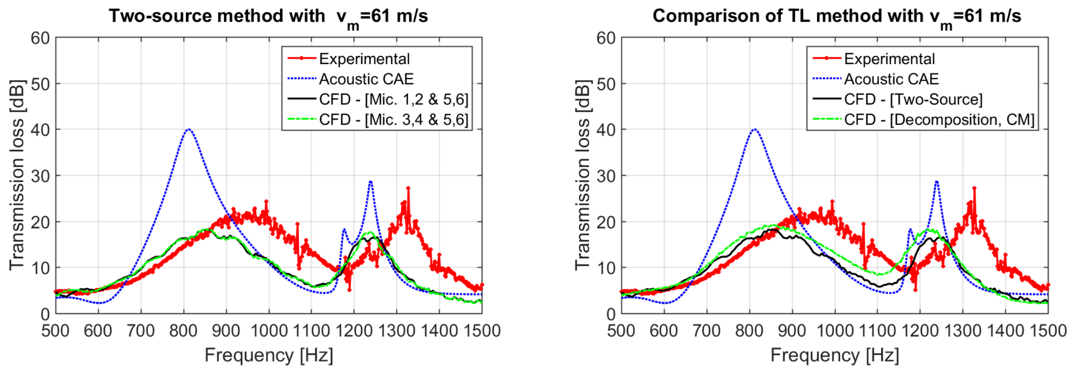

(a) **(b)**

Figure 5.13: Transmission loss results calculated using the two-source method, (a) presents TL using two-source method with two different upstream distant microphone pairs, (b) shows the difference in TL using the two-source method (distant microphones) and decomposition method (close microphones).

5.3.5 Turbulence model

Since there were many parameters influencing the comparison of different mesh methodology results in Section 5.3.2. The basic mesh is studied using both the $k-\varepsilon$ and SST $k-\omega$ turbulence models. SST $k-\omega$ is usually used with low-Reynolds number wall treatment but has been adapted to work with wall functions in Star-CCM+, due to the all y^+ wall treatment. This section therefore presents a comparison between TL for all inlet flow speeds with both $k-\varepsilon$ and SST $k-\omega$ turbulence models. Studying different turbulence models is performed using the decomposition method with close microphones and is the last numerical option studied. This section therefore finalizes the choice of numerical setup prior to using the optimal numerical setup for the following acoustic performance enhancing study.

Starting from the flow behaviour in the neck regions, Figure 5.14 shows the magnitude of dimensionless velocity scaled with the inlet flow speed of 61 m/s using the basic mesh and the SST $k-\omega$ turbulence model, similarly shown as in the meshing comparison Section 5.3.2. It can be observed that the boundary layer flow in the duct and shear layer flow in the neck orifices are calculated similarly as in Figure 5.8 with $k-\varepsilon$ and BM. However, the jets of flow entering the resonator cavity is resembling the simulation results from IM and AM in Figure 5.9 and 5.10. It is therefore most likely that the difference in jet flow behaviour entering the resonator cavity in the center-row of necks between BM and IM or AM is governed by the choice of turbulence model.

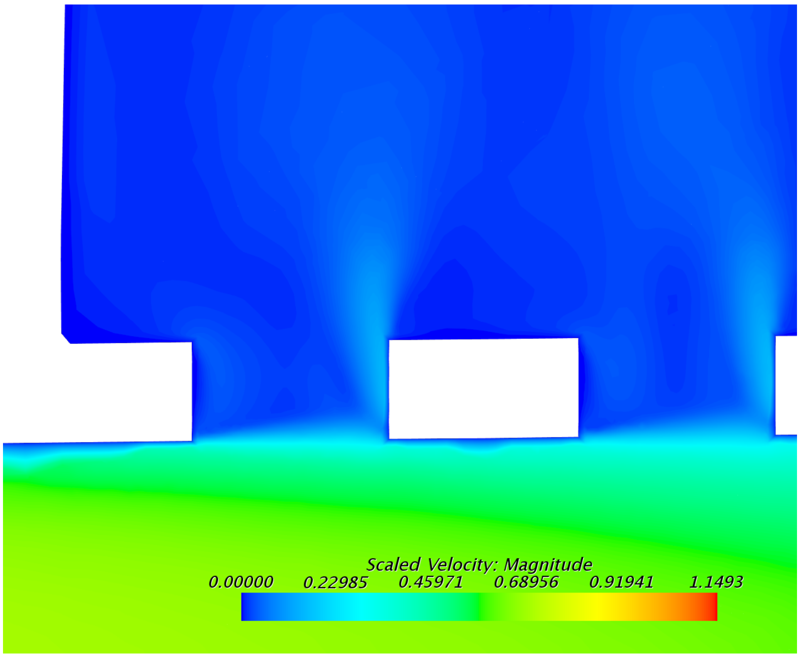

Figure 5.14: Magnitude of dimensionless velocity scaled with inlet mean flow speed of 61 m/s plotted on a plane cutting the center-row of necks zoomed in at the first two necks, using the **basic mesh** and SST $k-\omega$ turbulence model where flow direction is to the right.

Further, transmission loss results from simulations with $k-\varepsilon$ and SST $k-\omega$ turbulence models for all three inlet mean flow speeds of 21, 41 and 61 [m/s] using the basic mesh and decomposition method with close microphones are presented in Figure 5.15. The CFD results from both turbulence models and all inlet flow speeds are compared to experimental results and simulation data from acoustic CAE. Studying the TL results of all inlet flow speeds, it can be observed that the choice of turbulent model does not affect the transmission loss results to such a large extent. There are some slight differences between the two models, for example resonance peak 1 for 21 m/s where $k-\varepsilon$ have a considerably broader peak than SST $k-\omega$. Further, comparing the resulting differences in TL from changing turbulence models with TL comparisons from other studies of numerical options, it can be seen that the other numerical options (like mesh quality and TL calculation method including microphone position) have larger impact on the resulting TL characteristic.

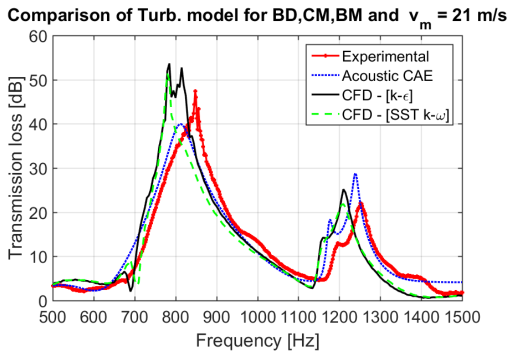

(a) 21 m/s

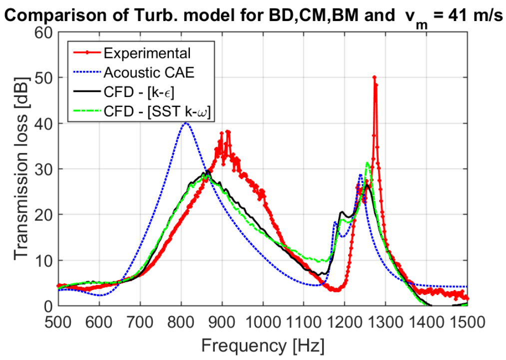

(b) 41 m/s

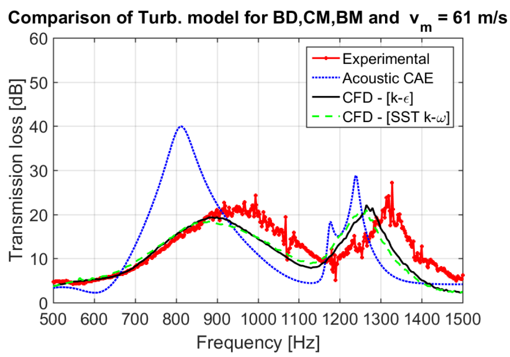

(c) 61 m/s

Figure 5.15: Transmission loss calculated using the basic mesh; both the $k-\varepsilon$ and SST $k-\omega$ turbulence models; decomposition method with close microphones and compared to both experimental and acoustic CAE results, (a,b,c) shows the three different inlet flow speeds respectively.

Generally, it can be seen that calculation of TL captures the trends of the experimental data with good accuracy. The basic mesh using decomposition method with close microphones describes the flow effect on transmission loss for the silencer-duct system with a slight difference in both frequency shift and amplitude compared to the experimental data. In Table 5.1 and 5.2, a summary of both eigenfrequency shift and captured transmission loss reduction from Figure 5.15 is presented. Table 5.1 presents a percentage difference in eigenfrequency shift for each resonance peak of simulations with $k-\varepsilon$ and SST $k-\omega$; compared to experimental data for each respective inlet flow speed, non-dimensionally scaled with the lowest frequency in the domain, 500 Hz. A mean value is then taken for all eigenfrequency differences for each turbulence model respectively to compare the mean eigenfrequency shift accuracy. It can be observed that $k-\varepsilon$ is slightly better than SST $k-\omega$, but not large enough to conclusively state that $k-\varepsilon$ outperforms SST $k-\omega$ model in describing acoustic wave propagation in CFD simulation.

In Table 5.2, the same type of percentage comparison between simulations with $k-\varepsilon$ and SST $k-\omega$, and experimental data is conducted for the peak transmission loss. The peak transmission loss is non-dimensionally scaled with the transmission loss amplitude of the first resonance peak for each inlet flow speed and simulated turbulence model respectively. It can be seen that the differences in transmission loss for inlet flow speed of 41 m/s are much greater than the other flow speeds. Looking instead on Figure 5.15b, it can be seen that the experimental data of resonance peak one inherits some noise and that the simulation is not able to capture the sharp higher-order peaks. Since resonance peak one is more important than the higher order resonances from a design perspective, it is therefore more interesting to compare the accuracy of capturing resonance peak one. The mean value therefore only includes the first resonance peak from all inlet flow speeds for each studied turbulence model respectively, shown in Table 5.2. It can be observed that $k-\varepsilon$ has an overall higher accuracy in capturing transmission loss resonance peak compared to SST $k-\omega$. Together with the data in Table 5.1, concludes that $k-\varepsilon$ turbulence model increases accuracy in capturing transmission loss characteristics compared to SST $k-\omega$ in the studied case. Therefore, the $k-\varepsilon$ turbulence model was chosen as the most optimal choice between the studied eddy-viscosity models.

Property	Δf [%] (500 Hz)								Mean [%]
Inlet flow speed	21 m/s			41 m/s			61 m/s		
Resonance peak	1	2	3	1	2	3	1	2	
Numerical setup $k-\varepsilon$	9.6	7.2	8.4	8	7.8	4.6	13	9	8.45
Numerical setup $k-\omega$	13.6	6.2	8.4	9	7.8	4.6	14	12	9.45

Table 5.1: A comparison of difference in eigenfrequency shift scaled with the lowest studied acoustic frequency 500 Hz, comparing TL result from the two presented numerical setups using CM, BM and both $k-\varepsilon$ and $k-\omega$ turbulence models. Mean value is taken over all resonance peak and inlet flow speeds.

Property	ΔTL [%] (1:st peak)								Mean [%] 1:st peak
Inlet flow speed	21 m/s			41 m/s			61 m/s		
Resonance peak	1	2	3	1	2	3	1	2	
Numerical setup $k-\varepsilon$	10.6	2.8	7.2	16.5	15.6	67	7.2	0.7	11.4
Numerical setup $k-\omega$	16.1	1.5	0.3	18.1	20.3	53	11.4	5.1	15.2

Table 5.2: A comparison of difference in peak transmission loss scaled with the resonance peak 1 for each flow speed respectively, comparing TL result from the two presented numerical setups using CM, BM and both $k-\varepsilon$ and $k-\omega$ turbulence models. The mean value is only calculated using peak 1 resonance values.

The reason why TL results from CFD simulations for all flow conditions are slightly different in comparison to the experimental data could depend on many different parameters. Since the experimental study was conducted with the real inlet duct system including the corrugated pipe bellow regions, while the CFD simulations simplified the computational domain by removing the two bellows could create differences in the resulting TL. There also exists uncertainty in the experimental data since the study was conducted separately from this study and therefore unknown parameters like duct-silencer leakage or measurement errors could have influenced the experimental results negatively. At the same time, it was observed from studying different numerical options that CFD mesh quality influence both amplitude and frequency shift in TL. The resulting difference in TL amplitude and eigenfrequency shift is not a result of inaccurate TL calculation method. Both decomposition method and two-source method captured the same eigenfrequency shift. However, the two-source method possibly increased accuracy in TL amplitude since the decomposition method was slightly overestimating. Using the two-source method would therefore increase the difference between CFD and experimental results, at least for TL amplitude difference. Therefore, the most likely reason behind the diminished acoustic performance in CFD numerical setup is either a question of mesh quality or choice of fundamental turbulence description. It is possible that the eddy-viscosity turbulence models used have limited numerical capacity in describing flow effects on broad and high frequency Helmholtz-like silencer acoustics. More accurate turbulence models like LES, DES or DNS are needed to capture both acoustic wave propagation and turbulent acoustic noise generation in aeroacoustic CFD simulations. Thus, an uncertainty exists in the numerical setup regarding the description of flow effect on Helmholtz resonator acoustic performance. However, it can be seen from comparing the different numerical setups that both wall treatment and choice of turbulence model from different eddy-viscosity models have low impact on the final results of flow effect on CFD transmission loss calculation.

The flow effect on TL characteristics could most optimally, considering both accuracy and numerical efficiency, be captured with the basic mesh, $k-\varepsilon$ turbulence model, decomposition method with close microphones for the bent duct computational domain. Thus, this was the final choice of numerical setup. Figure 5.16 shows the best and final transmission loss results for the three different inlet flow speeds studied using the most optimal numerical setup based on the presented study of numerical options. If the proposed numerical setup in CFD would be used for other duct-silencer geometries without experimental data as reference, the information obtained from that study regarding TL would resemble the obtainable information in Figure 5.16.

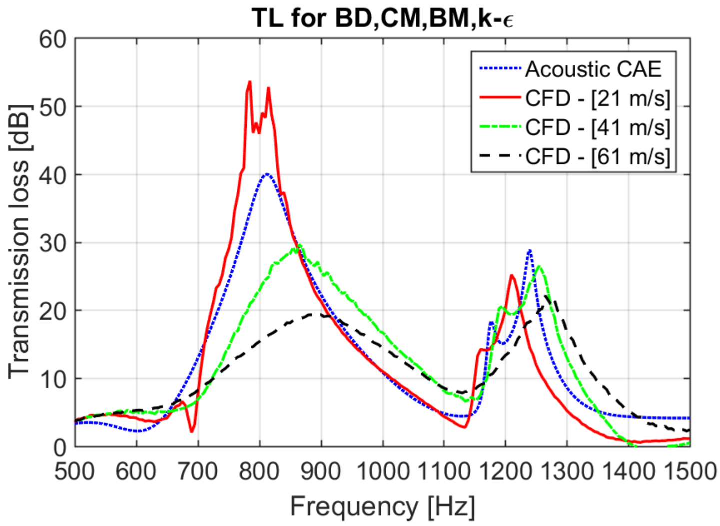

Figure 5.16: Final transmission loss result from the most optimal numerical setup in CFD for the three studied inlet mean flow speeds compared to the acoustic CAE as reference.

5.4 CFD - Geometrical changes of the straight duct geometry

The final numerical setup obtained in Section 5.3 could both capture amplitude reduction and frequency shift from grazing duct flow effect on silencer acoustic performance for the bent duct geometry. It was therefore interesting from an acoustic point of view, whether the degradation of acoustic performance of the silencer-duct system could be improved under duct flow condition. Could any geometrical changes to the silencer-duct system influence the flow in such a way that the diminishing flow effect on transmission loss would not be as effective? Could this effect be captured with the chosen numerical setup?

Since the flow effect on acoustic performance of the silencer is directly related to the grazing flow passing the Helmholtz resonator neck orifices and flow entering the necks, any geometrical change would have to affect the flow in the neck regions. Any geometrical change to the silencer itself is neglected since any change to resonator neck- and cavity geometry, size and location would change the fundamental acoustic behaviour of the silencer. The TL results would thus be impossible to compare with the given silencer geometry TL results. Any geometrical change would then have to be located in the duct system, affecting the flow passing the neck orifices. However, the given bent duct geometry includes a complex rotating flow behaviour passing the neck orifices. Hence, any geometrical changes in the duct aimed to affect the flow passing the neck orifices would have to be related to the rotating flow, which would add an additional layer of complexity. When changing the duct geometry, the pressure drop of the duct system would also be affected, most likely negatively.

Therefore, any geometrical duct change aims to minimize any negative augmentation on pressure drop while still effectively altering the grazing neck orifice flow to improve silencer acoustic performance.

The straight duct computational domain is created in order to one: remove the vorticity of the duct flow and thus be able to compare the influence of the rotating flow on TL and two: removing the vorticity enables any geometrical duct changes to be made with influence from less related flow parameters. The straight duct geometry will mainly cause a straight flow through the duct, parallel to the duct walls. Since the pattern of Helmholtz resonator necks of the silencer are aligned parallel with the duct walls in the duct region, the neck orifices will thus be aligned with the flow. Any small or large geometrical change to the straight duct geometry in order to control or affect the grazing neck orifice flow will therefore be easier than changing the geometry for the bent duct geometry. From studying how the flow can be affected in a straight duct in order to improve performance, similar geometrical changes can be introduced and studied for any arbitrary silencer-duct system related to the specific flow behaviour.

The two following sections will present the flow and acoustic results of the straight duct geometry (reference) and two of the six geometrical changes that were developed and studied. Creating different geometrical changes of the duct geometry was a developing process, the two presented changes were the first and last geometry alterations created, where the last change showed the best acoustic improvement. All CFD simulations with the straight duct geometry are performed with a basic mesh methodology, $k-\varepsilon$ turbulence model and transmission loss is calculated using the decomposition method with microphones placed close to the silencer. Only one inlet flow speed of 41 m/s is studied in order to increase simulation time spent on studying different geometrical designs rather than different inlet flow speeds; since no experimental data of TL for different inlet flow speeds is available for the straight duct system. Contour plots presenting flow behaviour on a cut-through plane of the silencer and duct section is placed in the centerline of the center-row of necks. Contour plots of velocity uses the dimensionless velocity variable scaled with the mean inlet flow speed of 41 m/s.

5.4.1 Straight duct computational domain (Reference)

Initially, the flow and acoustic results from CFD simulation with the straight duct computational domain is presented. The results with geometrical changes of the straight duct geometry is compared to the results from this reference simulation in order to observe a change in acoustic performance. Figure 5.17 shows the dimensionless velocity profile contour plotted on the described cut-through plane. Jets of flow entering the resonator cavity can be observed in the downstream necks of each resonator respectively. A straight developed flow velocity profile is present in the duct and can be seen to slow down passing the silencer. The flow now follows the initial thought of choosing a straight duct geometry, the vorticity in the duct flow is removed.

Turbulent kinetic energy in the flow is now contour plotted on the same plane in Figure 5.18. The generation of turbulence due to the created shear layer flow between neck and duct fluid can be observed and will be an important flow field to study for the different geometrical changes. It can be seen that the turbulent kinetic energy is increased in the grazing flow as it passes the resonator necks and that the turbulent kinetic energy is stronger for the first resonator compared to the second. The increasing turbulent kinetic energy is most likely an effect from the resonator necks now aligning with the grazing flow direction.

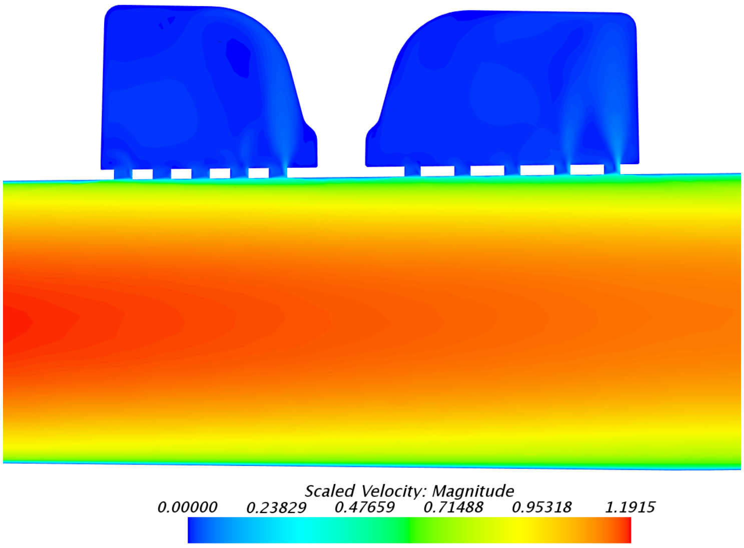

Figure 5.17: Magnitude of dimensionless scaled velocity contour plotted on a duct-centered cut-through plane in the silencer region. Flow direction from left to right.

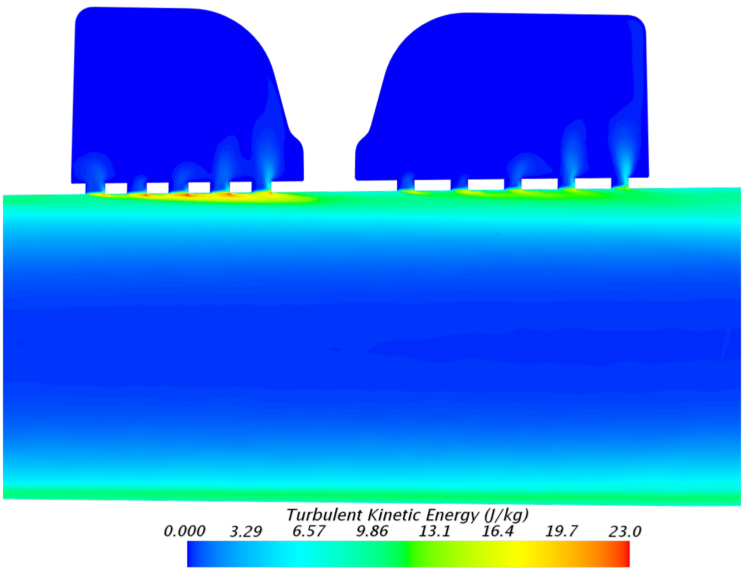

Figure 5.18: Turbulent kinetic energy contour plotted on a duct-centered cut-through plane in the silencer region. Flow direction from left to right.

Figure 5.19 shows the dimensionless velocity plotted in the "Mid_Cyl_Holes[j]" direction (aligning parallel with the necks) on the surface orifices of the resonator necks, where positive direction is flow entering the resonator neck and cavity. It can be seen that the flow in the resonator necks are now more or less symmetric compared to the bent duct geometry governed strongly by the passing duct flow vorticity. Flow now enters the resonator at the downstream row of necks for both resonators as well as through top and bottom rows of necks. Flow enters the downstream row due to grazing orifice flow being slowed down passing each neck orifice and thus is most prominent to enter through the last neck. The necks on the top and bottom are necks where flow have the easiest potential to enter due to angle between duct and neck. Center-row neck orifices are normally directed outwards from the duct while the top and bottom necks are aligned with the center row thus reducing the angle between neck and duct. Flow leaves the resonator through the remaining neck orifices. No strong jet flow can be observed to enter the duct flow similar to the bent duct geometry.

The friction velocity is contour plotted on the duct surface in the region around the silencer in Figure 5.20. It can be seen from the figure that flow direction is directly aligned with the row of necks. Where the grazing flow after each hole is disturbed and slowed down, reducing the friction velocity, possibly enabling flow to enter the resonator house in the trailing row of necks. It can also be seen that the leading row of necks as well as the top and bottom row of necks have the highest friction velocity. It seems like the increased friction velocity around the leading row of necks could be caused by inaccurate resolution of boundary layer flow, due to the prism layer mesh retracting inside the necks.

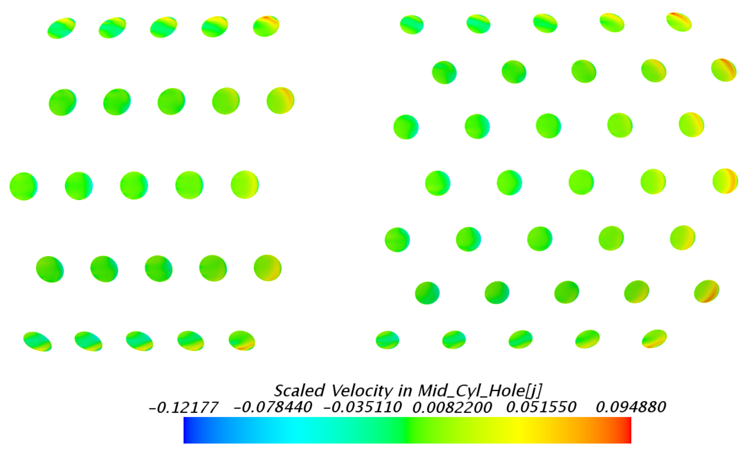

Figure 5.19: Dimensionless scaled velocity in the direction of the neck extrusions contour plotted on the neck orifice surface, positive direction towards the resonator cavity. Flow direction from left to right.

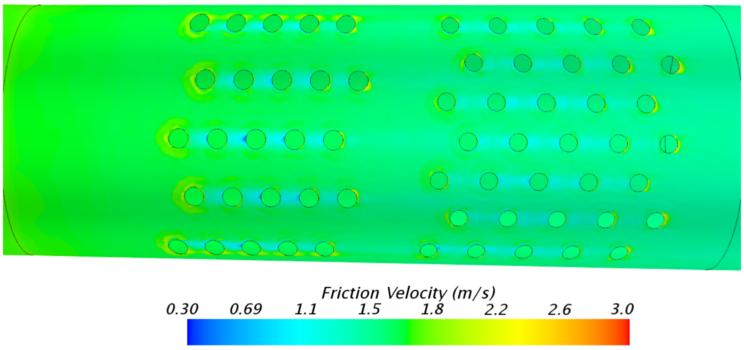

Figure 5.20: Friction velocity plotted on the duct wall surface in close proximity to the silencer. Flow direction from left to right.

Transmission loss is calculated with the reference straight duct and compared to the bent geometry, experimental results of the same inlet flow speed 41 m/s and results from acoustic CAE in Figure 5.21. It can be seen that the transmission loss characteristic of the straight duct geometry is similar to the CFD results from the bent duct geometry. The same three eigenfrequency peaks are present since the geometry of the silencer was kept unchanged. Removing the vorticity in the flow however, increases the flow effect on frequency shift by 40 Hz (855 to 895 Hz) and reduces the transmission loss amplitude by 5 ± 0.5 %.

The increased degrading flow effect on silencer performance is most likely the result of aligning the row of necks with the flow direction. The shear layer is strengthened and generated turbulence is increased as the grazing flow passes over each neck orifice. The acoustic interaction between the silencer and duct is therefore further degraded and thus the performance of the silencer is reduced for the straight duct compared to the bent duct geometry. Designing efficient multi-neck Helmholtz-like resonator silencers in relation to flow effect could take the incident grazing duct flow into consideration when developing resonator hole pattern. It also makes the inlet velocity flow profile to the duct system more relevant when developing the CFD numerical setup. If the flow behaviour in the real inlet air duct system is heavily affected by duct parts before or after the silencer-duct section, it can affect the resulting flow effect on the silencer acoustics, for example strong vortex flow from a turbo-compressor.

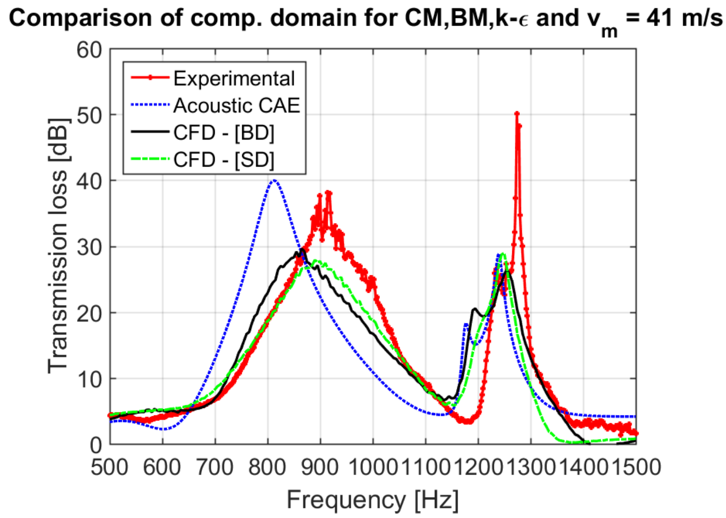

Figure 5.21: A comparison between transmission loss results from acoustic CAE, experimental data and CFD data from both simulations of bent and straight duct geometry with inlet mean flow speed of 41 m/s.

5.4.2 Geometry change configurations

This section will present two different geometrical changes to the straight duct geometry. Six different geometrical changes were made in total, where the common idea of geometrical change were to create an internal duct protrusion upstream of the silencer to disturb grazing flow passing the neck orifices. There are endless design options in how to disturb the flow internally in the duct. However, any arbitrary internal protrusion in the duct will increase flow resistance depending on the size, increasing turbulence and hence increasing the pressure drop of the duct system. Geometrical duct changes in an air intake duct system are now part of a bigger subject, increasing pressure drop over a duct section in a powertrain air-breathing system reduces combustion engine performance. Hence, any internal duct protrusion is designed to minimize its effect on pressure drop while improving flow effect degradation on silencer acoustic performance.

The geometrical changes were performed on the straight duct computational domain in the pre-processing program ANSA and exported similarly to Star-CCM+ as other defined computational domains. Volume mesh where then created in Star-CCM+ based on the basic mesh methodology with some slight improved mesh resolution in the region surrounding the protrusion. The two presented geometrical changes are called the: *Ridge x1* and *Stamp Full*. The resulting geometry, flow and acoustics of the two duct alterations follows.

The first geometrical change developed was the Ridge x1, an internal ridge/3D edge covering half the duct circumference, placed upstream of the leading row of necks of the first resonator. An overview of the geometrical change (purple) can be seen in Figure 5.22, one picture directly taken above the silencer and one cut-through picture where half the duct can be seen from the inside. It was deliberately chosen such that the ridge aligns the resonator angle and not placed perpendicularly to the duct. Thus, the flow from the ridge has to travel equally far to each row of holes. The geometrical change is defined with the surface mesh "Bead"-option through certain parameters in ANSA and is presented in Table 5.3. Since the duct diameter upstream of the silencer is $D_{in} = 0.07$ m, the ridge covers 7 % of the duct diameter. For a schematic picture of surface and volume mesh surrounding the Ridge x1 alteration, see Appendix A.3.

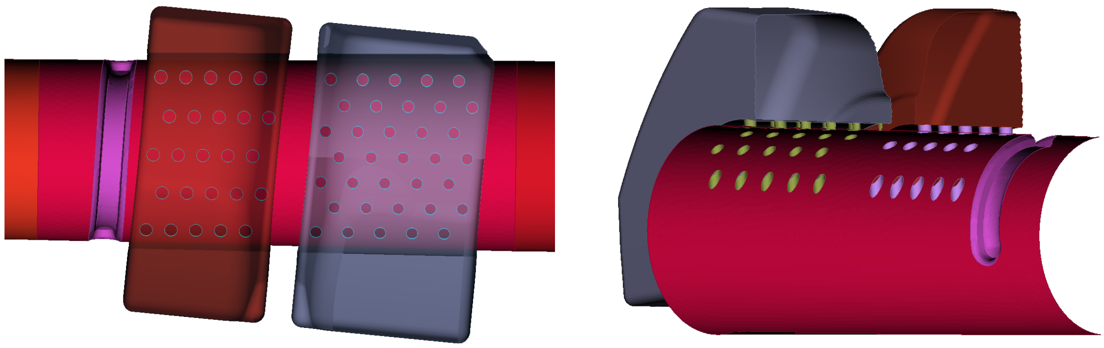

(a) (b)

Figure 5.22: An overview of the Ridge x1 geometrical change (purple), (a) shows the geometrical change from above the straight silencer-duct system and (b) shows the inside of the duct plus geometrical change with a cut-through.

Geometrical variable	Width [mm]	Height [mm]	Angle	Radius [mm]
Value	10	5	75°	2

Table 5.3: Geometrical variables and their respective values chosen for the Ridge x1 geometrical change in ANSA ("Bead"-option).

Figure 5.23 and 5.24 shows the resulting dimensionless velocity and turbulent kinetic energy field of the flow from the Ridge x1 geometrical duct change, contour plotted on a cut-through centered plane. The Ridge x1 alteration heavily influences the flow field downstream of the change. In Figure 5.23, it can be observed that flow internally separates from the duct wall at the trailing edge of the ridge before grazing the neck orifices. The large region of low velocity continues far downstream of the silencer. Simultaneously, the neck flow of the first resonator is completely changed compared to the straight duct reference case in Figure 5.17. The magnitude of the dimensionless flow velocity is increased inside the necks of the first resonator due to an increase in fluid neck mass-flow, forcing the fluid through a contracting duct (neck) due to the duct flow separation.

In Figure 5.24, the turbulent kinetic energy of the flow is increased by a factor four due to the geometrical change compared to the reference case in Figure 5.18. The shear layer flow in the neck orifices is completely removed for the first resonator and is affected for the second resonator due to a change in neck flow behaviour and downstream grazing flow.

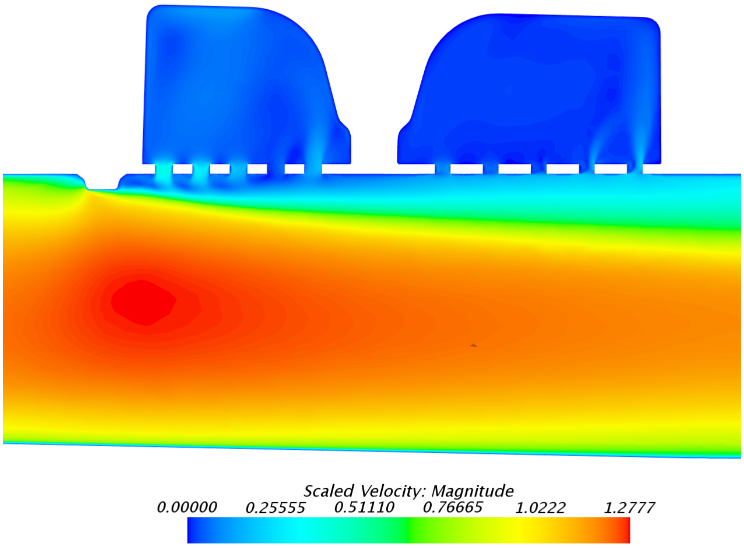

Figure 5.23: Magnitude of dimensionless scaled velocity contour plotted on a duct-centered cut-through plane in the silencer region for the Ridge x1 geometrical change. Flow direction from left to right.

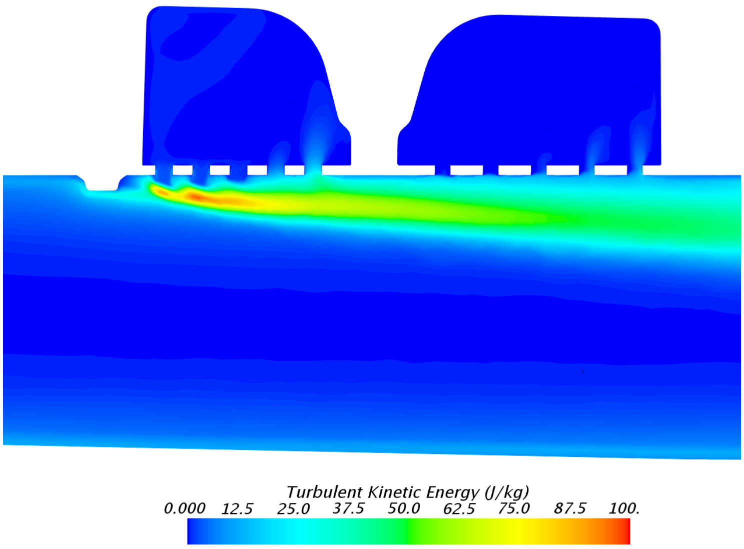

Figure 5.24: Turbulent kinetic energy contour plotted on a duct-centered cut-through plane in the silencer region for the Ridge x1 geometrical change. Flow direction from left to right.

Figure 5.25 and 5.26 presents the dimensionless velocity in the neck direction on neck orifice surfaces and friction velocity on the duct surface with contour plots from the Ridge x1 geometrical change.

The flow pattern shown in Figure 5.25, for both the first and second resonator is very different compared to the reference straight duct geometry. The duct flow separation causes a greatly increased neck mass-flow and thus speed (top neck flow speed four times as large as reference case), entering the first resonator cavity through the trailing, top and bottom row of necks. This flow phenomena occurs since the center-most holes close to the ridge must feed the duct flow separation with strong outgoing jet-flows, removing any possible recirculating region downstream of the ridge. This resonator neck and cavity flow behaviour is directly forced by the separation from the geometrical change. The second resonator show similar neck flow behaviour but with less strength. The plotted duct wall friction velocity in Figure 5.26 show how the flow has to accelerate passing the internal ridge and a large region of greatly increased turbulent flow downstream, covering almost the full silencer-duct region.

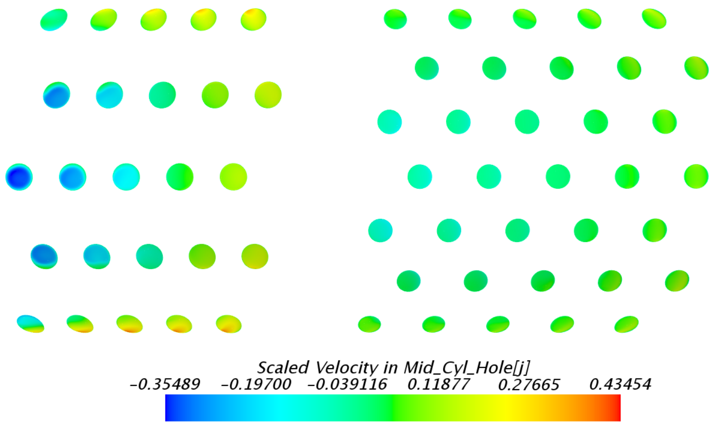

Figure 5.25: Dimensionless scaled velocity in the direction of the neck extrusions contour plotted on the neck orifice surface for the Ridge x1 geometrical change, positive direction towards the resonator cavity. Flow direction from left to right.

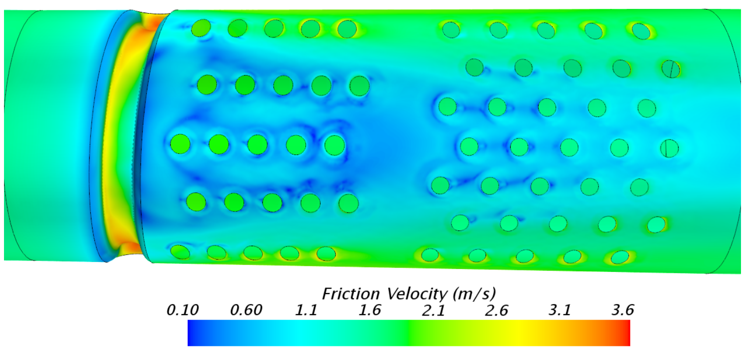

Figure 5.26: Friction velocity plotted on the duct wall surface in close proximity to the silencer for the Ridge x1 geometrical change. Flow direction from left to right.

After several iterations of different geometrical changes, the last iteration and second to be presented in this thesis is the Stamp Full geometrical change. Micro-geometrical protrusions are placed upstream and in close proximity of all silencer neck orifices to locally disturb the grazing flow compared to the macro-geometrical change of the Ridge x1 design. An overview of the Stamp Full geometrical change (yellow) can be seen in Figure 5.27, one picture directly taken above the silencer and one cut-through picture where half the duct can be seen from the inside. The alteration makes use of the ANSA surface mesh "Stamp"-option and the geometrical parameters used are presented in Table 5.4. Geometrically, the protrusions in Stamp Full are roughly three times smaller in both height and width (diameter) compared to the Ridge x1 design. Since the size of the protrusions are smaller than the neck diameter as well as positioned in close proximity of the necks, similar mesh surface and volume cell-size in the surrounding regions are selected, see Appendix A.3 for schematic pictures.

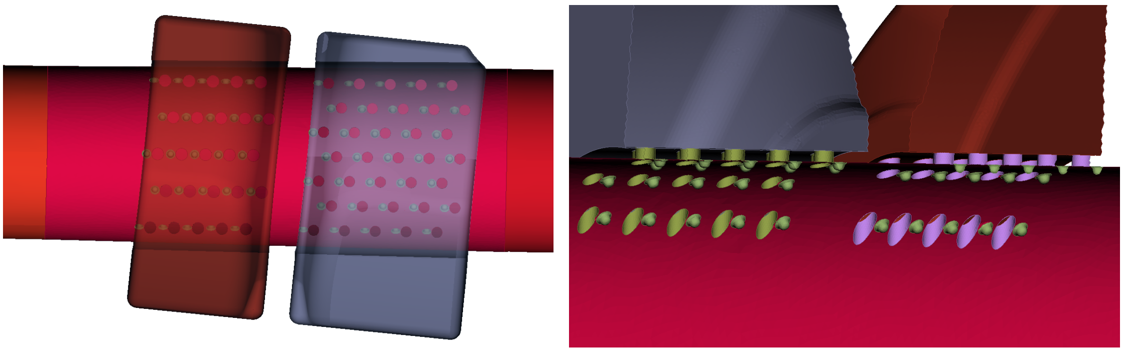

(a) (b)

Figure 5.27: An overview of the Stamp Full geometrical change (yellow), (a) shows the geometrical change from above the straight silencer-duct system and (b) shows the inside of the duct plus geometrical change with a cut-through.

Geometric variable	Diameter	Height	Radius 1	Radius 2
Value [mm]	3	1.75	0.5	1

Table 5.4: Geometrical variables and their respective values chosen for the Stamp Full geometrical change in ANSA ("Stamp"-option).

Figure 5.28 and 5.29 presents the resulting dimensionless velocity and turbulent kinetic energy field of the flow from the Stamp Full geometrical duct change, contour plotted on the same cut-through centered plane. The small protrusions does not affect the duct flow on a large scale but it can be observed that the neck flow regions are affected, comparing the flow and turbulent kinetic energy field of the straight duct geometry and stamp full geometrical change. In Figure 5.28, strong jet flows are entering the second resonator increasing in strength downstream. A very different neck flow behaviour compared to Ridge x1 results in Figure 5.23, closer resembling the reference case flow behaviour in Figure 5.17. Figure 5.29 show a slight increase in peak turbulent kinetic energy (roughly 50 % increase) compared to the reference case. The protrusion locally increases the turbulence over the orifices but also removes the neck orifice shear layer flow.

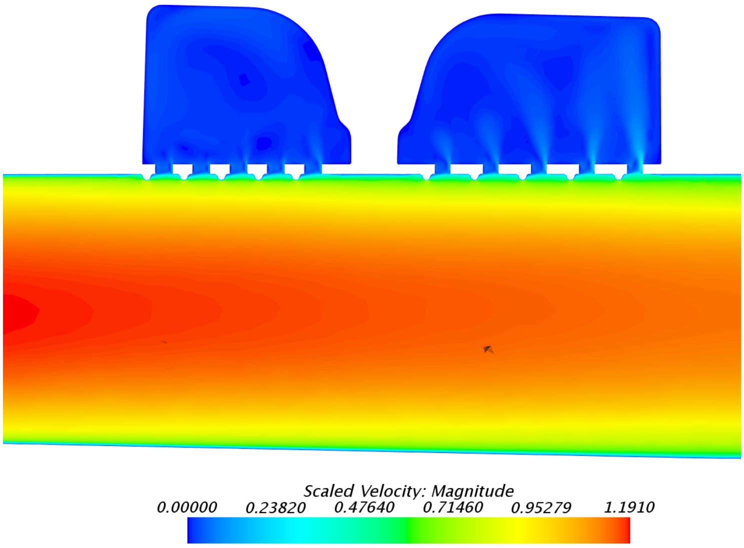

Figure 5.28: Magnitude of dimensionless scaled velocity contour plotted on a duct-centered cut-through plane in the silencer region for the Stamp Full geometrical change. Flow direction from left to right.

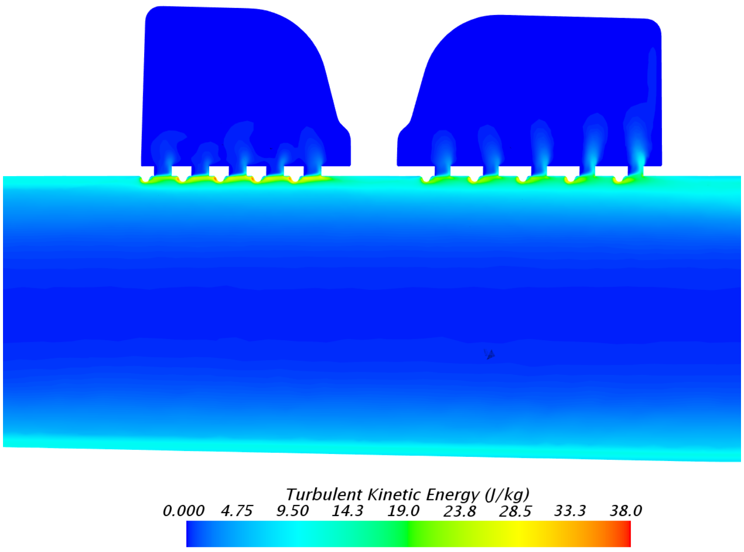

Figure 5.29: Turbulent kinetic energy contour plotted on a duct-centered cut-through plane in the silencer region for the Stamp Full geometrical change. Flow direction from left to right.

Figure 5.30 and 5.31 shows the dimensionless velocity in the neck direction on neck orifice surfaces and friction velocity on the duct surface with contour plots for the Stamp Full geometrical change. Figure 5.30 also include outlines of the protrusions to relate their positions to the neck flow behaviour. The neck flow behaviour in Figure 5.30 is very different in comparison of both the Ridge x1 simulation and reference case. Flow entering the resonator cavity is now present in all necks, where the highest entering flow speeds can be observed to occur in centered streaks downstream of each protrusion. By also studying the turbulent kinetic energy captured in the centerline, it seems like the protrusions are small enough to prevent local flow separation. Instead, the flow continues to attach to the wall and follows the geometrical change, directing the flow towards the necks, increasing the entering neck flow speed. It must therefore follow that the flow on either side of the entering flow inside the necks are leaving the resonator cavity and looking at Figure 5.30, at relatively low speed.

In Figure 5.31, it can be seen how the small protrusions causes the flow to accelerate on the protrusion but also disturbs and directs the flow around the protrusion. By forcing the flow around the protrusions, also prevents grazing flow passing the neck orifices and instead flows in-between the lateral neck rows. Further, preventing orifice grazing flow indirectly allows flow to both enter and leave the resonator cavity simultaneously through the neck, seen in Figure 5.30.

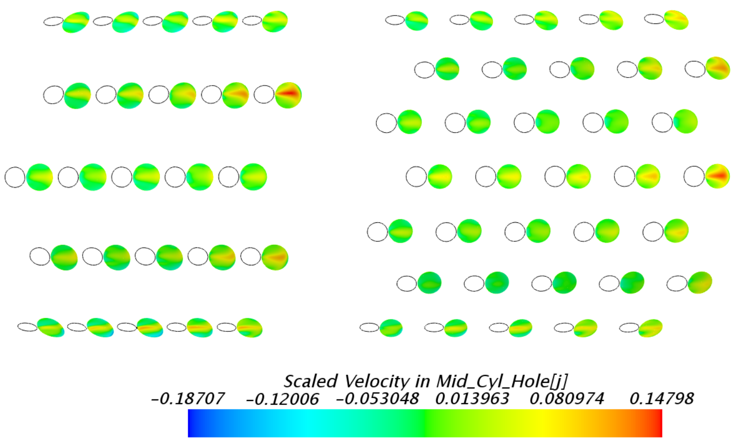

Figure 5.30: Dimensionless scaled velocity in the direction of the neck extrusions contour plotted on the neck orifice surface for the Stamp Full geometrical change, positive direction towards the resonator cavity. Flow direction from left to right.

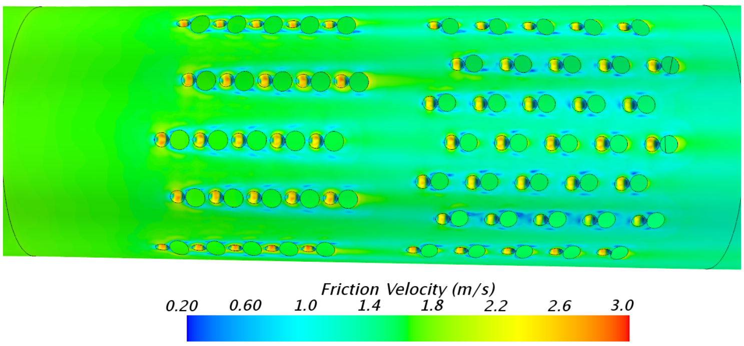

Figure 5.31: Friction velocity plotted on the duct wall surface in close proximity to the silencer for the Stamp Full geometrical change. Flow direction from left to right.

A comparison between the resulting transmission loss characteristics of the two presented geometrical changes, straight duct reference case and acoustic CAE for the no-flow conditional reference is presented in Figure 5.32. It can be seen that the CFD numerical setup capture a change in acoustic performance of the duct-silencer system, due the geometrical change of both presented designs. Moreover, it can also be observed that both designs remove the first eigenfrequency shift due to grazing neck orifice flow. The silencer-duct system including geometrical change is now reducing noise in the frequency band it initially was designed for, by comparing the TL with geometrical changes to acoustic CAE. A difference in TL amplitude can also be observed comparing the two presented designs. The first design, Ridge x1, reduces the amplitude of TL for the first peak compared to the reference case slightly. However, the second design Stamp Full improve the TL amplitude performance of the silencer-duct system compared to the reference case. Since the flow alteration were made in the duct and not inside the resonator cavity, the second and third resonance peak almost remain unchanged for both geometrical changes. A slight reduction in TL amplitude can be seen with the Ridge x1 design for the higher-modes of eigenfrequency.

Moreover, the resulting pressure drop and improved degradation of flow effect on transmission loss characteristics for all studied geometrical changes are presented in Table 5.5. Pressure drop is measured between duct orifices and pressure drop difference in percent is in relation to the reference case. Frequency shift Δf for first resonance peak is in relation to the first eigenfrequency peak calculated with Acoustic CAE, representing no-flow condition of silencing properties. Presented results of TL amplitude for first resonance peak are also compared to the reference case. The last design Stamp Full is the best performing duct alteration since it only increases pressure drop by 1.1 %, removes frequency shift and increases transmission loss peak value with 15 %, which can also be seen in Figure 5.32.

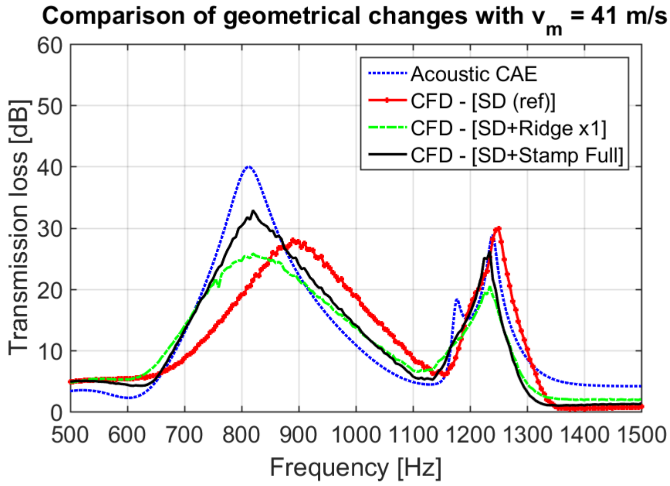

Figure 5.32: A comparison between transmission loss results from acoustic CAE and CFD data from straight duct geometry including results from the two presented geomtrical changes with inlet mean flow speed of 41 m/s.

Simulation case for SD	Δp [Pa]	Δp_{diff} [%]	Δf **Peak 1** [$\pm$ 0.5 %]	**TL Amplitude Peak 1** [$\pm$ 1 %]
Reference	634.46	-	10	-
Ridge x1	716.7	12.9	1.2	-8.9
Ridge x2	784.8	23.7	1.2	-14.3
Stamp	636.4	0.3	9.2	1.7
Stamp Half	639.75	0.8	5	7.1
Stamp Half Rect	692.4	9.1	1.2	-16.8
Stamp Full	641.9	1.1	1.2	15

Table 5.5: Resulting properties from the reference case as well as all six geometrical changes of the straight duct, Δf for all cases are related to Peak 1 eigenfrequency of Acoustic CAE and TL amplitudes are compared to reference case.

Generally, it can be noted that four out of six configurations in Table 5.5 remove the frequency shift. This means that disturbing grazing flow passing Helmholtz resonator necks increases the acoustic interaction between resonator and duct. Both local micro-geometrical adjustments and large scale macro-geometrical adjustments are effective as long as the flow it disturbs passes the neck orifice, preventing strong shear layer flows to be developed. Also taking pressure drop into account, renders the micro-geometrical adjustments (Stamp) more effective overall compared to macro-changes.

The amplitude of transmission loss is varying both positively and negatively, comparing the results of the different geometrical changes. In general, flow inside the resonator necks are responsible for the flow effect of reducing transmission loss amplitude with duct mean flow. It is known that an increase in mean duct flow speed reduces silencer transmission loss, since the flow speed inside the necks increases proportionally with duct flow speed, see Appendix A.4. Therefore, increasing the flow speed in resonator necks most likely reduces transmission loss for the first resonance. However, increasing duct mean flow speed does not necessarily change the flow pattern for the necks. For example, an increasing duct mean flow in the bent duct geometry will not affect the flow pattern entering and leaving the resonator cavity as it is governed by the vorticity, see Appendix A.5. The flow pattern could however change for low flow speeds under 21 m/s, not studied in this project. But for such low flow speeds, the acoustic performance is unaltered by flow effects.

By studying the neck flow patterns for the reference case, Ridge x1 and Stamp Full in Figure 5.19, 5.25 and 5.30, it can be seen that Ridge x1 has the highest flow speeds entering and leaving the necks. One possible explanation why TL is reduced with 8.9 % for Ridge x1 is thus obtained. However, Stamp Full has approximately 60 % increased top flow speed entering and leaving the resonator cavities through the necks compared to reference case, while increasing TL with 15 %. Therefore, reduction of transmission loss due to mean duct flow depends on more flow parameters than neck flow speed. One possible flow behaviour affecting TL are the neck flow pattern, both globally for all necks and locally in each neck. For example, most of the necks in Stamp Full have flow going both in an out simultaneously while all other simulation cases show either that

- all necks act as inflow or outflow to/from resonator cavity (Ridge x1)
- one part of necks include a major part of inflow and outflow while the rest have low inflow and outflow (Bent duct geometry).

One possible explanation could therefore be that necks with parallel flow in only one direction inhibits the volume of air inside the neck to fully resonate, thus reducing the effectiveness of that neck locally affecting the total Helmholtz resonator efficiency leading to reduced TL. Further, necks with parallel flow in both directions only affects the resonance of the neck air volume to a lesser extent compared to single direction neck flow, acting similar to a neck with stagnant air (maximum attenuation). This theory needs further studying but could describe the occurring flow effect on transmission loss amplitude for a multi-neck Helmholtz-like resonator.

One possible negative phenomenon that could occur naturally by introducing internal duct protrusions is an increased generation of turbulent flow noise. The larger geometrical change of Ridge x1 increases turbulent kinetic energy roughly by a factor of four compared to straight duct reference case, which might lead to an increase in flow noise generation. The small protrusions of Stamp Full however, does not lead to a large increase in turbulent kinetic energy and thus probably leads to no or a low increase in flow noise. Most noise in the intake air system is generally generated by turbo-compressors and if flow noise is only slightly increased by micro-geometrical alterations, the topic of noise generation by the alterations is unessential. Turbulent flow noise generation by the geometrical changes as well as potential tonal whistling effects from neck orifices or duct protrusions (not discussed in this thesis) could numerically be described with direct noise simulations using LES, DES or DNS in future studies.

6 Conclusion

Acoustic CAE is a well established, highly accurate and efficient numerical method capable of capturing the acoustic transmission loss performance for complex silencer-duct systems. However, the methodology lacks the capability of numerically capturing duct mean flow effects on silencer acoustic performance, which is important to account for when designing efficient air intake silencers. The established CFD methodology developed by Selamet and Iqbal have been further studied, developed and streamlined in this Master's thesis project. The presented CFD methodology can with reasonable accuracy and improved efficiency capture flow effect on a high-frequency broad-band Helmholtz-like silencer in a complex real air intake system. CFD including acoustic wave propagation is a numerically complex and computationally expensive method but a strong and effective tool in aiding air intake silencer design, noise mitigation research in combustion engines as well as other areas of interest. The CFD methodology is not developed to replace acoustic CAE but instead to be seen as a way to obtain additional information about silencer performance under duct mean flow-condition.

The CFD setup was developed and applied using the commercial CFD software Star-CCM+, studying the high frequency silencer acoustic behaviour with several duct mean inlet flow speeds. Using Star-CCM+, the usability of the methodology was improved from previous research by increasing the number of possible frequencies studied simultaneously in one simulation to an arbitrary number. Making it possible to study any acoustic wave frequency band of interest, assuming duct acoustic plane wave propagation. The impact of different turbulence models as well as wall treatments gave new insight into the choice of numerical models and methods. The choice of microphone location in relation to silencer due to duct resonances were also outlined as an important parameter in describing the acoustic performance with good accuracy. Since acoustic duct resonances were an area of interest, the two-source measuring technique to capture transmission loss was integrated into the CFD simulation setup to increase accuracy at the expense of increased computational cost. The previously utilized decomposition measuring method is then validated by comparing the CFD transmission result of the two measuring methods, and further studied due to the methods computational efficiency. The most optimal resulting CFD methodology was able to capture transmission loss characteristics with reasonable accuracy, under predicting the resulting eigenfrequency shift with roughly 8.5 % difference for all flow speeds; as well as a 11.4 % transmission loss peak difference, both in comparison to experimental data.

The optimally developed CFD setup in relation to choice of numerical parameters were then employed; to study how different duct geometrical alteration can affect the grazing neck orifice flow, in order to improve silencer acoustic performance under flow effect. Through a numerically empiric process, six different geometrical changes were developed with varying strategies. The different changes resulted in varying success of the studied parameters, low increase in pressure drop and improved transmission loss characteristics. The best design included small circular perturbations positioned in the duct, in front of each Helmholtz resonator neck disturbing the grazing neck orifice flow, destroying the accumulating neck orifice shear layer as well as changing the multi-neck flow pattern. Resulting in a 15 % increase in first order resonance peak transmission loss and removal of eigenfrequency shift as well as only increasing pressure drop by 1.1 %, in comparison to a reference simulation.

Finally, it can be concluded that flow effect on the acoustic performance of a complex silencer can be captured employing the presented CFD methodology with reasonable accuracy. Accuracy and computational efficiency in CFD including acoustic (computational aeroacoustics) are sensitive to choice of numerical setup and parameters. Small geometrical changes through the alteration of grazing Helmholtz resonator neck orifice flow can improve silencer acoustic performance under flow effect.

7

Future work

The first thing of interest to further study would definitely be to implement the best geometrical change in the bent duct geometry. Here, the positions of the protrusions would have to be related to the generated duct flow vorticity to disturb the grazing neck flow locally. If simulations would still show an improved silencer acoustic performance under flow effect for different inlet mean flow speeds, an experimental study of the geometrical changes is necessary to validate the numerical results. The experimental studies could both include a similar decomposition measurement method presented in this thesis as well as noise mitigation measurements from an intake air system including the studied silencer and geometrical changes performed in a real combustion-engine.

It would also be interesting to test the developed CFD methodology on other silencer-duct systems. Studying how neck flow patterns and duct geometrical features affect the silencer acoustic performances, increasing the knowledge needed to design effective intake air silencers and other ducted noise mitigation devices including flow. For example, the method could be used to describe silencers placed on ducts downstream of the turbo-compressor or mufflers in the exhaust system where air is in a non-atmospheric condition.

Finally, the numerical setup in CFD could be further studied and optimized to increase numerical accuracy and improve computational efficiency. The developed meshing methodologies including low-Reynolds number wall treatment need further investigation to capture the interesting transmission loss characteristics. It could be interesting to further study the necessary surface cell size in the resonator neck and cavity region as well the chosen time step to obtain highly accurate acoustic results. Expanding the numerical setup to simulate turbulent flows using more complex turbulence models like LES or DES instead of eddy-viscosity models could also give more insight into the the effect on acoustic performance from choice of turbulence model. It was also noted that the amplitude of the time dependant boundary condition inducing plane acoustic waves was of importance, possibly hinting at a amplitude dependency of acoustic waves to capture transmission loss in CFD that need further investigation.

Bibliography

[1] Senate Public Works Committee, Noise Pollution and Abatement Act of 1972, S. Rep. No. 1160, 92nd Cong. 2nd session

[2] Hogan CM, and Latshaw GL. The relationship between highway planning and urban noise. Proceedings of the ASCE Urban Transportation Division Environment Impact Specialty Conference, May 21-23, 1973, Chicago, Illinois. *ASCE*

[3] European Commission. The Green Paper on Future Noise Policy (`https://web.archive.org/web/20101123022847/http://ec.europa.eu:80/environment/noise/pdf/com_96_540.pdf`). Archived from the original (PDF) on 23 November 2010. Retrieved 22 June 2017.

[4] Wallin HP, Carlsson U, Åbom M, Bodén H, and Glav R. Sound and Vibration. Revised English version. Stockholm: KTH Aeronautical and Vehicle engineering, Marcus Wallenberg laboratory; 2014.

[5] McAuliffe CE. The influence of high speed air flow on the behavior of acoustical elements. Thesis (M. S.). *Cambridge: Massachusetts Institute of Technology*; 1950. Available from: `http://hdl.handle.net/1721.1/74994`. Retrieved 22 June 2017.

[6] Meyer E, Mechel F, and Kurtze G. Experiments on the influence of flow on sound attenuation in absorbing ducts. *JASA*. 1958; 30(3):165-174.

[7] Phillips B. Effects of high-wave amplitude and mean flow on a Helmholtz resonator [Internet]. *Washington: NASA Lewis Research Center*; 1968. NASA-TM-X-1582. Available from: `https://ntrs.nasa.gov/search.jsp?R=19680013954`. Retrieved 22 June 2017.

[8] Anderson JS. The effect of an air flow on a single side branch Helmholtz resonator in a circular duct. *JSV*. 1977; 52(3):423-431.

[9] Hersh AS, and Walker B. Effect of Grazing Flow on the Acoustic Impedance of Helmholtz Resonators Consisting of Single and Clustered Orifices. *JASA*. 1982; 72(2):642.

[10] Allam S, Knutsson M, and Boden H. Development of Acoustic Models for High Frequency Resonators for Turbocharged IC-Engines. *SAE Technical Paper*. 2012. doi:10.4271/2012-01-1559.

[11] Du L, Abom M, Karlsson M, and Knutsson M. Modelling of Acoustic Res-

onators Using the Linearized Navier Stokes Equations. *SAE Technical Paper*. 2016. doi:10.4271/2016-01-1821

[12] Munjal ML. Acoustics of ducts and mufflers with application to exhaust and ventilation system design. New York: Wiley; 1987. pp. 58–60. ISBN 0471847380.

[13] Cummings A. The response of a resonator under a turbulent boundary layer to a high amplitude non-harmonic sound field. *JSV*. 1987; 115(2):321-8.

[14] Ricot D, Maillard V, and Bailly C. Numerical simulation of the unsteady flow past a cavity and application to the sun-roof buffeting. *7th AIAA/CEAS Aeroacoustics Conference and Exhibit, Aeroacoustics Conferences*; 2001 (p. 2112). Available from: `http://dx.doi.org/10.2514/6.2001-2112`. Retrieved 22 June 2017.

[15] W. Tam CK, and Kurbatskii KA. Microfluid Dynamics and Acoustics of Resonant Liners. *AIAA Journal*. 2000;38(8):1331-9.

[16] W. Tam CK, Kurbatskii KA, Ahuja KK, and Gaeta RJ. A numerical and experimental investigation of the dissipation mechanisms of resonant acoustic liners. *JSV*. 2001;245(3):545-57.

[17] Iqbal A, and Selamet A. A two-dimensional computational study of the flow effect on the acoustic behaviour of Helmholtz resonators. *IJVNV*. 2010;6(2/3/4):130.

[18] Selamet E, Selamet A, Iqbal A, and Kim H. Effect of Flow on Helmholtz Resonator Acoustics: A Three-Dimensional Computational Study vs. Experiments. *SAE Technical Paper*. 2011, doi:10.4271/2011-01-1521.

[19] Selamet E, Selamet A, Iqbal A, and Kim H. Acoustics of a Helmholtz Resonator Aligned Parallel with Flow: A Computational Study VS. Experiments. *IJMMM*. 2013:210-213.

[20] Davidson L. Fluid mechanics, turbulent flow and turbulence modeling. Gothenburg (Sweden): Chalmers University of Technology, Department of Applied Mechanics, Division of Fluid Dynamics; 2017. Available from: `http://www.tfd.chalmers.se/~lada/MoF/lecture_notes.html`. Retrieved 22 June 2017.

[21] Atkins T, and Escudier M. A Dictionary of Mechanical Engineering. *Oxford University Press*. 2013; DOI: 10.1093/acref/9780199587438.001.0001

[22] Launder BE, and Spalding DB. Lectures in Mathematical Models of Turbulence. London: Academic Press; 1972.

[23] Wilcox DC. Turbulence Modeling for CFD. 3rd ed. La Canada: DCW Industries; 2006.

[24] Siemens PLM software (CD-adapco) STAR-CCM+ User's Guide. Version 11.06.010. Siemens PLM software (CD-adapco). 2016.

[25] Andersson B, Andersson R, Håkansson L, Mortensen M, Sudiyo R, and van Wachem BGM. Computational Fluid Dynamics for Engineers. 10th ed. Cambridge University Press; 2014

[26] Menter FR. Two-Equation Eddy-Viscosity Turbulence Models for Engineering Applications. *AIAA journal*. 1994;32(8):1598–1605. doi: 10.2514/3.12149.

[27] Spalart PR. Strategies for turbulence modelling and simulations. *IJHFF*. 2000;21(3):252-263.

[28] Menter FR, Smirnov PE, Liu T, and Avancha R. A One-Equation Local Correlation-Based Transition Model. *FTAC*. 2015;95(4):583-619.

[29] White FM. Fluid mechanics. 7th ed. Boston: McGraw-Hill; 2003.

[30] von Kármán Th. Mechanische Ähnlichkeit und Turbulenz. 1930 Nachrichten von der Gesellschaft der Wissenschaften zu Göttingen, Fachgruppe 1 (Mathematik), 5: 58–76 (also as: "Mechanical Similitude and Turbulence", Tech. Mem. NACA, no. 611, 1931).

[31] Versteeg HK, and Malalasekera W. An Introduction to Computational Fluid Dynamics, The Finite Volume Method. 2nd ed. Edinburgh Gate: Pearson Education Limited; 2007. ISBN: 978-0-13-127498-3

[32] Kinsler L, Frey A, Coppens A, and Sanders J. Fundamentals of Acoustics. New York: John Wiley Sons; 2000, Inc. ISBN 0-471-84789-5.

[33] Ingard U. On the theory and design of acoustic resonators. *JASA*. 1953; 25(6):1037-1061

[34] Chung JY, and Blaser DA. Transfer function method of measuring induct acoustic properties. I. Theory. *JASA 68*. 907 (1980); doi: 10.1121/1.384778

[35] Chung JY, and Blaser DA. Transfer function method of measuring induct acoustic properties. II. Experiment. *JASA 68*. 914 (1980); doi: 10.1121/1.384779

[36] Chung JY, and Blaser DA. Transfer function method of measuring acoustic intensity in a duct system with flow. *JASA 68*. 1570 (1980); doi: 10.1121/1.385211

[37] Bodén H, and Abom M. Influence of errors on the two-microphone method for measuring acoustic properties in ducts. *JASA*. 1986; 79(29).

[38] Tao Z, and Seybert AF. A Review of Current Microphone Techniques for Measuring Muffler Transmission Loss. *SAE Technical Paper*. 2003, doi:10.4271/2003-01-1653

[39] Zhanq Q, and Bodony DJ. Numerical investigation of a honeycomb liner grazed by laminar and turbulent boundary layers. *JFM*. 2016;792:936-980. doi: 10.1017/jfm.2016.79

[40] Ghanadi F, Arjomandi M, Cazzolato BS, and Zander AC. Analysis of the turbulent boundary layer in the vicinity of a self-excited cylindrical Helmholtz resonator. *JoT*. 2015; 16(8):705-728. doi: http://dx.doi.org/10.1080/14685248.2015.1024839

[41] Abom M. An Introduction to Flow Acoustics. Stockholm, Sweden 2015. TRITA-AVE 2006:04. ISSN 1651.7660. ISRN/KTH/AVE/N-06/04-SE

[42] Karlsson M, Knutsson M, and Abom M. Predicting Fluid Driven Whistles in Automotive Intake and Exhaust Systems. *SAE Technical Paper*. 2016.

doi:10.4271/2016-01-1820.

[43] Kierkegaard A. Personal communication. 2017.

[44] Courant R, Friedrichs K, and Lewy H. On the partial difference equations of mathematical physics. *IBM Journal of Research and Development*. 1967 [1928]; 11(2): 215–234. doi:10.1147/rd.112.0215. It can be downloaded free from: `http://web.stanford.edu/class/cme324/classics/courant-friedrichs-lewy.pdf`.

A

Additional results

A.1 Wave formation

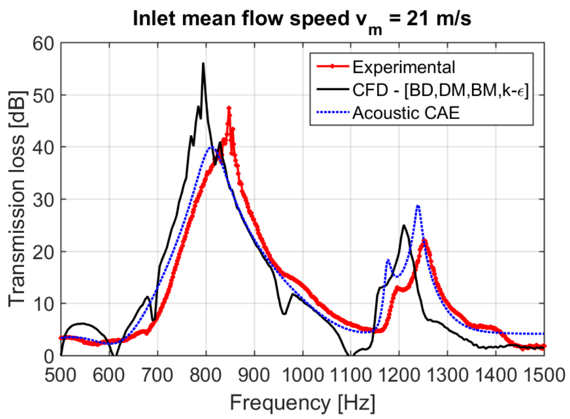

Figure A.1: Transmission loss from CFD simulation including bent duct geometry, decomposition method with distant microphones, basic mesh and $k - \varepsilon$ model compared to experimental results and acoustic CAE for inlet flow speed of 21 m/s.

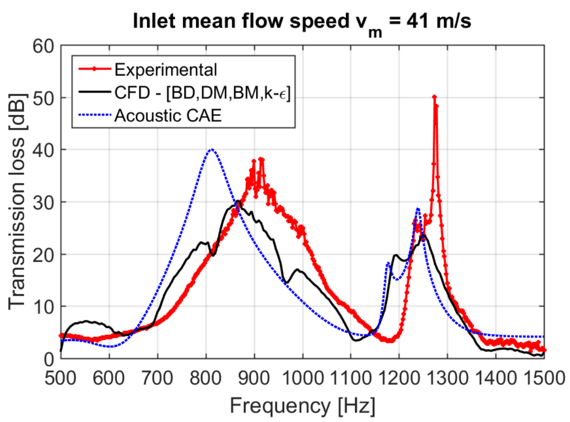

Figure A.2: Transmission loss from CFD simulation including bent duct geometry, decomposition method with distant microphones, basic mesh and $k - \varepsilon$ model compared to experimental results and acoustic CAE for inlet flow speed of 41 m/s.

A.2 Mic. comparison for two-source method

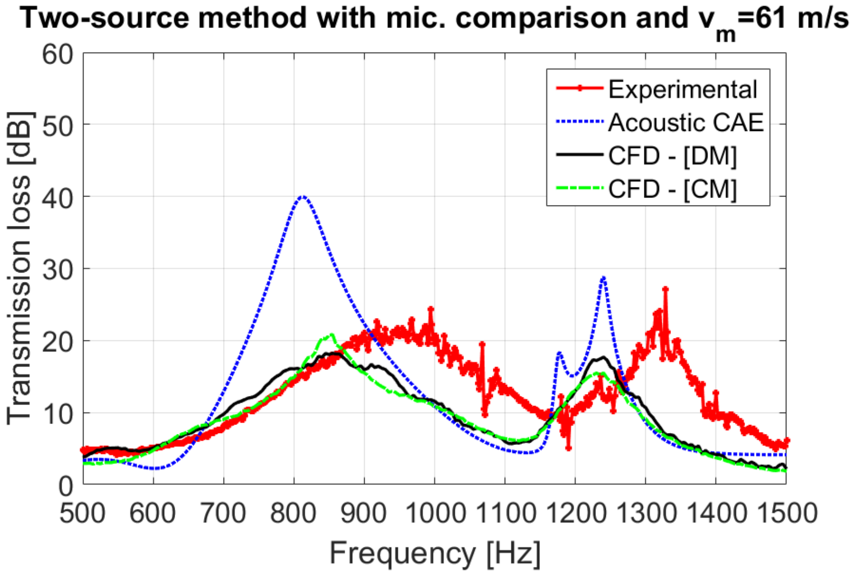

Figure A.3: Transmission loss from CFD simulation including bent duct geometry, two-source method, advanced mesh mesh and SST $k-\omega$ model comparing microphone pairs for inlet flow speed of 61 m/s.

A.3 Geometrical change - mesh

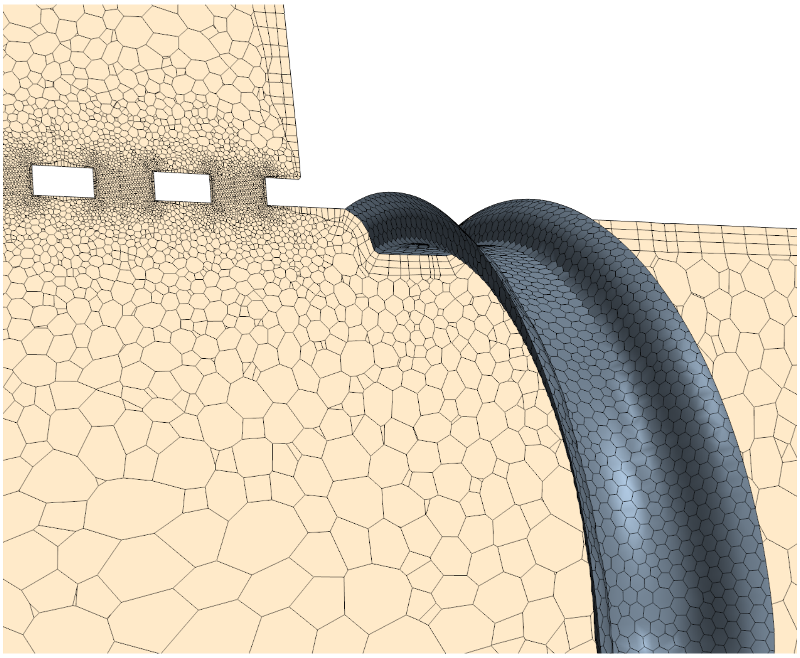

Figure A.4: Mesh from the straight duct computational domain including the Ridge x1 geometrical change.

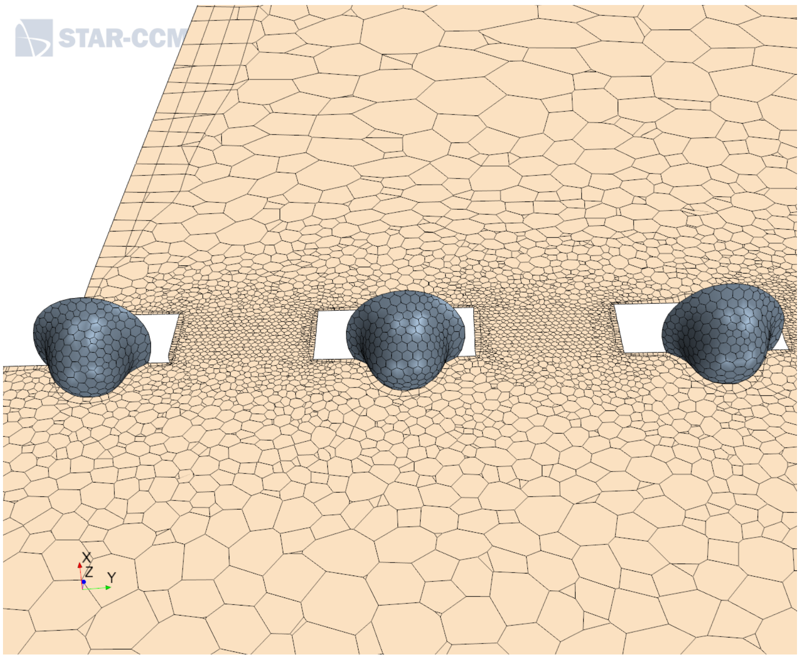

Figure A.5: Mesh from the straight duct computational domain including the Stamp Full geometrical change.

A.4 Neck flow speed

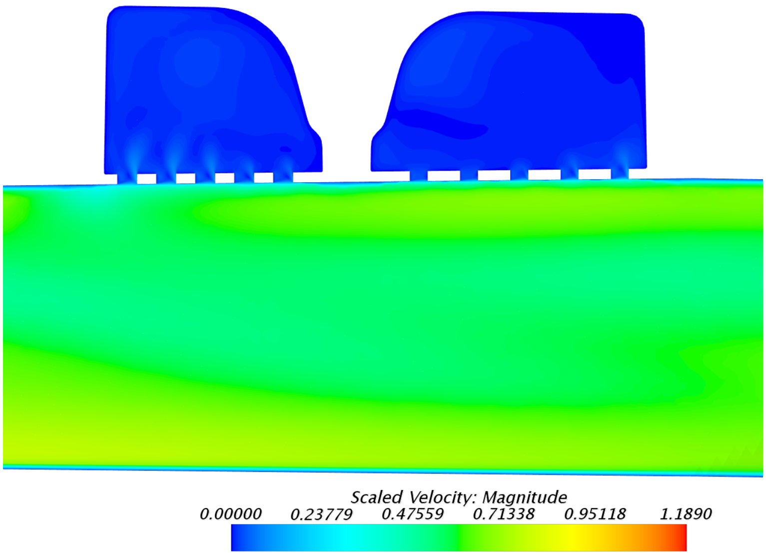

Figure A.6: Magnitude of dimensionless scaled velocity contour plotted on a duct-centered cut-through plane in the silencer region for the bent duct geometry for inlet mean flow speed of 21 m/s. Flow direction from left to right. Basic mesh with $k-\varepsilon$ turbulence model.

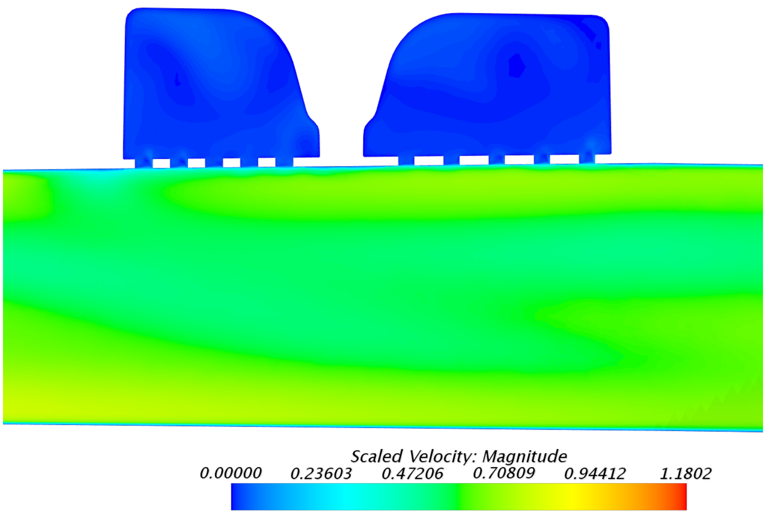

Figure A.7: Magnitude of dimensionless scaled velocity contour plotted on a duct-centered cut-through plane in the silencer region for the bent duct geometry for inlet mean flow speed of 41 m/s. Flow direction from left to right. Basic mesh with $k-\varepsilon$ turbulence model.

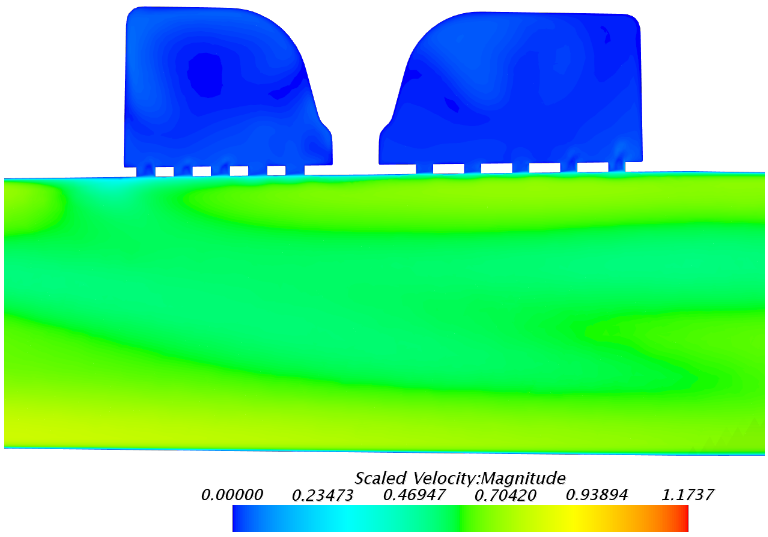

Figure A.8: Magnitude of dimensionless scaled velocity contour plotted on a duct-centered cut-through plane in the silencer region for the bent duct geometry for inlet mean flow speed of 61 m/s. Flow direction from left to right. Basic mesh with $k-\varepsilon$ turbulence model.

A.5 Neck flow pattern

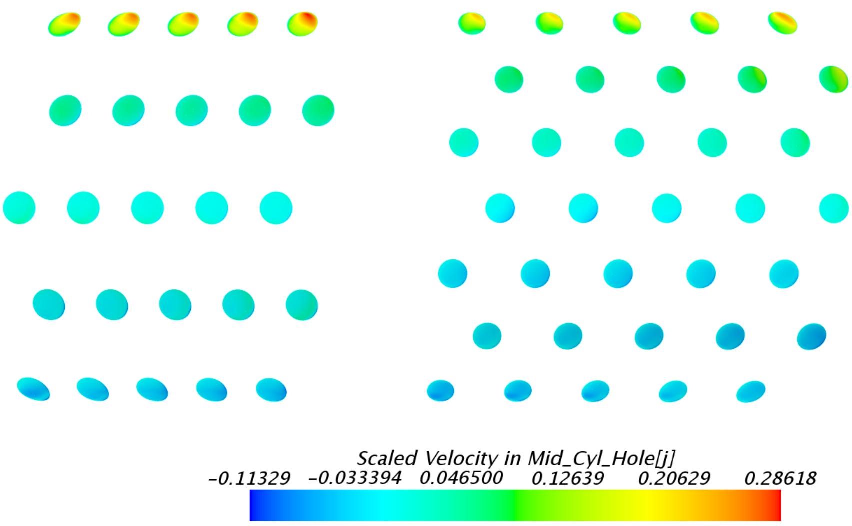

Figure A.9: Dimensionless scaled velocity in the direction of the neck extrusions contour plotted on the neck orifice surface, positive direction towards the resonator cavity, scaled with inlet mean flow speed of 21 m/s. Basic mesh with $k-\varepsilon$ turbulence model.

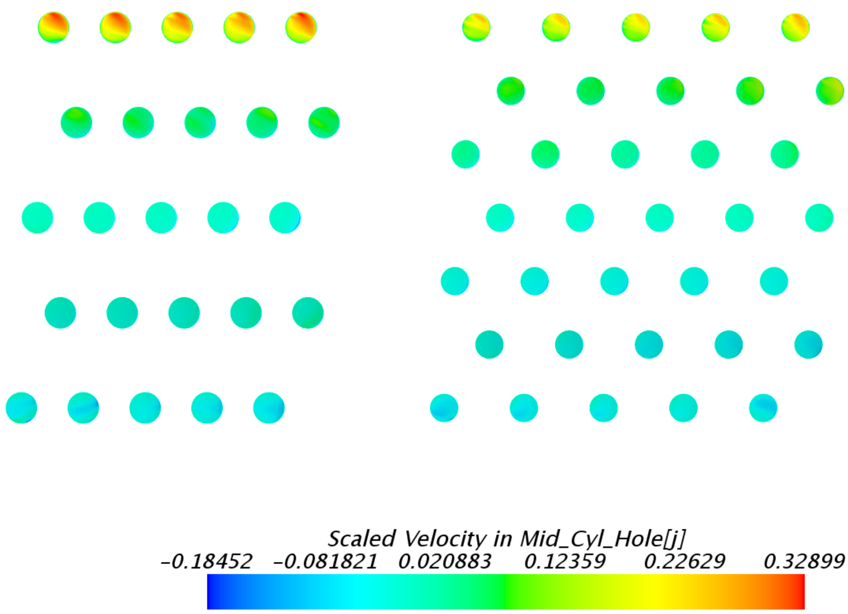

Figure A.10: Dimensionless scaled velocity in the direction of the neck extrusions contour plotted on the neck orifice surface, positive direction towards the resonator cavity, scaled with inlet mean flow speed of 41 m/s. Basic mesh with $k-\varepsilon$ turbulence model.